Influence of Electrode Buffer Layers in Plasmonic Bulk Heterojunction Solar Cells

A thesis submitted by

Ashish Singh

to

Indian Institute of Technology Guwahati

for the award of the degree of

Doctor of Philosophy

Centre for Nanotechnology
Indian Institute of Technology Guwahati
Guwahati – 781039, Assam
India

September 2017

Centre for Nanotechnology
IIT Guwahati
PhD Thesis

Influence of Electrode Buffer Layers in Plasmonic Bulk Heterojunction Solar Cells

Ashish Singh

Supervisor

Prof. Parameswar Krishnan Iyer
September 2017

भारतीय प्रौद्योगिकी संस्थान गुवाहाटी
Indian Institute of Technology Guwahati
Guwahati- 781039, Assam, India

Statement

The work contained in this thesis titled '**Influence of Electrode Buffer Layers in Plasmonic Bulk Heterojunction Solar Cells**' has been carried out by me under the supervision of Dr. Parameswar Krishnan Iyer, Professor, Department of Chemistry and Centre for Nanotechnology, Indian Institute of Technology Guwahati. This work has not been submitted elsewhere for the award of any degree.

Ashish Singh

Roll No. 126153004
Centre for Nanotechnology
Indian Institute of Technology Guwahati
Guwahati – 781039
Assam, India

September 2017

भारतीय प्रौद्योगिकी संस्थान गुवाहाटी
Indian Institute of Technology Guwahati
Guwahati- 781039, Assam, India

Certificate

It is certified that the work contained in the thesis entitled '**Influence of Electrode Buffer Layers in Plasmonic Bulk Heterojunction Solar Cells**' by Ashish Singh, a student of Centre for Nanotechnology, Indian Institute of Technology Guwahati, for the award of the degree of Doctor of Philosophy has been carried out under my supervision. This work has not been submitted elsewhere for any degree.

Parameswar Krishnan Iyer

Professor,
Department of Chemistry and
Centre for Nanotechnology
Indian Institute of Technology Guwahati
Guwahati – 781039
Assam, India

September 2017

This Thesis is dedicated to my family
for their endless love, support and encouragement

Acknowledgements

This thesis might not have seen through its completion unless I had the support and encouragement of numerous people around me. Today, when I bring it to an end, I would like to express few words of appreciation to the people who actually made this thesis a reality and an unforgettable experience for me.

To begin with, I would like to thank my supervisor, Prof. Parameswar Krishnan Iyer not only for being so supportive, but also for providing me with the opportunity to travel and interact with people who inspired me to work even harder and pursue science more vigorously. This milestone would have been a dream for ever if I hadn't had the fortune of meeting Prof. Iyer who always allowing me to pursue my research the way I desired, he gave me the opportunity to learn from my mistakes – being always there by me in all my troubles.

I sincerely thank and appreciate the members of my doctoral committee, Prof. Roy P. Paily, Prof. Arun Chattopadhyay and Prof. Harshal B. Nemade for periodically assessing my work and providing many detailed and crucial comments for its betterment.

I am going to cherish my time spent in IITG due to the many friends and groups - whom I consider a part of my life. Things around me wouldn't have been so beautiful if I wouldn't have met and shared my moments with Anand, Shyam, Purushottom, Ram and Dip. I am going to treasure the moments I spent with my seniors – Rumi didi, Suresh Bhaiya, Bheem Bhaiya and Radha Bhaiya. My time in IITG was enriched by my juniors – Mitradip, Niranjan Meher, Surjendu, Subrata, Adil, Rameshji, Ritesh, Indrani, Rahul, Nystha and all my synthesis lab-mates. A special thanks to Paran da, Kaustubh da, Indrajit da, Milan da and Pranjoli ma'am for extending their best supports towards my research, whenever it was required. This thesis wouldn't have seen the light of this day without the care and encouragement of all of my well-wishing friends from Bhopal, Madhya Pradesh. I would like to specially thank Harsh Sandeep, Ankur, Saurabh and Kaushal for their constant motivation which made me reach this point.

I am thankful to Prof. Dr. Peter Müller-Buschbaum of Technical University of Munich, Germany, Dr. Eric Dufresne, Dr. Joseph Strzalka of Argonne National Laboratory, IL, USA and Dr. Newby Gemma, Dr. Panine Pierre and Dr. James Endicott of Xenocs, France, for various constructive suggestions towards the improvement of my work. I am also thankful to Dr. Prasad Gosavi, Mr. Rajkumar Somendrajit Singh and Dr.

H.M.A. Ehmann of Anton Paar, India for their endless support. I consider myself lucky enough to be able to meet and interact with some of the finest interdisciplinary researchers during my PhD tenure – when I participated in the 44th IEEE Photovoltaic Specialist Conference in Washington DC, USA. I humbly appreciate the patience and interest of Prof. Dr. David S. Ginger, University of Washington and Prof. Dr. Michael McGehee, Stanford University, who earnestly listened to my research and gave their opinion on its future scopes.

I gratefully acknowledge the funding sources that made my PhD work possible. For various characterizing facilities, I remain thankful to the Central Instruments Facility (CIF) and DST funded Organic Electronic Lab, IIT Guwahati.

At the end I would like to express appreciation to Anamika Dey, one of my very special friend cum lab-mate who spent sleepless nights with and was always my support in the moments when there was no one to answer my queries. This thesis would not have been possible to complete without her support. Finally, I would like to thank my family for their understanding, encouragement and patience in my every endeavour. Especially my father, my elder brothers and my sister-in-law's have given me the strength towards this accomplishment throughout, as always, for which, I believe, mere expression of gratitude likewise doesn't suffice.

Thank you very much, everyone for your endless support and encouragement.

Ashish

Abstract

The incremented universal demand of cost efficacious sustainable energy sources has inspired the researchers and engineers to develop new methods to convert solar energy into electrical energy. Among all of these, the third generation, Organic Photovoltaic (OPV) technology is one of the most promising one because of its potential to achieve a faster, lower-cost and compatibility with larger area and flexible substrates to manufacture devices compared to the conventional first generation- silicon wafer and second generation-CdTe and CIGS based thin film solar cell technologies. The Organic Bulk Heterojunction (BHJ) solar cell is one of the third-generation solar cells having its simplest device architecture with a blend active layer of two kinds of organic material, where one functions as an electron donor and the other functions as an electron acceptor. However, because of low charge carrier mobility of organic semiconductors, the Power Conversion Efficiency (PCE) of BHJ organic solar cells are not yet high enough for commercialization and restricted their use to satisfy this huge growing global demand. Therefore, in order to increase the PCE of BHJ organic solar cells has become one of the most interesting research topics at the present time due to their promising application in future as a replacement to their inorganic counter parts.

Considering the demand of cost efficient organic BHJ solar cell, different device architecture modulation methods have been introduced in this thesis for improving the PCE value. The thesis mainly focuses to modify the cathode and anode buffer layers to improve the PCE of very commonly studied organic BHJ system, namely, regioregular poly (3-hexylthiophene-2, 5-diyl) (rrP3HT):[6, 6]-Phenyl $C_{61/71}$ butyric acid methyl ester ($PC_{61/71}BM$). For modulating cathode contact different types of hole and electron rich small molecules were introduced in the device structure whereas to modulate the anode contact various types of easily synthesised plasmon induced metal nanoparticles were doped in the hole injecting PEDOT:PSS layer. The thesis mainly introduced a very simple, unique and robust methodology consisting of the combine effect of dual cathode buffer layers and different shaped plasmon induced metal nanoparticles for improving the PCE value as well as the morphological information of very commonly studied rrP3HT:PCBM system which can be further used in the next generation of solar cell technology.

Contents

Chapter 1

Introduction

The photovoltaic (PV) cells have been extensively studied since 1950 when the first crystalline Silicon (Si) solar cell was developed at Bell Laboratories. Since then, the efficiency of crystalline Si solar cells has reached up to 24%, which is already proximate to the upper limit of theoretically predicted efficiency (~30%). But one of the major obstacles for the market implementation of photovoltaic cells is the large production costs of Si based technology.[1,2] However, despite much effort to further reduce the price, large scale production of Si-based solar cells will be limited by the unavailability of raw materials, such as solar-grade Si. Therefore, to ensure a sustainable technology path for PV, the development of new materials and device structures are required.[3,4] Solar cell technologies are traditionally divided into four generations- *First generation solar cells* are mainly based on Silicon wafers and typically demonstrate a performance about 15-20%. The benefits of this generation lie in their good performance, as well as their high stability. Silicon cells have a quite high efficiency, but very pure Silicon is needed for this type of technology. However, they are rigid and require a lot of energy in production. Due to these reasons, this generation is dominating the commercial market.[5-7]

The second generation solar cells are based on amorphous Silicon, CIGS and CdTe, where the typical performance is 10-15%. Since this generation of solar cells avoid the use of Si-wafers and have a lower material consumption, it has been possible to reduce the production costs of these types of solar cells compared to the first generation. However, as the production of second generation solar cells still include vacuum processes and high temperature treatments, there is still a large energy consumption associated with the production of these solar cells. Further, the second generation solar cells are based on scarce elements and this is a limiting factor in the price.[8]

The *third generation solar cells* use organic materials such as small molecules or polymers. The polymer materials, which are generally known as plastics, have a very significant role in our everyday life, due to their low cost and easy manufacturing protocol compared to many of the other traditional materials. In the early days of Bakelite (the first plastic material), polymers were commonly used as electrically insulating materials in the fabrication of electronic products. However, this idea completely changed in 1976; when Alan J. Heeger, Alan G. MacDiarmid and Hideki Shirakawa proved that the conductivity of the organic polymer, namely, polyacetylene, can be improved several orders by simply exposing the vapor of iodine.[9] Due to this outstanding discovery, they were jointly awarded by Nobel Prize in Chemistry, in the year of 2000, 'for the discovery and development of conductive polymers.' After this innovation, some of the conducting polymers were observed to have similar electrical and optical properties like inorganic semiconductors, with the addition of mechanical flexibility, low-cost, and other advantages of plastics. Further the solar cells containing these materials can also be fabricated with well-known industrial roll-to-roll technology which is analogous to the process involved for printing newspapers. The performance and stability of third generation solar cells although is still limited compared to the first and second generation solar cells. Research interest in polymer solar cells has increased significantly in recent years but this type of solar cell is yet to generate a strong commercial application because of the lower power conversion efficiency (PCE) compared to the inorganic solar cells.[10]

Fourth generation solar cells bring most of the successful types of solar cells till now for mankind and these are called Hybrid-Nanocrystal or Plasmonic solar cells.[11-16] This generation combines the low cost, flexible polymer thin films with the stable novel inorganic nanostructures so that it can improve the optoelectronic properties of the low cost thin film PVs.[17-21] The organic semiconductor based plasmonic solar cell (PSC) is one of this fourth generation solar cells having its simplest device architecture where the application of the plasmonic effect through the use of noble metal nanoparticles (NPs) is another valuable route to improve light harvesting within the absorption range of a given PSC device. However, because of low charge carrier mobility of organic semiconductors, the PCE of plasmonic organic solar cells are not yet high enough for commercialization and restricted their use to satisfy this huge growing global demand. Therefore, to increase the PCE of these types of solar cells has become one of the most interesting research topics presently due to their promising application in future as a replacement to their inorganic counter parts.

1.1 Parameters of Solar Cell

A Solar cell or photovoltaic cell is a type of optoelectronics device that converts the light energy into electrical energy based on the principles of photovoltaic effect. The word 'solar cell' is used for devices intended specifically to capture energy from sunlight, while the word 'photovoltaic cell' is used when the light source is unspecified. The device mainly performed two functions- (1) photo generation of charge carriers in a light-absorbing material and (2) separation of the charge carriers by conductive electrodes which will transmit the electricity.

The simplified device schematic and equivalent circuit model of a solar cell is depicted in Figure 1.1. The model consists of a photon current source (I_{PH}), a diode, a series resistance (R_S), and a shunt resistance (R_{SH}). The output of the circuit is connected to an external load (R_{LO}). On sweeping the voltage across R_{LO} by means of a voltage source and monitoring the current through Rs, the voltage-current density characteristics (J-V curve) of a solar cell can be obtained.[22] In the dark, a solar cell has an exponential J-V characteristic similar to that of a diode, as shown in Figure 1.2.[23] Without illumination, no current flows through the diode unless there is an external potential applied. When the applied potential is in the forward bias direction, the curve shows the turn-on and the build-up of the forward bias current. With incident sunlight, the J-V curve shifts down into the fourth quadrant indicating that there is current flow from the solar cell to a passive load.[24] From the equivalent circuit, it is evident that the current generated by light is divided into three parallel branches: the diode, the shunt and external resistors. As a result the output current can be calculated by the following equation:

$$I = I_{PH} - I_D - I_{SH} \tag{1}$$

Where, I is the output current; I_{PH} is the photo-generated current; I_D is the diode current and I_{SH} is the shunt current.

I_D follows the Shockley diode equation, which is given below-

$$I_D = I_0 \left[e^{\left(\frac{qV_D}{nkT}\right)} - 1 \right] \tag{2}$$

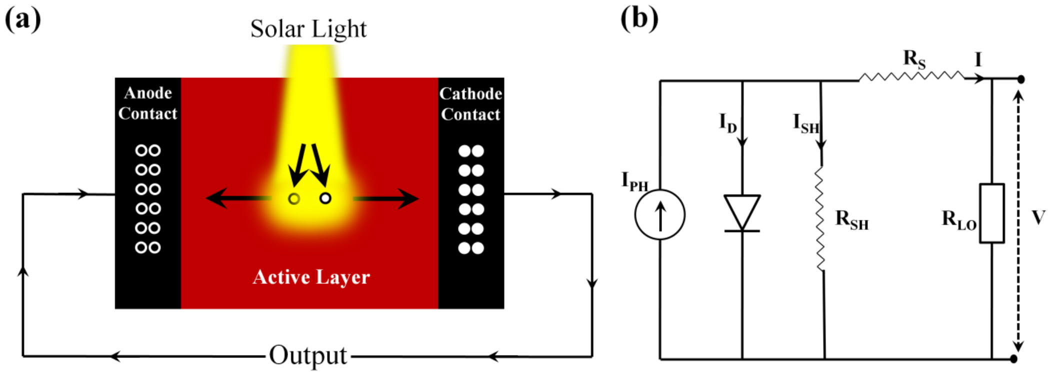

Figure 1.1. (a) Schematic of device architecture and (b) equivalent circuit of solar cell.

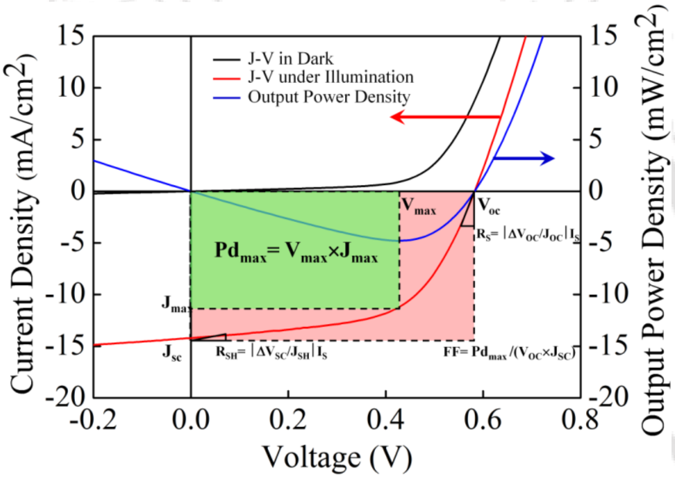

Figure 1.2. Current density versus voltage (J-V) and output power density versus voltage characteristics of solar cell.

Here I_o is the saturation current; V_D is the voltage across the diode; q is the magnitude of the electrical charge on the electron; n is the diode ideality factor; k is the Boltzmann constant and T is the absolute temperature. According to Ohm's Law I_{SH} can be written as

$$I_{SH} = \frac{V_{SH}}{R_{SH}} \tag{3}$$

Where, V_{SH} is the voltage across the shunt resistor. It should be noted that

$$V_D = V_{SH} = V + IR_S \tag{4}$$

Where, V is the voltage across the output terminals, I is the output current and R_S is the series resistance. By substituting equations (2), (3) and (4) into equation (1), the voltage-current characteristics of a solar cell device can be obtained,

$$I = I_{PH} - I_D - I_{SH} = I_{PH} - I_0\left[e^{\frac{q(V+IR_S)}{nkT}} - 1\right] - \left(\frac{V+IR_S}{R_{SH}}\right) \tag{5}$$

From the illuminated J-V characteristic several important parameters can be extracted to estimate the performance of a solar cell.

1.1.1 Short-Circuit Current Density (J_{sc})

If the cell is short circuited (R_{LO} = 0), it cannot deliver a voltage but generates the maximum current (I_{SC}). Under an external load, the current will always be less than I_{SC}. I_{SC} has a dependence on the solar cell area. Therefore, the current density (J_{SC} in the unit of $A{\cdot}cm^{-2}$ or $mA{\cdot}cm^{-2}$) is adopted as;

$$J_{SC} = \frac{I_{SC}}{S} \quad (6)$$

Where, s is the active area of a solar cell, in cm^2.

1.1.2 Open-Circuit Voltage (V_{oc})

In the case of open circuit ($R_{LO}\rightarrow\infty$), no current flows through the terminals of the solar cell but the potential developed across the external load is at the maximum.

1.1.3 Output Power Density (Pd)

Under both extreme situations of short circuit and open circuit, no power can be extracted from a solar cell device. However, at other operating points in the fourth quadrant the cell delivers an output power density ($Pd = J \times V$, plotted as the blue curve in Figure 1.2), which can be identified as the area of the rectangle formed between a point on the J-V curve and the axis. The maximum power density point is reached where the area of the resulting rectangle is the largest ($Pd_{max} = J_{max} \times V_{max}$, the green rectangle in Figure 1.2).

1.1.4 Power Conversion Efficiency (PCE, η)

The PCE is the most commonly used parameter to compare the performance of one solar cell to another. It is defined as the energy output from the solar cell divided by the input energy from the sun:

$$PCE = \frac{Output\ Power\ (Electric)}{Input\ Power\ (Photon)}\ [\%] \quad (7)$$

The standard solar spectrum has a radiation power density of 100 $mW{\cdot}cm^{-2}$. Hence, the efficiency is given by:

$$PCE = \frac{Pd_{max}}{100\ mW.cm^{-2}} = \frac{J_{max} \times V_{max}}{100\ mW.cm^{-2}} \quad (8)$$

Where, J_{max} is the current density and V_{max} is the voltage at the maximum output power density point. Notice that, in this case, the units must be either mA·cm^{-2} and V, or A·cm^{-2} and mV.

1.1.5 Fill Factor (FF)

The fill factor (FF) of a solar cell is defined as the ratio of actual maximum output power of the device to the product of J_{SC} and V_{OC}. The equation for FF can be expressed as

$$FF = \frac{Pd_{max}}{J_{SC} \times V_{OC}} = \frac{J_{max} \times V_{max}}{J_{SC} \times V_{OC}} \qquad (9)$$

The fill factor is a key parameter which signifies how close an actual device is to the ideal status. In other words, it reflects how difficult or how easy the photo-generated carriers can be extracted out of a photovoltaic device. From a mathematical point of view, FF is a parameter to estimate the squareness of a solar cell device, if the J-V curve had a square shape, FF would be 1. However, because the J-V curve has an exponential shape, FF is always smaller than 1.

1.1.6 Series Resistance (R_S) and Shunt Resistance (R_{SH})

Resistive effects of solar cells reduce its PCE by dissipating power in the resistances. The most common resistances observed in any types of solar cells are series resistance (R_S) and shunt resistance (R_{SH}).[25] For an ideal solar cell, R_S should be equal to zero while R_{SH} should be infinite. However, practically the observed R_S is inevitable and R_{SH} is far less than infinite. Generally R_S determines the terminal voltage of the cell in relation to the open circuit voltage whereas R_{SH} governs the fraction of photo-generated current of the cell flowing into the external load.[26] Therefore R_S and R_{SH} are important parameters to analyse the performance of a solar cell. The values of R_S and R_{SH} can be estimated by the following equations-

$$R_S = \left|\frac{dV}{dI}\right|_{V=V_{OC}} = \frac{1}{S} \times \left|\frac{dV}{dJ}\right|_{V=V_{OC}} \qquad (10)$$

and

$$R_{SH} = \left|\frac{dV}{dI}\right|_{V=0} = \frac{1}{S} \times \left|\frac{dV}{dJ}\right|_{V=0} \qquad (11)$$

1.1.7 External Quantum Efficiency (EQE)

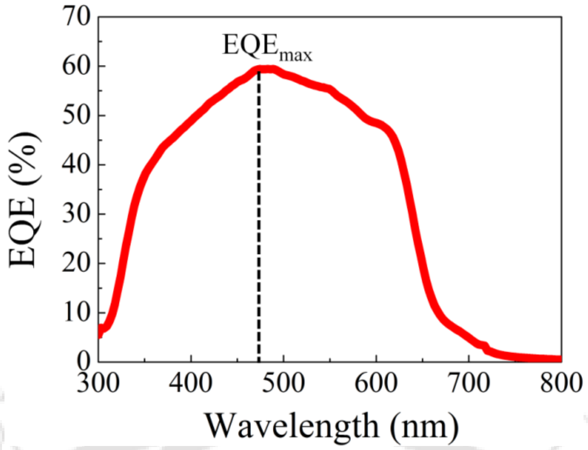

Figure 1.3. External quantum efficiency (EQE) versus wavelength (λ) curve measured at monochromatic incident light.

The quantum efficiency (QE) is a very important parameter to determine how efficiently a solar cell converts photons into electrons. Since the energy of a photon depends on its wavelength, QE is measured by recording the photocurrent response while continuously varying the wavelength of the excitation light. Generally, considering the optical losses occurring on coupling light in the active region of the device, QE can be classified into two types: external quantum efficiency (EQE) and internal quantum efficiency (IQE). EQE is the ratio between the number of charge carriers collected by the solar cell and the number of photons shining on the cell from outside, defined as

$$EQE(\lambda) = \frac{N_e}{N_p} = \frac{J/q}{P_{in}/hf} = \frac{J}{P_{in}} \times \frac{hv}{q\lambda} = \frac{J}{P_{in}} \times \frac{1240}{\lambda} \qquad (12)$$

Where, N_e is the number of electrons, N_p is the number of photons, J is photocurrent density ($mA{\cdot}cm^{-2}$), P_{in} is incident light power, ($mW{\cdot}cm^{-2}$), h is the Planck constant, f is the frequency of light in vacuum (Hz), v is the speed of light in vacuum ($nm{\cdot}s^{-1}$), q is the magnitude of the electrical charge on the electron (C) and λ is the wavelength (nm). IQE can be inferred from EQE on condition that transmission and reflection losses of incident light are known-

$$IQE(\lambda) = \frac{EQE}{(1-\eta_r-\eta_t)} \qquad (13)$$

Where, η_r and η_t are reflection and transmission loss ratios respectively. A typical example of EQE spectrum is shown in Figure 1.3. At any given wavelength, the higher EQE the higher photon to current efficiency is. The maximum EQE is named EQE_{max}, which is a key parameter for describing the energy conversion efficiency of a device.

1.2 Organic Solar Cell (OSC)

An organic or plastic solar cell (OSC) is a type of solar cell that uses conductive organic semiconductors for light absorption and charge transportation to produce electricity from sunlight by following the photovoltaic effect. Organic semiconductors are very simple materials which contained carbon compounds. They only become conductors of electric current when excess charge carriers are either produced by the internal photo effect or are injected by applied voltages. Depending upon the nature of majority carriers, they are generally classified as p-type (donor) or n-type (acceptor) organic semiconductors. In p-type semiconductors the majority carriers are holes, while in n-type semiconductors, the majority carriers are electrons. An organic semiconductor contained solar cell has many intrinsic advantages, such as they are light in weight, flexible, and have manufacturing costs. They are generally can distinguished by their production technique such as wet processing technique or thermal evaporation. This thesis generally focuses on the wet processing method for the fabrication of solar cell with three different active semiconductor system, namely, poly (3-hexylthiophene-2, 5-diyl) (rrP3HT), [6,6]-Phenyl C_{61} butyric acid methyl ester ($PC_{61}BM$) and [6,6]-Phenyl C_{71} butyric acid methyl ester ($PC_{71}BM$).

1.3 Working Principle of OSC

In organic photovoltaic cell, generally six important processes have to be optimized to obtain a high conversion efficiency of solar energy into electrical energy. These are- (a) light absorption, (b) excitation, (c) exciton formation, (d) exciton diffusion, (e) exciton dissociation and (f) charge transport and collection. The most important feature that distinguishes organic solar cell from inorganic solar cell is the generation of excitons in organic semiconducting material. Due to the absorption of light, organic semiconductors produce excitons which is a bound state of electron-hole pairs, while in most conventional inorganic solar cells, it results in direct creation of free electron-hole pairs. When the organic semiconductor absorbs a photon bearing energy larger than its bandgap (E_g), an electron will be excited from its highest occupied molecular orbital (HOMO) to the lowest unoccupied molecular orbital (LUMO) and create a hole in its HOMO energy level. However, these two electric charges are attracted to each other to form bond pair the so-called exciton with a binding energy of about 0.1 to 1 eV.[27,28]

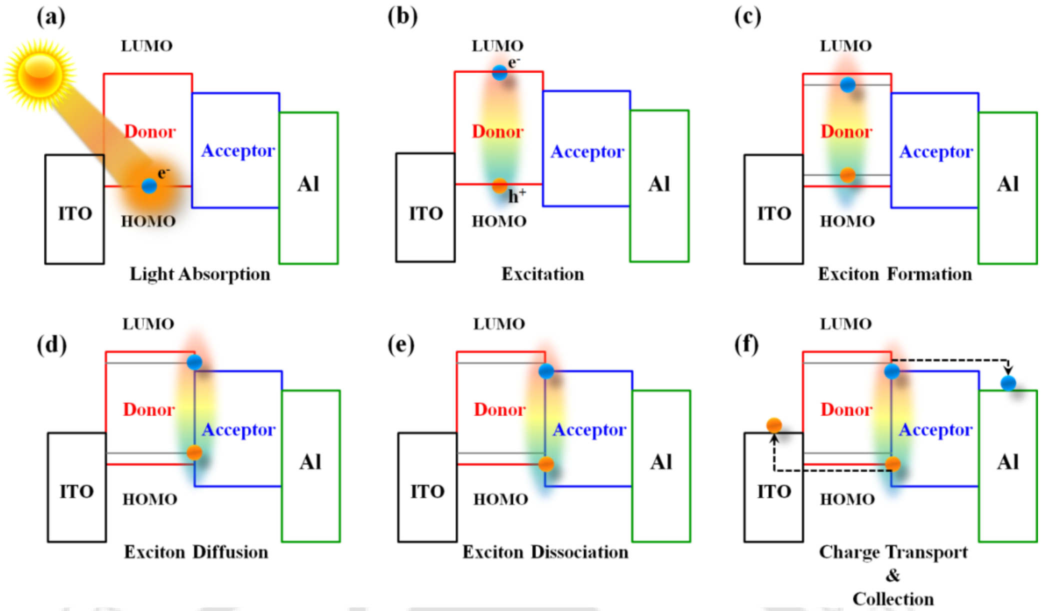

Figure 1.4. Basic processes in organic solar cell.

These excitons may diffuse to certain sites for dissociation before they decay radioactively or non-radioactively. The generated charge carriers then need to move through the organic film to reach the respective electrodes and become available for injection into an external circuit. The step-by-step processes involved in the working principle of OSC are schematically shown in Figure 1.4.

1.4 Types of OSC

Based on the structure and operational principles, the organic solar cells are classified in various types which are discussed in detail below-

1.4.1 Single Layer OSC

A single layer solar cell is one of the fundamental and simplest architecture of organic photovoltaic cells. The device structure of these cells are one organic semiconducting layer which is sandwiching two contact electrodes, typically a semi-transparent layer of indium tin oxide (ITO) acting as an anode and a non-transparent layer of low work function metal such as Al, Mg or Ca. The schematic of such device structure is illustrated in Figure 1.5a.

This structure was first introduced by Marks et al. in 1994, by using poly (phenylene vinylene) (PPV) as the organic semiconducting material.[29] The quantum efficiency of this device was found to be around 0.1% under the illumination of 0.1 mW/cm^2 light intensity. This low quantum efficiency is because of the low carrier mobility of the active layer material. The mobility of the active layer material was found to be ~10^{-3} $cm^2/V{\cdot}s$, which is very less in comparison to single crystalline silicon (~10^3 $cm^2/V{\cdot}s$). Due to this low carrier mobility, the photo generated charges in semiconducting layer needs more time to reach to the respective electrodes, as a result of which the PCE value decreases.

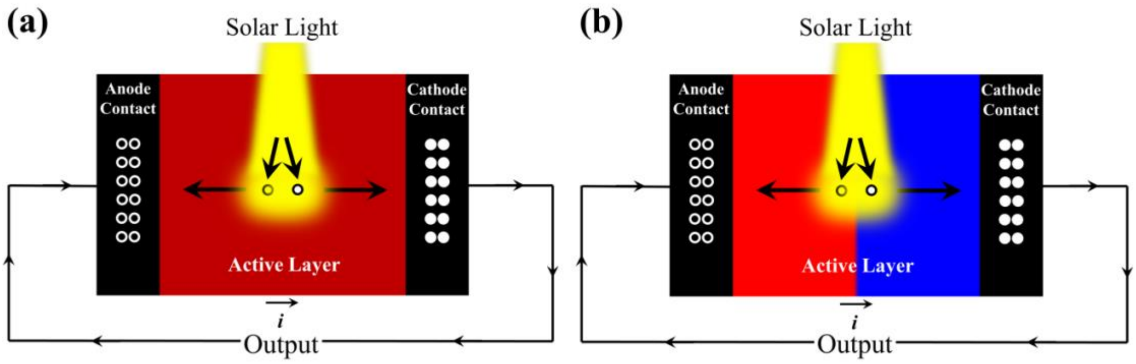

Single Layer OSC

Bi-layer Heterojunction OSC

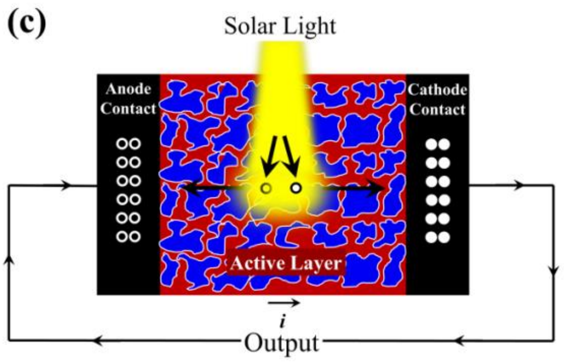

Bulk Heterojunction (BHJ) OSC

Figure 1.5. Schematics of (a) Single Layer (b) Bi-Layer Heterojunction and (c) Bulk Heterojunction organic solar cells.

The slow charge conveying reduces the efficiency of the OPV cell, but increases the chance of charge carrier recombination. The other quandary that causes the low PCE of single layer OSCs is the exciton formations, which are efficaciously bound dipole charges of photo exhilarated organic semiconductor. Free electrons and holes are desired as an efficient charge carrier since the exciton requires an extra step for exciton dissociation to make free carriers, which further decreases the efficiency of carrier generation. In case of single layer OSC, there is only one place where the excitons can be dissociated into free carriers which is the interface between the active layer and the cathode electrode. Later, it was found that the excitons can be dissociated efficiently at the donor-acceptor interface and depending on this idea a bi-layer OSC was developed.

1.4.2 Bi-layer Heterojunction OSC

Bi-layer organic solar cell is the upgraded version of single layer solar cell where two different layers of organic semiconductor having different electron affinity and ionization energy are sandwiches in between the two conductive electrodes (Figure 1.5b). Due to the different electron affinity and ionization energy of the semiconductor layers electrostatic forces are engendered at the interface between these. The materials are chosen in such a way that this difference is large enough to generate strong local electric fields which help to dissociate the excitons more efficiently than the single layer OSC. The organic semiconducting layer which has higher electron affinity and ionization potential is termed as electron acceptor, whereas the other is termed as electron donor. This device architecture is also known as planar donor-acceptor heterojunction.

This OSC device architecture was first introduced by Prof. C. W. Tang in the year of 1986. Copper Phthalocyanine (CuPc) and perylene tetra carboxylic derivative (PDI) were used by him for the fabrication of the device with ITO and silver (Ag) as the electrodes. The PCE of the device was observed to be ~1% under simulated AM2 conditions.[30] However, the reported PCE of bi-layer OSCs are still lagging behind the PCE of inorganic solar cells. One of the main reasons for this may be the short diffusion length of the excitons which are usually ~10 - 20 nm. By using C_{60} organic small molecule researchers attempted to overcome this limitation. In this regard, P. Peumans et al. used C_{60} as an acceptor in the place of perylene tetra carboxylic derivative and achieved ~3.5% of PCE.[31] Other way to developed efficient bi-layer heterojunction OSCs is the incorporation of conjugated polymers inside the device structure. This types of first bi-layer heterojunction OSC was fabricated by Sariciftci et al, where MEH-PPV, a conjugated polymer was used as hole transporting material along with the electron transporting material C_{60}.[32] In device structure, the obtained PCE was 0.04% under illumination of light having 514.5 nm of wavelength. However, the efficiency of bi-layer heterojunction OSC devices is still limited mainly due to i) the low exciton diffusion length in the donor-acceptor phases and ii) the less availability of donor-acceptor heterojunction interfacial area for excitons dissociation to separated charges, which further generated the concept of Bulk Heterojunction OSC by mixing both the donor and acceptor materials to overcome the above mentioned problems.

1.4.3 Bulk Heterojunction OSC

In this type of organic solar cells, the electron donor and acceptor are mixed together, to form a polymer blend which is used as the active layer of the device (Figure 1.5c). The main advantage of this device architecture is the blend length scale which is almost equal to the exciton diffusion length. As a result of which most of the photo-generated excitons are able to reach to the interface and break efficiently. This type of device architecture was first mentioned by Yu et al. where a blend polymer consisting of poly [2-methoxy-5-(2'-ethyl-hexyloxy)-l, 4-phenylene vinylene] (MEH-PPV) and cyano-PPV (CN-PPV) was used.[33] The cell made with this material shows promising photovoltaic characteristics with PCE of 0.9%, which is 20 times larger than the PCE observed in MEH-PPV polymer based bi-layer OSC.

The next significant increment in PCE of this type of solar cell was achieved by using poly (3-hexylthiophene) (P3HT) as a donor polymer. Gang Li et al. fabricated a Bulk Heterojunction OSC cell using the blend of P3HT and PCBM polymers.[34] They observed significant improvement in PCE value which is because of the higher crystallinity of P3HT and better morphology. Since the better phase separation in the morphology of the blend active layers increases the hole mobility of the conjugated polymer which further helps to improve the absorption efficiency, several modifications like solvent annealing, varying the evaporation rate, etc., were done to optimize morphology of the active materials.

Y. Kim et al. also studied the same blend active layer system by using regioregular P3HT (rrP3HT).[35] Various blend solutions were prepared by them in which P3HT had different regioregularities ranging from 80% to 96%. The investigation implies that higher order of regioregularities of P3HT are essential to improvise the crystallized fibril-like shape of P3HT, which further help to increase the charge transport in BHJ OSC.

1.5 Optimization of BHJ OSC

The sun gives out a tremendous amount of energy every second in the form of irradiation, which reaches the Earth at an energy density of about 1366 W/m^2 just outside the atmosphere, although some energy will be lost after reflection and absorption by the atmosphere.[36] Figure 1.6 shows the standard AM1.5 solar spectrum at the ground level, indicating the energy density with respect to wavelength. The PCE in organic BHJ solar cells can be improved by mostly absorbing maximum amount of solar photons and then collecting maximum number of photo-generated charges at the electrodes. Increasing the light absorption is crucial in order to increase the PCE of these devices. There are several method already reported in the literature which were successfully used to improve the performance of BHJ organic solar cells. Some such important modifications are listed below-

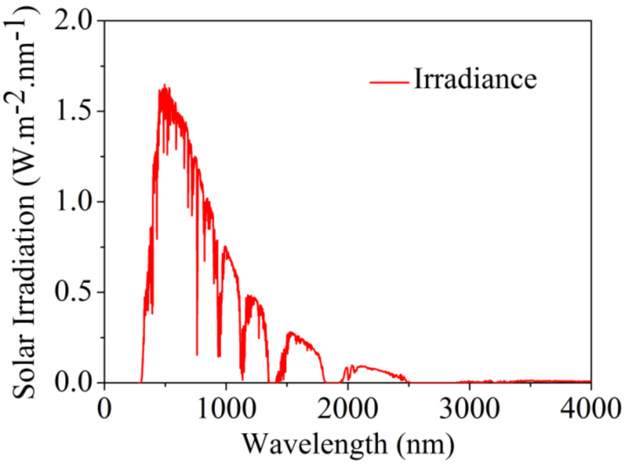

Figure 1.6. Sun irradiance as a function of wavelength.

1.5.1 Development of New Materials

Most of the solar energy of the solar spectrum is concentrated in the visible and near-infrared (near-IR) region. Thus, to efficiently harvest solar energy, the absorption spectra of OSC materials should have a large overlap in this region with the solar spectrum. If a semiconducting polymer has band gap ~1.1 eV (equivalent to photons with wavelength under 1100 nm) then it can able to absorb at least 77% energy of the solar spectrum. Further, if the band gap exceeds ~2 eV (less than 620 nm), then only 30% of the solar energy can be absorbed by it.[37] Thus, the first criteria in designing new polymers is high efficiency in absorbing solar energy in the whole solar spectrum. As the band gap of organic semiconductor determines the absorption limit for a particular polymer, researchers are mainly focusing to improve the absorption features of OSCs by fine tuning absorption characteristics. With a low band gap and a broad absorption band, a polymer can absorb more photons, which will increase the J_{sc} of an OSC. However, further narrowing the band gap of a polymer decreases the V_{oc} value of OSC. Thus, theoretically it has been obtained that the optimal band gap for an organic semiconducting material is around 1.3 eV, which represents the theoretical best possible compromise between V_{oc} and J_{sc} for an ideal solar cell.[38] However, a suitable band gap alone does not ensure always higher PCE of an OSC. It is also necessary to design low-band-gap donor polymers with energy levels that match well with those of the electron acceptor materials, so that the resulting BHJ solar cells will exhibit favored charge-separation and transport characteristics.[39] Some important donor and acceptor materials chemical structures are shown in Figure 1.7 and Figure 1.8 below-

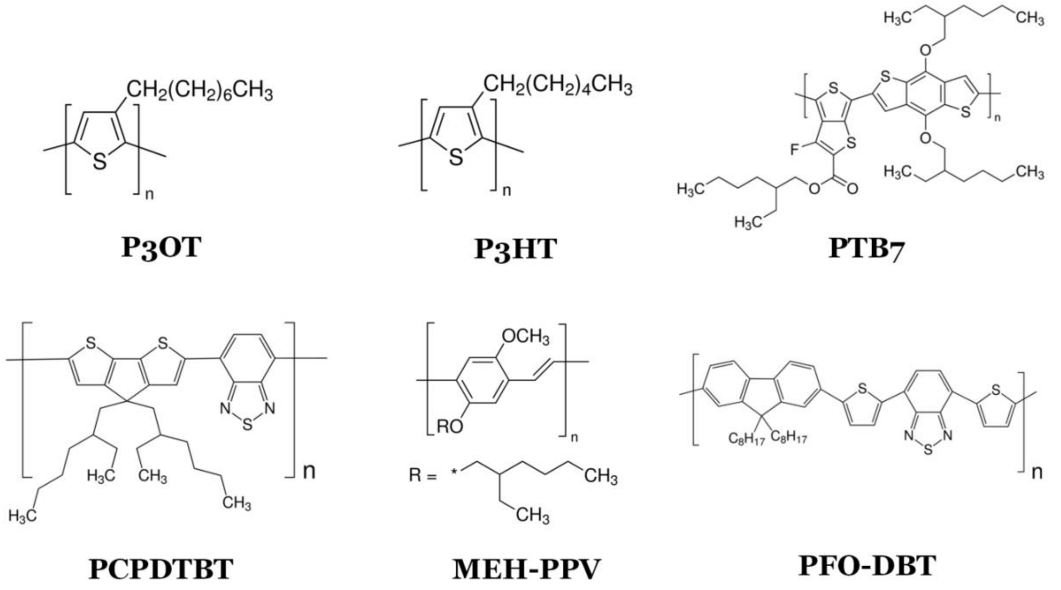

Figure 1.7. Chemical structure of donor materials used in OSC application.

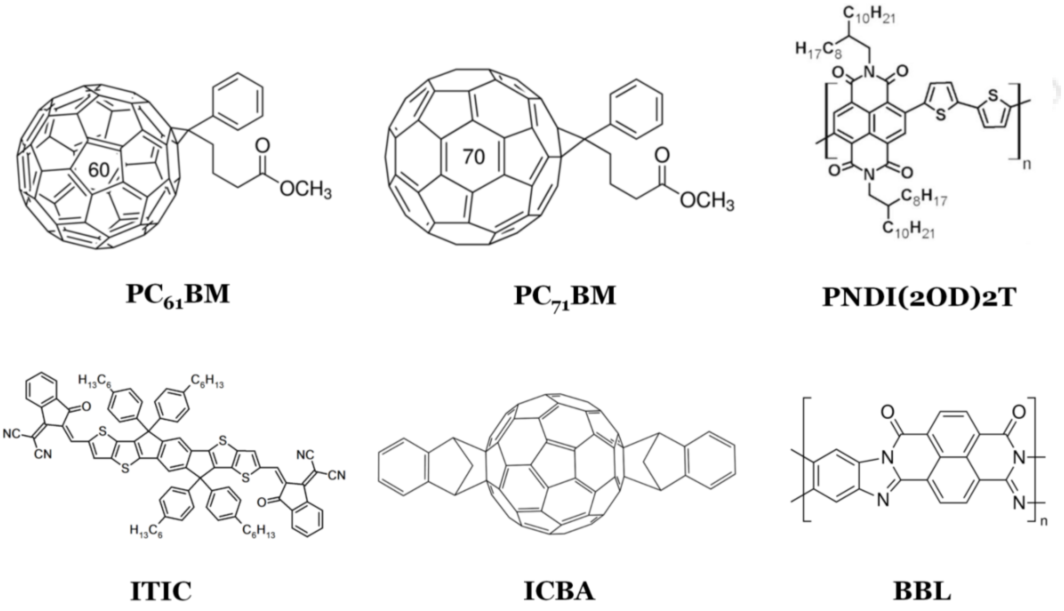

Figure 1.8. Chemical structure of acceptor materials used in OSC application.

1.5.2 Control of Active Layer Morphology

Active layer morphology has great influence on the performance of organic BHJ solar cell. While much effort has been fixated on developing incipient low-bandgap polymers to optimize optoelectronic properties, fine tuning the morphology in the BHJ blend is of equal importance to achieve a high PCE. However, though all active blend layers show identical BHJ structure, significant morphological differences exist, especially in terms of domain size and degree of interpenetration between the domains. Because excitons have a limited lifetime leading to a diffusion length of approximately 10 nm, the active layer must have interpenetrating network morphology to ensure that the exciton can migrate to the donor–acceptor interface to undergo charge separation and that the charges can be transported away. Thus, the domain size of both donor and acceptor should be diminutive enough to optimize exciton migration to the interface and large enough in order to efficiently engender current. In organic BHJ solar cells, the ideal domain size for donor and acceptor material is around 10–20 nm.[40] Numerous studies have been conducted to study how to characterize and control the blend morphology to enhance PCE.[41–43] Several physical methods have been developed, like incorporating solvent additives in the blend solution, thermal annealing, by choosing appropriate host solvents and solvent annealing etc. to control the nano morphology of the active layer.

1.5.3 Optimization of Device Architecture

Similar like new materials design perspective, efficiently extraction and transportation of free charges from blend active polymers to different desire electrodes are equally important for high performance BHJ OSCs. Interfacial layers between the electrodes and the active layer are introduced to facilitate this process, which include both a hole-injecting layer (HIL) and an electron injecting layer (EIL) in a single-junction OSC device. The multiple roles served by the interfacial layer include (1) tuning the work function of the electrode to promote Ohmic contact at the active layer and electrode interface, (2) determining the polarity of the device (conventional device or inverted device), (3) improving the selectivity toward holes or electrons while blocking the other and minimizing charge recombination in the interface, (4) enhancing light harvesting by introducing optical spacers, and (5) improving device stability. In BHJ OPVs, Voc is determined by the difference between the LUMO energy level of the acceptor and the HOMO energy level of the donor provided that an Ohmic contact is formed between the active layer and both the cathode and the anode.

Generally both conventional and inverted device structures are widely used for Organic BHJ solar cells. In a conventional structure, holes are extracted by the bottom electrode, transparent indium tin oxide (ITO) in most cases, while electrons are extracted at the bottom electrode in the inverted structure. It is the interfacial layers which determine the polarity of the device. Therefore, by inserting interfacial layers with good charge selectivity, one can minimize the interfacial charge recombination and increase device performance. To extract holes to the anode, HILs should have an appropriate energy alignment with polymer donors. It is equally important that the conduction band of HILs should be high enough to block the flow of electrons moving to the anode. Similar principles apply to the design of EILs. The interfacial materials should also have larger band gaps than that of the donor and acceptor to prevent the excitons from recombining at the electrode. Finally, it is important to design interfacial materials with high conductivity to reduce the series resistance of the device.[44,45] In the past few years, numerous interfacial materials and new cost-effective ways to make the buffer layers have been developed.[46,47] Some of the widely used interfacial buffer layer chemical structures are shown in Figure 1.9-

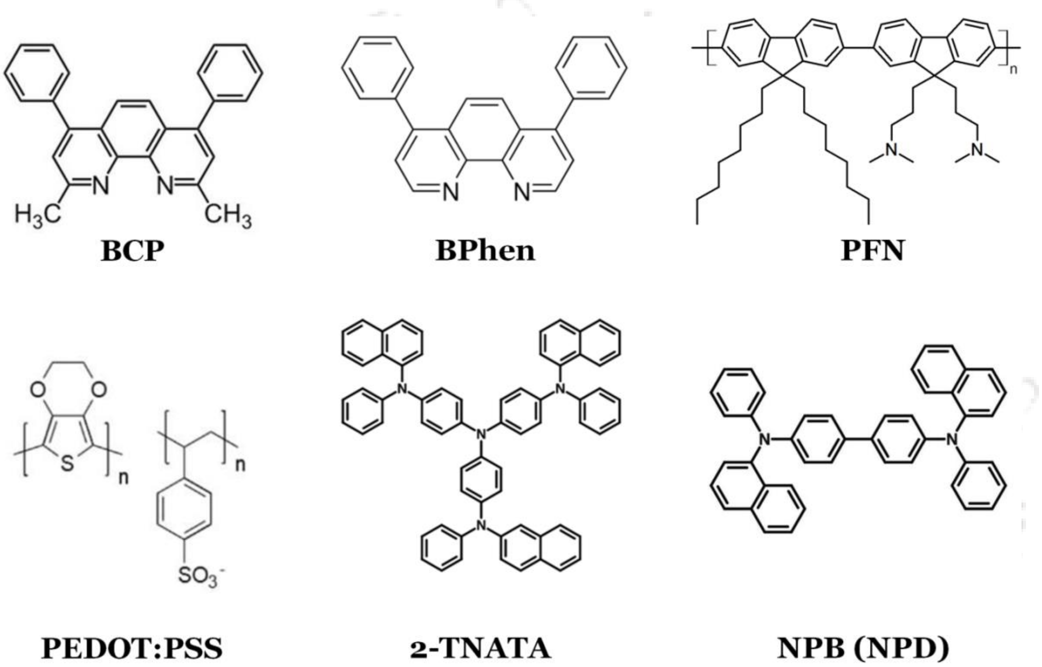
BCP **BPhen** **PFN**

PEDOT:PSS **2-TNATA** **NPB (NPD)**

Figure 1.9. Chemical structure of electrode buffer layers used in OSC application.

Generally in literature, three different types of materials, namely, alkali metal compounds, metal oxides and organic materials are used for modulating the EIL. This all are together termed as cathode buffer layers (CBL). Lithium Fluoride (LiF) combined with Aluminum metal is a well-known conventional cathode contact which was first reported for OLED device application.[48,49] For organic solar cells incorporation of a very thin layer of LiF layer (~1.5 nm) along with Aluminium can able to improved PCE by over 20% by simultaneously increasing the FF and V_{OC} by reducing the series resistance across the contact. [50] There are may be two possible reasons for such improvement- (1) formation of dipole layer which lowers the energy barrier between the Fermi level of the metal and the LUMO level of the acceptor, thereby helping electron transfer and (2) the doping of the underlying organic layer caused by LiF dissociation and diffusion. Similar like LiF, other alkali metal compounds have been proved to be qualified as efficient cathode buffer layers, such as NaF, KF, CsF, $LiCoO_{2-3}$ and Cs_2CO_3.[51-55]

Similar like alkali metal compounds, various metal oxides are also applied as cathode buffer layers for organic solar cell fabrication. A TiO_X interlayer has been extensively used as a CBL in OSC. TiO_X possess some inherent properties like large energy gap (~3.7 eV with LUMO -4.4 eV and HOMO -8.1 eV), transparent film forming ability which makes its one of the demanding CBL for BHJ application. Zinc oxide is another inherently n-type, high bandgap semiconductor, with electronic properties similar to those of TiO_X.[56] For TiO_X and ZnO buffer layers, an additional role is an optical spacer.[57, 58] This type of spacer can tune the position of the photoactive layer to make it locate at the maximum optical field, which results in a better absorption and a higher efficiency of exciton generation.[59, 60]

Another kind of cathode buffer materials is organic small molecules, like Bathocuproine (BCP) or Bathophenanthroline (BPhen). A layer of these compounds is named exciton blocking layer (EBL) according to their working mechanism. Both these materials are transparent to the visible and near-IR solar spectrum due to their wide *Eg*. Its bandgap is substantially larger than those of the organic donors and acceptors, which blocks excitons in the organic semiconducting layer from the cathode avoiding any quenching effect at the organic/cathode interface. Moreover, holes can also be blocked by a barrier originated from the HOMO difference between these organic small molecules and the donor. The LUMO offset between BCP or BPhen and the acceptor will be an energy barrier for electrons to reach the Aluminium cathode, provided that electron transport via LUMO levels. Another role of these types EBL is that it can protect the organic film from metal atom diffusion when the cathode is thermally deposited. Moreover it may fill pinholes, cracks and other defects, which suppress the leakage current.

1.5.4 Incorporation of Plasmonic Metal Nanoparticles (NPs)

Light trapping in organic BHJ solar cells has become an interesting solution to increase its PCE value. Several techniques have been proposed for light trapping in OSC, such as the inclusion of periodic nanostructures, diffraction gratings, metallic nanoparticles and a combination of gratings and metallic nanoparticles. Similar to the use of blend active material to achieve extended absorption, better charge separation, and improved charge transport, the application of the plasmonic effect through the use of noble metal NPs is another valuable route to improve light harvesting within the absorption range of a given organic BHJ solar cell.

Specifically, the inclusion of metallic nanoparticles can enhance the absorption of the light by two mechanisms: an increasing of the forward scattering cross section and a near-field enhancement (Figure 1.10). When the metallic particles are very similar or smaller in size than the wavelength of the light of interest, a strong interaction occurs between the free conduction electrons in the metal and the electromagnetic radiation. Plasmons are the oscillations of these free conduction electrons with the generation of a dipole into the particles due to the interaction with the light (Figure 1.11).

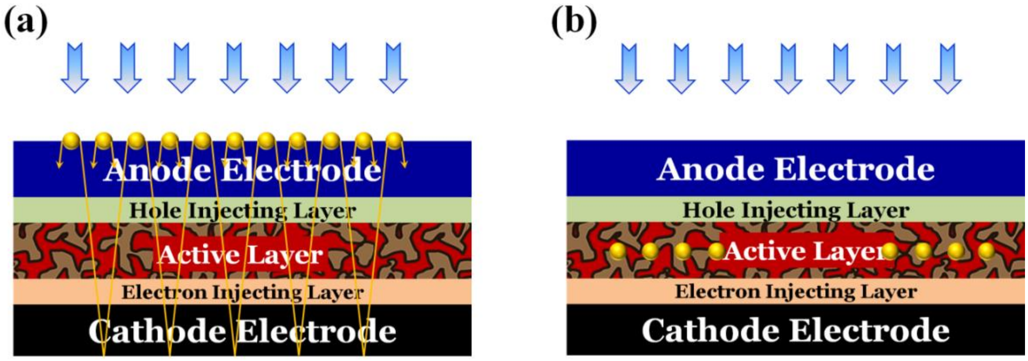

Figure 1.10. (a) Light trapping by scattering from metallic nanoparticles at the surface of a standard organic solar cell. The optical path length is increased because light is trapped into the device through multiple angle scattering. (b) Excitation of localized surface plasmons in metallic nanoparticles embedded in the organic solar cell.

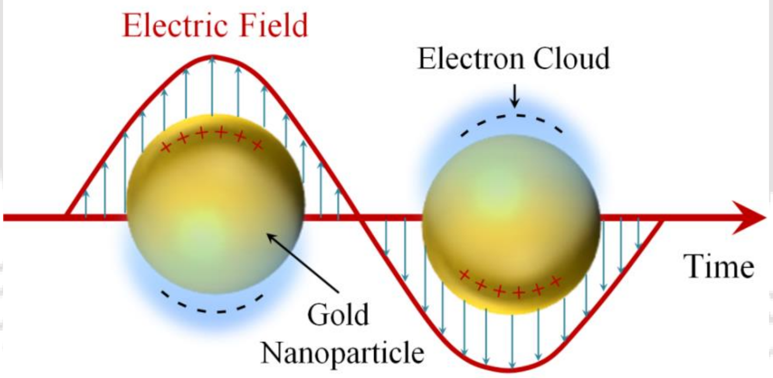

Figure 1.11. Schematic of surface plasmon resonance where the free conduction electrons in the metal nanoparticles are driven into oscillation due to the strong coupling with incident light.

The resonance condition occurs when the frequency of the light matches the frequency of the electrons oscillating and is defined as localized surface plasmon resonance (LSPR) in the case of nanometre sized structures. LSPR from noble metal NPs and nanostructures enhances the electromagnetic field and thus facilitates light absorption, generating excess excitons inside the solar cell. In addition, metal NPs or nanostructures can scatter incident photons to generate longer propagation pathways. Further, the main advantage of the use of metallic nanoparticles does not compromise the architecture of the devices because they can be easily added to one of the organic solar cell layers. Indeed, metal nanostructures have received great attention due to their extraordinary optical properties. In particular, Ag and Au NPs with different sizes, shapes, surface modifications, and concentrations are widely integrated into different layers of Organic BHJ solar cells to achieve enhanced absorption.

1.6 Thesis Synopsis

Considering the demand of present day technology, this thesis mainly focused on the modulation of cathode and anode buffer layers to improve the BHJ solar cell performance of commonly studied system, namely, regioregular poly (3-hexylthiophene-2, 5-diyl) (rrP3HT):[6, 6]-Phenyl $C_{61/71}$ butyric acid methyl ester ($PC_{61/71}BM$). The main research results are detailed in seven chapters of this thesis, the contents of which can be outlined below -

In bulk heterojunction (BHJ) solar cells, the molar mass ratio of donor-acceptor polymers, the annealing temperature and the cathode buffer layer plays very consequential role in ameliorating the power conversion efficiency (PCE) by tuning the film morphology and enhancing the charge carrier dynamics. A comprehensive understanding of each of these factors is very essential in order to optimize the performance of organic solar cells (OSCs). Albeit there are several fundamental reports regarding these factors, an altogether felicitous correlation of these physical processes with experimental evidence of the photo active layer are required. In **Chapter 2**, the influence of different molar mass ratio, the annealing temperature and the single cathode buffer layer of rrP3HT:$PC_{71}BM$ based BHJ solar cells and their corresponding photovoltaic performances were systematically correlated with their thin film growth structure and energy level diagram. The observations of this chapter prosperously explicate the cumulate role of all these physical parameters and their conbined contribution to the PCE amendment and overall device performance with rrP3HT:$PC_{71}BM$ based organic BHJ solar cell.

The **Chapter 3** demonstrated a new concept of incorporating dual cathode buffer layer in harvesting the PCE value of rrP3HT:PCBM based BHJ solar cell. In this study, three different additional buffer layers viz., Tris(8-hydroxyquinolinato) aluminum (Alq3) or Bathophenanthroline (BPhen) or Bathocuproine (BCP) were incorporated with LiF/Al as conventional cathode contact in both rrP3HT:$PC_{61}BM$ and rrP3HT:$PC_{71}BM$ blend BHJ solar cells and their corresponding photovoltaic performances were systematically correlated with their energy level diagram. It has been observed that the device with BCP/LiF/Al as dual cathode buffer layer showed the best device performance for both the with rrP3HT:$PC_{71}BM$ and rrP3HT:$PC_{61}BM$ system which is due to the combined effects of better hole-blocking capacity of BCP and low work function provided by LiF/Al with the blend polymer. These results successfully explain the role of dual cathode buffer layers and their contribution to the PCE improvement and overall device performance with rrP3HT:PCBM based BHJ solar cell.

Chapter 4 demonstrated the combined influence of plasmon induced metallic nanoparticles (NPs) and dual cathode buffer layers for significantly improving the PCE of rrP3HT:PCBM based BHJ solar cells. In this chapter PEDOT:PSS, the anode buffer layer is basically modulated by metal NPs and their effect in presence of dual cathode buffer layer are analyzed. Two different types of metal NPs, viz. citrate capped gold (Au) and silver (Ag) NPs were blended (20 v/v %) separately in the hole transport layer PEDOT:PSS. For the dual cathode buffer layer, two different hole blocking layers were chosen, BPhen and BCP, along with LiF/Al cathode contact. The combined influence of both the NPs as well as the dual cathode buffer layers were investigated with two blend polymers, rrP3HT:$PC_{61}BM$ and rrP3HT:$PC_{71}BM$. It was observed that for both the blend polymer systems the PCE increases significantly in the presence of PEDOT:PSS + AuNPs and PEDOT:PSS + AgNPs with BCP/LiF/Al as the cathode contact compared to the bare PEDOT:PSS layer. Especially, in the presence of PEDOT:PSS + AuNPs and BCP/LiF/Al, the highest PCE was observed for both the blend polymers because of the better band alignment of BCP/LiF/Al with the active layers and the superior surface plasmon resonance of the AuNPs at the visible spectrum compared to AgNPs. These results conclusively explain the combined influence of dual cathode buffer layer and the plasmonic metal NPs to remarkably improve the PCE and overall device performance of rrP3HT:PCBM based BHJ solar cells.

In **Chapter 5**, the collective effect of plasmon induced dual metal nanoparticles (NPs) and the dual cathode buffer layers on improving PCE of rrP3HT:PCBM based BHJ solar cell were systematically demonstrated. Here, initially, two different types of metal NPs, viz. citrate capped gold (Au) and silver (Ag) NPs were separately synthesized and then physically blend together with three different volume ratio [AuNPs + AgNPs (25:75), AuNPs + AgNPs (50:50) and AuNPs + AgNPs (75:25)]. These three blended NPs solution are then mixed together in the PEDOT:PSS (20 v/v %) hole transport layer to form three new NPs doped hole injecting layers and their effect on the performance of rrP3HT:PCBM based BHJ solar cell was systamatically analysed. The plasmonic metal nanoparticles were incorporated in the PEDOT:PSS layer to improve photo current of the fabricated BHJ solar cell by increasing optical absroption and scattering inside the devices. For dual cathode buffer layer, two different hole blocking layers, BPhen and BCP were used for enhanced charge collection along with LiF/Al cathode contact. The combined influence of both the dual NPs as well as the dual cathode buffer layers were investigated with two blend polymers, rrP3HT:PC$_{61}$BM and rrP3HT:PC$_{71}$BM. It was observed that for both the blend polymer systems the PCE increases significantly in presence of PEDOT:PSS + AuNPs:AgNPs (25:75) with BCP/LiF/Al as the cathode contact compared to others because of the better band alignment of BCP/LiF/Al with the active layers and the superior surface plasmon resonance of the AuNPs:AgNPs (25:75) at the UV-visible spectrum compared to AuNPs:AgNPs (50:50) and AuNPs:AgNPs (75:25). These results conclusively explained a very simple technique in which the collective effect of dual plasmonic metal NPs and dual cathode buffer layer to remarkably improve the PCE and overall device performance of rrP3HT:PCBM based BHJ solar cells is shown.

Chapter 6 demonstrated the combine effect of different shaped plasmonic Gold nanoparticles (AuNPs) and the dual cathode buffer layers on improving the PCE of rrP3HT:PCBM based BHJ solar cells. Two different blend polymers, namely, rrP3HT:PC$_{61}$BM and rrP3HT:PC$_{71}$BM were used here along with BPhen and BCP as the buffer layers of the convensional LiF/Al cathode contact. Initially, four different shaped AuNPs, viz. CTAB capped gold nanorod (AuNRs), nanosphere (AuNSs), nano-oval (AuNOs) and nano branch (AuNBs) were separately mixed together in the PEDOT:PSS hole transport layer to form four new NPs doped hole injecting layers and their effect on the performance of rrP3HT:PCBM based BHJ solar cell was systamatically analysed. The synthesized nanoparticles were characterised by various caracterization technique viz., UV-Vis absorption study, FESEM and TEM analysis. The intention of varying the shape of the NPs were to improve the photo current by light scattering phenomanon inside the BHJ solar cell. It was observed that for both the blend polymer systems the PCE increases significantly in presence of PEDOT:PSS + AuNRs with BCP/LiF/Al as the cathode contact compared to others because of the better band alignment of BCP/LiF/Al with the active layers and the superior surface plasmon resonance of the AuNRs at the UV-visible spectrum compared to AuNSs, AuNOs and AuNBs. These results successively explain the influence of shape of AuNPs to magnify the PCE value of rrP3HT:PCBM based BHJ solar cells with dual cathode buffer layers.

The **Chapter** 7 consisted of epilogue of the thesis. This chapter concludes the thesis with a summary of the main research results. A brief discussion on the exciting future prospects of Plasmonic BHJ Solar Cell at the subnanoscale is included at the end.

1.7 References

1. Becquerel, E. On Electric Effects under the Influence of Solar Radiation. *C. R. Acad. Sci.* **1839**, *9*, 561.

2. Fritts, C. E. On a New Form of Selenium Cell, and some Electrical Discoveries made by its use. *Am. J. Sci.* **1883**, *26*, 465-472.

3. Chapin, D. M; Fuller, C. S.; Pearson, G. L. A New Silicon P-N Junction Photocell for Converting Solar Radiation into Electrical Power. *J. Appl. Phys.* **1954**, *25*, 676.

4. Green, M. A. Silicon Photovoltaic Modules: A Brief History of the First 50 Years. *Prog. Photovolt: Res. Appl.* **2005**, 13, 447–455.

5. Heeger, A. J. Semiconducting Polymers: the Third Generation. *Chem. Soc. Rev.* **2010**, *39*, 2354–2371.

6. Arias, A. C.; MacKenzie, J. D.; McCulloch, I.; Rivnay, J.; Salleo, A. Materials and Applications for Large Area Electronics: Solution-Based Approaches. *Chem. Rev.* **2010**, *110*, 3–24.

7. Tobjörk, D.; Österbacka, R. Paper Electronics. *Adv. Mater.* **2011**, *23*, 1935–1961.

8. Shaheen, S. E.; Ginley, D. S.; Jabbour, G. E. Organic-based Photovoltaics: Toward Low-Cost Power Generation. *MRS Bull.* 2005, 30, 10.

9. Shirakawa, H.; Louis, E. J.; MacDiarmid, A. G.; Chiang, C. K.; Heeger, A. J. Synthesis of Electrically Conducting Organic Polymers : Halogen Derivatives of Polyacetylene, $(CH)_X$. *J. Chem. Soc., Chem. Commun.* **1977**, *0*, 578-580.

10. Green, M. A. Third Generation Photovoltaics: Solar Cells for 2020 and Beyond. *Physica E* **2002**, *14*, 65–70.

11. Jayawardena, K. I.; Rozanski, L. J.; Mills, C. A.; Beliatis, M. J.; Nismy, N. A.; Silva, S. R. P. 'Inorganics-in-Organics': Recent Developments and Outlook for 4G Polymer Solar Cells. *Nanoscale* **2013**, *5*, 8411–8427.

12. Notarianni, M.; Vernon, K.; Chou, A.; Aljada, M.; Liu, J.; Motta, N. Plasmonic Effect of Gold Nanoparticles in Organic Solar Cells. *Sol. Energy* **2014**, *106*, 23–37.

13. Pacios, R.; Marcilla, R.; Pozo-Gonzalo, C.; Pomposo, J. A.; Grande, H.; Aizpurua, J.; Mecerreyes, D. Combined Electrochromic and Plasmonic Optical Responses in Conducting Polymer/Metal Nanoparticle Films. *J. Nanosci. Nanotechnol.* **2007**, *7*, 2938–2941.

14. Truong, N. T. N.; Nguyen, T. P. N.; Park, C. Structural and Optoelectronic Properties of CdSe Tetrapod Nanocrystals for Bulk Heterojunction Solar Cell Applications. *Int. J. Photoenergy* **2013**, *2013*, 7.

15. Liu, Y.; Zhang, F.; Wang, J. Organic Photovoltaic Cells Based on PbPc Nanocolumns Prepared by Glancing Angle Deposition. *Int. J. Photoenergy* **2013**, *2013*, 6.

16. Sarah, M. S. P.; Zahid, F. S. S.; Rusop, M. Investigation on I-V for Different Heating Temperatures of Nanocomposited MEH-PPV:CNTs Organic Solar Cells. *Int. J. Photoenergy* **2012**, *2012*, 6.

17. Heo, S. W.; Baek, K. H.; Lee, T. H.; Lee, J. Y.; Moon, D. K. Enhanced Performance in Inverted Polymer Solar Cells via Solution Process: Morphology Controlling Of PEDOT:PSS as Anode Buffer Layer by Adding Surfactants. *Org. Electron.* **2013**, *14*, 1629–1635.

18. Jung, J. W.; Lee, J. U.; Jo, W. H. High-Efficiency Polymer Solar Cells with Water-Soluble and Self-Doped Conducting Polyaniline Graft Copolymer as Hole Transport Layer. *J. Phys. Chem. C* **2010**, *114*, 633–637.

19. Andreoli, E.; Liao, K.-S.; Haldar, A.; Alley, N. J.; Curran, S. A. Ppy:PSS as Alternative to PEDOT:PSS in Organic Photovoltaics. *Synth. Met.* **2013**, *185*, 71-78.

20. Lu, L.; Luo, Z.; Xu, T.; Yu, L. Cooperative Plasmonic Effect of Ag and Au Nanoparticles on Enhancing Performance of Polymer Solar Cells. *Nano Lett.* **2013**, *13*, 59–64.

21. Sun, J.; Zhu, Y. ;Xu, X.; Lan, L.; Zhang, L.; Cai, P.; Chen, J.; Peng, J.; Cao Y. High Efficiency and High V_{oc} Inverted Polymer Solar Cells Based on a Low-Lying HOMO Polycarbazole Donor and a Hydrophilic Polycarbazole Interlayer on ITO Cathode. *J. Phys. Chem. C* **2012**, 116, 14188–14198.

22. Chuchmała, A.; Palewicz, M.; Sikora, A.; Iwan A. Influence of Graphene Oxide Interlayer on PCE Value of Polymer Solar Cells. *Synth. Met.* **2013**, *169*, 33–40.

23. Iwan, A.; Chuchmała, A. Perspectives of Applied Graphene: Polymer Solar Cells. Prog. Polym. Sci. **2012**, *37*, 1805–1828.

24. Devasia, A.; Kurinec, S. K. Teaching Solar Cell I-V Characteristics using SPICE. *Am. J. Phys.* **2011**, *79*, 1232–1239.

25. Walker, G. Evaluating MPPT Topologies using a MATLAB PV Mode. *J. Electr. Electron. Eng., Aust.* **2001**, *21*, 49-55.

26. Kamarzaman, N. A.; Tan, C. W. A Comprehensive Review of Maximum Power Point Tracking Algorithms for Photovoltaic Systems. *Renewable Sustainable Energy Rev.* **2014**, *37*, 585–598.

27. van Dyk, E. E.; Meyer, E. L. Analysis of the effect of Parasitic Resistances on the Performance of Photovoltaic Modules. *Renew. Energy* **2004**, *29*, 333–344.

28. Gregg ,B. A. Excitonic Solar Cells. *J. Phys. Chem. B* **2003**, *107*, 4688-4698.

29. Marks, R. N.; Halls, J. J. M.; Bradley, D. D. C.; Friend, R. H.; Holmes A. B. The Photovoltaic Response in Poly(p-Phenylene Vinylene) Thin-Film Devices. *J. Phys.: Condens. Matter* **1994**, *6*, 1379.

30. Tang, C. W. Two-Layer Organic Photovoltaic Cell. *Appl. Phys. Lett.* **1986**, *48*, 183–185.

31. Peumans, P.; Yakimov, A.; Forrest, S. R. Small Molecular Weight Organic Thin-Film Photodetectors and Solar Cells. *J. Appl. Phys.* **2003**, *93*, 3693–3723.

32. Sariciftci, N. S.; Smilowitz, L.; Heeger, A. J.; Wudl, F. Photoinduced Electron Transfer from a Conducting Polymer to Buckminsterfullerene. *Science* **1992**, *258*, 1474–1476.

33. Yu, G.; Heeger, A. J. Charge Separation and Photovoltaic Conversion in Polymer Composites with Internal Donor/Acceptor Heterojunctions. *J. Appl. Phys.* **1995**, *78*, 4510–4515.

34. Li, G.; Shrotriya, V.; Huang, J. S.; Yao, Y.; Moriarty, T.; Emery, K.; Yang, Y. High-Efficiency Solution Processable Polymer Photovoltaic Cells by Self-Organization of Polymer Blends. *Nat. Mater.* **2005**, *4*, 864–868.

35. Kim, Y.; Cook, S.; Tuladhar, S. M.; Choulis, S. A.; Nelson, J.; Durrant, J. R.; Bradley, D. D.; Giles, M.; McCulloch, I.; Ha, C. S.; Ree, M. A Strong Regioregularity Effect in Self-Organizing Conjugated Polymer Films and High-Efficiency Polythiophene: Fullerene Solar Cells. *Nat. Mater.* **2006**, *5*, 197–203.

36. Armaroli, N.; Balzani, V. The Future of Energy Supply: Challenges and Opportunities. *Angew. Chem., Int. Ed.* **2007**, *46*, 52–66.

37. Nunzi, J.-M. Organic Photovoltaic Materials and Devices. *C. R. Phys.* **2002**, *3*, 523–542.

38. Shockley, W.; Queisser, H. J. Detailed Balance Limit of Efficiency of p-n Junction Solar Cells. *J. Appl. Phys.* **1961**, *32*, 510–519.

39. Dennler, G.; Scharber, M. C.; Brabec, C. J. Polymer-Fullerene Bulk-Heterojunction Solar Cells. *Adv. Mater.* **2009**, *21*, 1323–1338.

40. Yu, G.; Gao, J.; Hummelen, J. C.; Wudl, F.; Heeger, A. J. Polymer Photovoltaic Cells: Enhanced Efficiencies via a Network of Internal Donor-Acceptor Heterojunctions. *Science* **1995**, *270*, 1789–1791.

41. Huang, Y.; Kramer, E. J.; Heeger, A. J.; Bazan, G. C. Bulk Heterojunction Solar Cells: Morphology and Performance Relationships. *Chem. Rev.* **2014**, *114*, 7006–7043.

42. Heeger, A. J. 25th Anniversary Article: Bulk Heterojunction Solar Cells: Understanding the Mechanism of Operation. *Adv. Mater.* **2014**, *26*, 10–28.

43. Chen, W.; Nikiforov, M. P.; Darling, S. B. Morphology Characterization in Organic and Hybrid Solar Cells. *Energy Environ. Sci.* **2012**, *5*, 8045–8074.

44. Yip, H.-L.; Jen, A.-K. Y. Recent Advances in Solution-Processed Interfacial Materials for Efficient and Stable Polymer Solar Cells. *Energy Environ. Sci.* **2012**, *5*, 5994–6011.

45. Lai, Y.-Y.; Cheng, Y.-J.; Hsu, C.-S. Applications of Functional Fullerene Materials in Polymer Solar Cells. *Energy Environ. Sci.* **2014**, *7*, 1866–1883.

46. Duan, C.; Zhang, K.; Zhong, C.; Huang, F.; Cao, Y. Recent Advances in Water/Alcohol-Soluble π-Conjugated Materials: New Materials and Growing Applications in Solar Cells. *Chem. Soc. Rev.* **2013**, *42*, 9071–9104.

47. Chen, S.; Manders, J. R.; Tsang, S.-W.; So, F. Metal Oxides for Interface Engineering in Polymer Solar Cells. *J. Mater. Chem.* **2012**, *22*, 24202–24212.

48. Hung, L. S.; Tang, C. W.; Mason M. G. Enhanced Electron Injection in Organic Electroluminescence Devices Using an Al/LiF Electrode. *Appl. Phys. Lett.* **1997**, *70*, 152-154.

49. Jabbour, G.; Kawabe, Y.; Shaheen, S.; Wang, J.; Morrell, M.; Kippelen, B.; Peyghambarian, N. Highly Efficient and Bright Organic Electroluminescent Devices with an Aluminum Cathode. *Appl. Phys. Lett.* **1997**, *71*, 1762-1764.

50. Brabec, C. J.; Shaheen, S. E.; Winder, C.; Sariciftci, N. S.; Denk, P. Effect of LiF/Metal Electrodes on the Performance of Plastic Solar Cells. *Appl. Phys. Lett.* **2002**, *80*, 1288-1290.

51. Ahlswede, E.; Hanish, J.; Powalla, M. Comparative Study of the Influence of LiF, NaF, and KF on the Performance of Polymer Bulk Heterojunction Solar Cells. *Appl. Phys. Lett.* **2007**, *90*, 163504(1-3).

52. Jiang, X.; Xu, H.; Yang, L.; Shi, M.; Wang M.; Chen, H. Effect of CsF Interlayer on the Performance of Polymer Bulk Heterojunction Solar Cells. *Sol. Energy Mater. Sol. Cells,* **2009**, *93*, 650-653.

53. Hanisch, J.; Ahlswede, E.; Powalla, M. All-Sputtered Contacts for Organic Solar Cells. *Thin Solid Films,* **2008**, *516*, 7241-7244.

54. Huang, J.; Xu, Z.; Yang, Y. Low-work-Function Surface Formed by Solution-Processed and Thermally Deposited Nanoscale Layers of Cesium Carbonate. *Adv. Funct. Mater.* **2007**, *17*, 1966-1973.

55. Chen, F.-C.; Wu, J.-L.; Yang, S. S.; Hsieh, K.-H.; Chen, W.-C. Cesium Carbonate as a Functional Interlayer for Polymer Photovoltaic Devices. *J. Appl. Phys.* **2008**, *103*, 103721(1-5).

56. Kim, J. Y.; Kim, S. H.; Lee, H.-H.; Lee, K.; Ma, W.; Gong, X.; Heeger, A. J. New Architecture for High-Efficiency Polymer Photovoltaic Cells using Solution-Based Titanium Oxide as an Optical Spacer. *Adv. Mater.* **2006**, *8*, 572-576.

57. Hayakawa, A.; Yoshikawa, O.; Fujieda, T.; Uehara, K.; Yoshikawa, S. High Performance Polythiophene/Fullerene Bulk-Heterojunction Solar Cell with A TiO_x Hole Blocking Layer. *Appl. Phys. Lett.* **2007**, *90*, 163517(1-3).

58. Kim, S. H.; Park, S. H.; Lee, K. Efficiency Enhancement in Polymer Optoelectronic Devices by Introducing Titanium Sub-Oxide Layer. *Curr. Appl. Phys.* **2010**, *10*, S528-S531.

59. Snaith, H. J.; Greenham, N. C.; Friend, R. H. The Origin of Collected Charge and Open-Circuit Voltage in Blended Polyfluorene Photovoltaic Devices. *Adv. Mater.* **2004**, *16*, 1640-1645.

60. Roy, A.; Park, S. H.; Cowan, S.; Tong, M.H.; Cho, S.; Lee, K. Heeger, A. J. Titanium Suboxide as an Optical Spacer in Polymer Solar Cells. *Appl. Phys. Lett.* **2009**, *95*, 013302(1-3).

Chapter 2

Influence of Molar Mass Ratio, Annealing Temperature and Cathode Buffer Layer on PCE of Organic BHJ Solar Cell

Research efforts towards organic semiconductor based thin film solar cells has enhanced dynamically in last few decades, due to their low-cost, interesting properties in terms of light, simple fabrication and compatibility with large-area and flexible substrates.[1-3] Among various types of organic solar cells, bulk hetero junction (BHJ) is one of the most promising one because of their facile fabrication processing and minutely diminutive amount of material requisite for making roll-to-roll printing.[4,5] Additionally, many organic semiconductors exhibiting very high absorption coefficients used as active materials in BHJ, are easily tuneable at the molecular level using different synthesis techniques.[6-8] However, in comparison with inorganic semiconductor based solar cells, for the commercialization of BHJ solar cells, several essential factors viz., improved power conversion efficiency (PCE), active layer stability, device lifetime etc. are yet to be boosted up.[9-13] Especially, for improving the PCE value of any BHJ solar cell, the controlled molar mass ratio of donor-acceptor blend polymers, the annealing temperature (T_{an}) and the cathode buffer layer plays very consequential role and by tuning the factors one can really modify the active layer morphology and the charge transport and finally the PCE value of the cell.

Among various reported BHJ active materials, the blend of regioregular poly(3-hexylthiophene) (rrP3HT) with (6,6)-phenylC_{61}-butyric acid methyl ester ($PC_{61}BM$) is one of the widely studied systems due to their unique property of good interpenetrating network forming capacity in nanoscale morphology range and large interfacial areas for efficient exciton dissociation. However, there only few reports where (6,6)-phenylC_{71}-butyric acid methyl ester ($PC_{71}BM$) was used as acceptor along with P3HT for the fabrication of BHJ solar cell where it is showing poor PCE compared to $PC_{61}BM$. Compared to $PC_{61}BM$, $PC_{71}BM$ has lower unoccupied molecular orbital (LUMO) energy level ($E_{LUMO,PC71BM}$=3.9 eV and $E_{LUMO,PC61BM}$=3.7 eV) and lower electron mobility (μ_{PC71BM}=0.1 cm²/V·s and μ_{PC61BM}=0.21 cm²/V·s) due to which it showed reduced open circuit voltage, V_{oc} and fill factor value (FF) as a result of which its PCE value decreases. Moreover, due to unsymmetrical structure of $PC_{71}BM$ it also showed poor thin film morphological property compared to $PC_{61}BM$. Therefore, in order to obtained efficient device performance and better PCE with P3HT:$PC_{71}BM$ based organic BHJ solar cell, a comprehensive understanding of its thin film growth morphology and charge transport mechanism is very essential.[14-17]

In this Chapter, we systematically analysed the influence of different molar mass ratio, the annealing temperature (T_{an}) and the cathode buffer layer on the photovoltaic performance rrP3HT:$PC_{71}BM$ based BHJ solar cells and their output properties, which were further justified by their thin film growth structure and energy level diagram. It has been observed that the device having molar mass ratio 1:0.8 and annealed at 150°C with Bathocuproine (BCP)/Aluminium (Al) as the cathode contact showed the best device performance with PCE, η= 4.79%, J_{sc}=14.21 mA/cm², V_{oc}= 0.58 V and FF= 57.8% This drastic enhancement in PCE of the devices having BCP/Al as the cathode contact compared to the other device configurations is due to the coalesced effects of better hole-blocking capacity of BCP/Al and better phase separation of the active blend layer at T_{an}=150°C with 1:0.8 molar mass concentration. These results successfully explicate the cumulate role of all these physical parameters and their combined influence to the PCE amendment and overall device performance with rrP3HT:$PC_{71}BM$ based organic BHJ solar cell.

2.1 Experiments

2.1.1 Materials

In this chapter, for device fabrication, the hole injecting material, Poly (3, 4-ethylenedioxythiophene)-poly (styrene sulfonate) (PEDOT:PSS) and Indium tin oxide (ITO) covered glass substrate (R_{Sheet}~15Ω/sq.), were purchased from Sigma Aldrich, India. The cathode material Aluminium wire (99.999% purity) and the buffer layers, Lithium Fluoride (LiF) (≥99.99% trace metals basis), Calcium (Ca) (99.99% trace metals basis), Bathocuproine (BCP) (M_w~360.45 g/mol), and Bathophenanthroline (BPhen) (M_w~332.40 g/mol) were also purchased from Sigma Aldrich, India and used as received. The acceptor material, [6, 6]-Phenyl C_{71} butyric acid methyl ester ($PC_{71}BM$) (M_w~1030.93 g/mol, 99.5% pure) and the donor material, regioregular poly (3-hexylthiophene-2, 5-diyl) (rrP3HT) (M_w~83 kg/mol) were purchased from Luminescence Technology Corp., Taiwan and Sycon Polymers India Pvt Ltd respectively. Tris (8-hydroxyquinolinato) Aluminium (Alq3) was synthesized by following the literature method.[18]

2.1.2 Characterization Details

Laurell and Spin 150 spin coaters were used for the deposition of PEDOT:PSS and the blend polymers on ITO coated glass substrate. Veeco Dektak 150 Surface Profilometer was used to measure thicknesses of the thin films. Jaz UV-Vis spectrophotometer was used for record the thin film absorption spectra of all the blend polymers having different configuration. For photovoltaic characterisation, Newport Oriel Sol 3A solar simulator, Oriel IQE-200 instrument and CH 680 Instrument were used along with Keithley-2400 digital source meter.

2.1.3 Device Fabrication

The rrP3HT:$PC_{71}BM$ based BHJ solar cells were fabricated on commercially available ITO-coated glass substrate and the schematic representation of all the device structures are shown in Figure.2.1. Four different types of blend polymer solution having different molar mass ratio i.e., P3HT:$PC_{71}BM$= 1:0.6, 1:0.8, 1:1.0 and 1:1.2 were prepared in 1, 2-diclorobenzene and stirred for 48 hours in hot plate at 60°C. After blending, all the active material solutions were filtered with 0.45 µm PTFE filter before use.

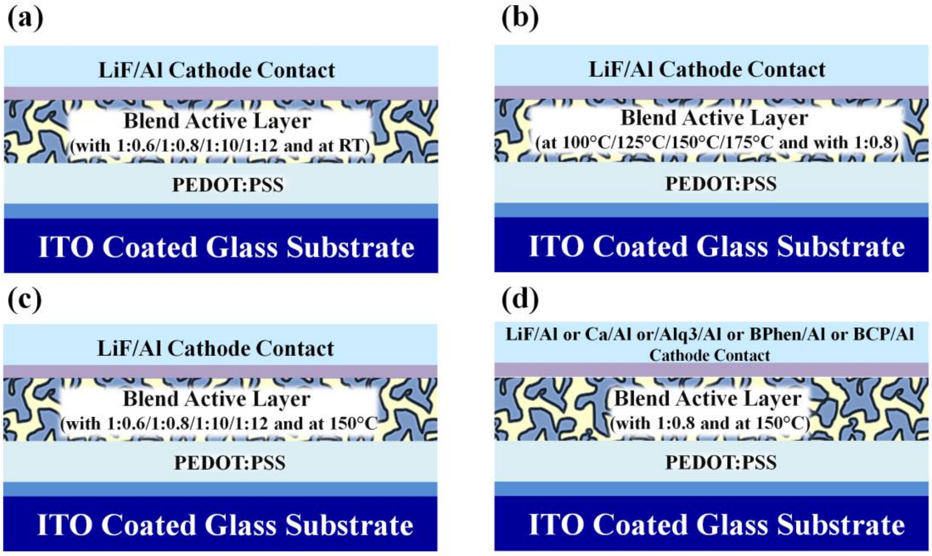

Figure 2.1. Schematic of the fabricated rrP3HT:PC$_{71}$BM based BHJ organic solar cell with (a) different donor-acceptor molar mass ratio at RT, (b) at different T$_{an}$ with 1:0.8 donor-acceptor molar mass ratio, (c) different donor-acceptor molar mass ratio and at T$_{an}$=150°C and (d) at T$_{an}$=150°C and donor-acceptor molar mass ratio 1:0.8 with different cathode contact.

For device fabrication, the ITO substrates were first patterned by chemical etching method with Zinc dust and dilute HCl (1:1) solution and then cleaned by ultrasonic cleaner in successive solutions of detergent, de-ionized water, acetone and isopropanol. After cleaning the substrates were dried in inert atmosphere and then UV-ozone treatment was carried out for ~20 minutes in order to improve the work function and the hydrophilic nature of the surface. Following this, PEDOT:PSS was spin coated at 3000 rpm and dried at 120°C for 30 minutes. After that four different sets of devices were prepared (Table 2.1)-

a. After PEDOT:PSS layer the active material solutions having different molar mass ratio were spin coated at 1000 rpm and dried under room temperature (RT) overnight under argon atmosphere. Followed by this LiF/Al (1nm/100nm) cathode contact was deposited (Figure. 2.1a).
b. For studying the effect of annealing temperature, after PEDOT:PSS layer, four substrates were prepared with blend polymer having molar mass ratio (1:0.8) and then annealed at four different temperature separately using four different hot plates i.e., at 100°C, 125°C, 150°C and 175°C for 30 min. Followed by this LiF/Al (1nm/100nm) cathode contact was deposited (Figure. 2.1b).

c. Again in order to find out the effect of molar mass ratio of the blend polymer at 150°C, same procedure like point (a) was repeated and all the substrates were annealed at 150°C for 30 min. Followed this LiF/Al (1nm/100nm) cathode contact was deposited (Figure. 2.1c).

d. Finally, to find out the effect of cathode buffer layer again five PEDOT:PSS coated substrates were prepared with molar mass ratio 1:0.8 and T_{an}=150°C. Followed by this different cathode contact i.e., LiF/Al (1nm/100nm), Ca/Al (10nm/100nm), Alq3/Al (5nm/100nm), BPhen/Al (5nm/100nm) and BCP/Al (5nm/100nm) cathode contact were thermally evaporated under base pressure of ~10^{-6} mbar through a shadow mask determining the active area of the device ~6 mm^2(Figure. 2.1d).

Table 2.1. List of the fabricated BHJ device configurations with rrP3HT:$PC_{71}BM$ blend active polymers.

Variation	**Device Configuration**
(1) At Room Temperature with Variable Molar Mass Concentration	(a) ITO/PEDOT:PSS /rrP3HT:$PC_{71}BM$ (1:0.6)/LiF/Al at RT
	(b) ITO/PEDOT:PSS /rrP3HT:$PC_{71}BM$ (1:0.8)/LiF/Al at RT
	(c) ITO/PEDOT:PSS /rrP3HT:$PC_{71}BM$ (1:1.0)/LiF/Al at RT
	(d) ITO/PEDOT:PSS /rrP3HT:$PC_{71}BM$ (1:1.2)/LiF/Al at RT
(2) At Constant Molar Mass Concentration and Variable Annealing Temperatures	(a) ITO/PEDOT:PSS /rrP3HT:$PC_{71}BM$ (1:0.8)/LiF/Al at 100°C
	(b) ITO/PEDOT:PSS /rrP3HT:$PC_{71}BM$ (1:0.8)/LiF/Al at 125°C
	(c) ITO/PEDOT:PSS /rrP3HT:$PC_{71}BM$ (1:0.8)/LiF/Al at 150°C
	(d) ITO/PEDOT:PSS /rrP3HT:$PC_{71}BM$ (1:0.8)/LiF/Al at 175°C
(3) At Constant 150°C Annealing Temperatures with Variable Molar Mass Concentration	(a) ITO/PEDOT:PSS /rrP3HT:$PC_{71}BM$ (1:0.6)/LiF/Al at 150°C
	(b) ITO/PEDOT:PSS /rrP3HT:$PC_{71}BM$ (1:0.8)/LiF/Al at 150°C
	(c) ITO/PEDOT:PSS /rrP3HT:$PC_{71}BM$ (1:1.0)/LiF/Al at 150°C
	(d) ITO/PEDOT:PSS /rrP3HT:$PC_{71}BM$ (1:1.2)/LiF/Al at 150°C
(4) At Constant 150°C Annealing Temperatures And Constant Molar Mass Concentration (1:0.8) with different Cathode Contact	(a) ITO/PEDOT:PSS /rrP3HT:$PC_{71}BM$ (1:0.8)/LiF/Al at 150°C
	(b) ITO/PEDOT:PSS /rrP3HT:$PC_{71}BM$ (1:0.8)/Ca/Al at 150°C
	(c) ITO/PEDOT:PSS /rrP3HT:$PC_{71}BM$ (1:0.8)/Alq3/Al at 150°C
	(d) ITO/PEDOT:PSS /rrP3HT:$PC_{71}BM$ (1:0.8)/BPhen/Al at 150°C
	(e) ITO/PEDOT:PSS /rrP3HT:$PC_{71}BM$ (1:0.8)/BCP/Al at 150°C

2.2 Results and Discussion

2.2.1 Thin Film Characterization

The thin film UV-Vis absorption spectra of rrP3HT:$PC_{71}BM$ blend polymers with different donor-acceptor molar mass concentration at room temperature, with different annealing temperature at weight ratio 1:0.8 and with different donor-acceptor molar mass ratio and at constant T_{an}=150°C are shown in Figure. 2.2.

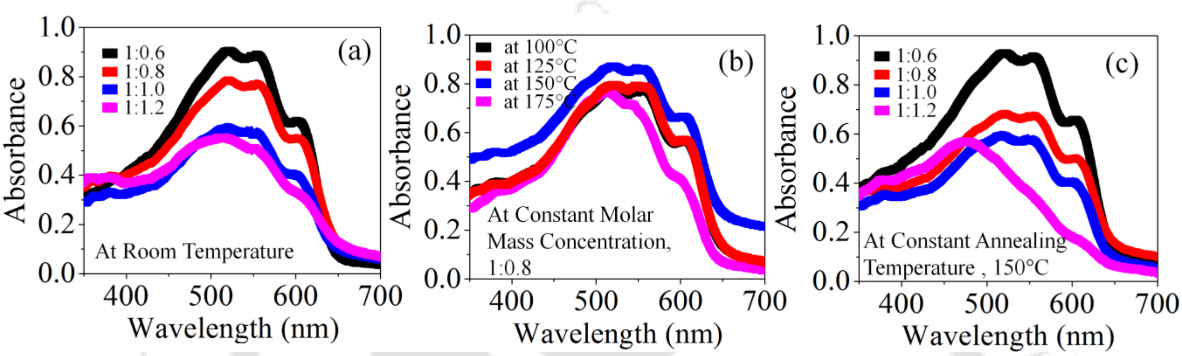

Figure 2.2. Thin film UV-Visible absorption spectra of rrP3HT:$PC_{71}BM$ with (a) different donor-acceptor molar mass ratio at RT, (b) at different annealing temperature with constant 1:0.8 donor-acceptor molar mass ratio and (c) different donor-acceptor molar mass ratio and at constant annealing temperature 150°C.

It was observed from Figure. 2.2a and Figure 2.2c that with the increase of $PC_{71}BM$ concentration a quenching in the absorption of the blends were observed which can be attributed to the interaction between the rrP3HT and $PC_{71}BM$, as $PC_{71}BM$ has absorption intensity near ultra-violet region where as P3HT has in the visible region. On the other hand, in Figure. 2.2b upon increasing the annealing temperature gradually from 100°C to 175°C, the absorption intensity again increases with a red-shift up to 150°C and then decreases at 175°C with a shift towards blue side.

Generally the π-π* transition of the P3HT backbone signifies the absorption peak band. This increased absorption after annealing is believed to be due to the improvement of crystallinity of P3HT donor polymer caused by the diffusion of $PC_{71}BM$ molecules by heat treatment leads to more π-π* absorption.[19-23] As a result highest crystallinity and maximum absorption were observed at an annealing temperature of 150°C. Further increase in the temperature from 150°C to 175°C, more phase separation are occur as a result absorption intensity decreases. This result is also supported by AFM analysis (Figure. 2.3). From Figure. 2.3a-Figure. 2.3h it has been observed that the 150°C and 1:0.8 is the optimum condition of P3HT:$PC_{71}BM$ thin film for BHJ solar cell fabrication as at this condition the film showed lowest surface roughness (σ_{rms}=21 nm) and better phase separation compared to the others.

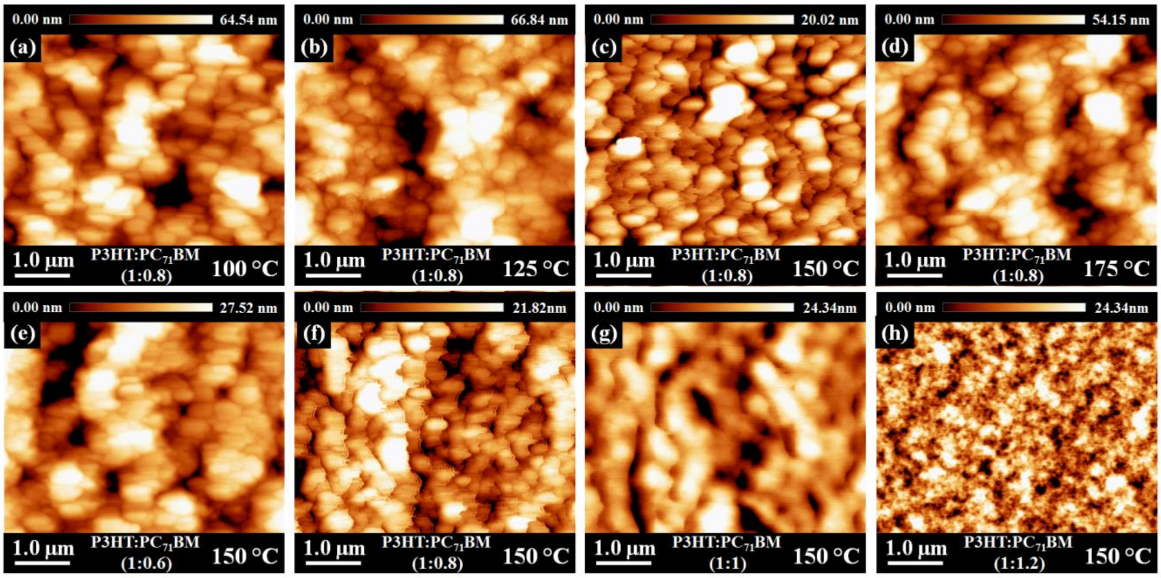

Figure 2.3. AFM topographic images of rrP3HT:PC71BM with (a-d) different T_{an} with constant 1:0.8 donor-acceptor molar mass ratio and (e-h) different donor-acceptor molar mass ratio and at constant Tan= 150°C.

2.2.2 Photovoltaic Characterizations

Figure. 2.4, 2.5 and 2.6 represents the photovoltaic properties of all the fabricated BHJ devices. In this study, total seventeen different device structures were systematically analysed which are listed in Table 2.1. From Figure. 2.4a it was observed that at room temperature with the variation of molar mass ratio of the blend active polymer very minor variation in current density can be achieved. From the device having configuration (1b), the highest PCE was observed to be η=2.88% with J_{sc}=10.33 mA/cm^2, V_{oc}=0.53 V and FF= 52.17% with 1:0.8 as the molar mass ratio. In the next step, by keeping constant 1:0.8 molar mass ratio and varying the annealing temperature, it has been observed that only by changing the T_{an} from RT to 150°C, the PCE increases from η=2.88% to 3.94% with J_{sc}=12.39 mA/cm^2, V_{oc}=0.54 V and FF= 58.41% [Figure. 2.4b and device configuration (2c)]. Figure. 2.4c signifies the variation of current density with respect to different molar mass ratio at constant T_{an}= 150°C. From this data it can be concluded that, the T_{an}= 150°C, and molar mass ratio= 1:0.8 are the optimum value for rrP3HT:PC$_{71}$BM blend polymer where the obtained highest photovoltaic parameters are, PCE, η=3.84% with J_{sc}=12.97 mA/cm^2, V_{oc}=0.55 V and FF= 53.81% [device configuration (3b)] without any contact modification. In the fourth step (Figure. 2.4d), with these optimum conditions, we studied the effect of different cathode buffer layers on the output performance of the cells.[24-29] The energy band diagram of all these buffer layers along with the rrP3HT:PC$_{71}$BM blend polymers are schematically described in Figure. 2.5.

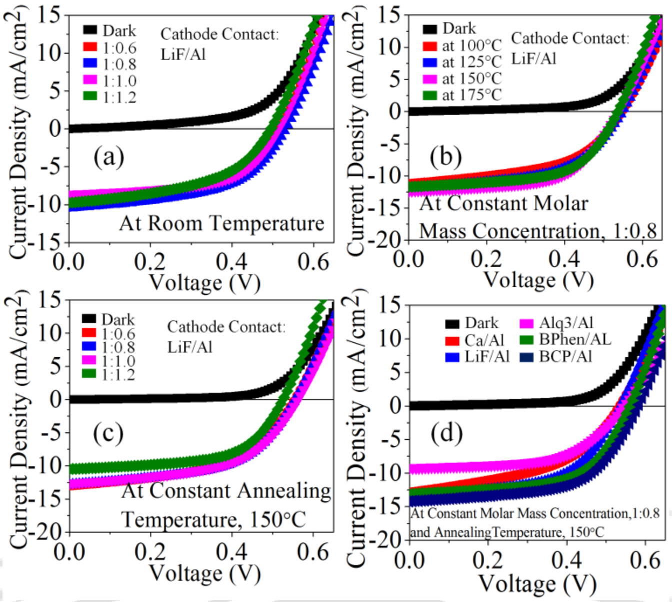

Figure 2.4. Current density vs. voltage (J-V) characteristics of rrP3HT:$PC_{71}BM$ with (a) different donor-acceptor molar mass ratio at RT, (b) at different T_{an} with constant 1:0.8 donor-acceptor molar mass ratio (c) different donor-acceptor molar mass ratio and at constant T_{an}= 150°C and (d) different cathode buffer layer and at optimum conditions.

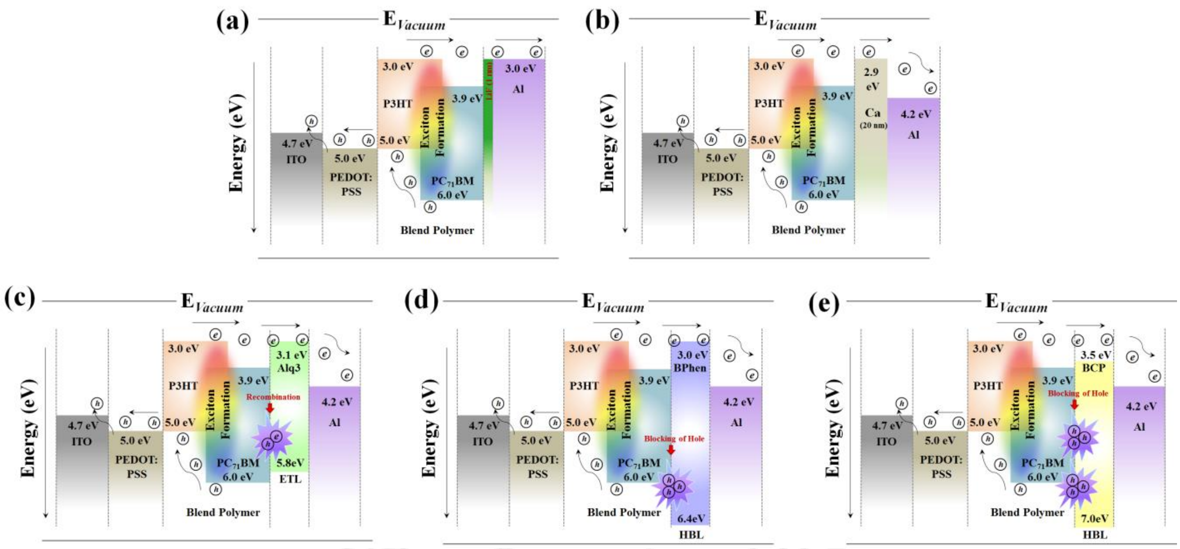

Figure 2.5. Band energy diagrams of the fabricated devices having (a) LiF/Al, (b) Ca/Al, (c) Alq3/Al (d) BPhen/Al and (e) BCP/Al as cathode buffer layer.

Using Ca/Al as cathode contact, similar types of device output were obtained [$\eta_{Ca/Al}$=3.20% having device configuration, (4b)] like LiF/Al [$\eta_{LiF/Al}$= 4.01% having device configuration, (4a)] since the work function of Ca/Al (~2.9 eV) is almost similar like LiF/Al (~3 eV) [Figure. 2.5a and Figure. 2.5b]. But with Ca/Al, the stability of the fabricated device was observed very poor compared to LiF/Al as Ca can be easily oxidized

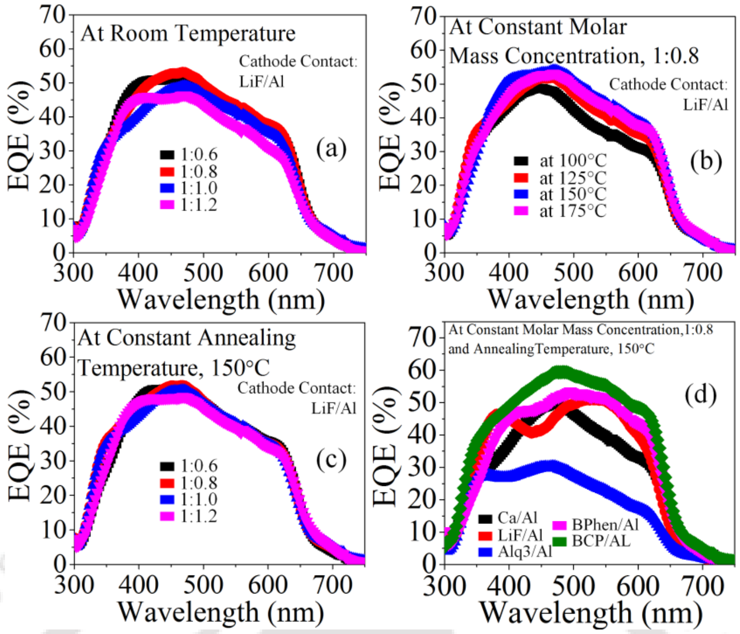

Figure 2.6. EQE spectra of rrP3HT:PC$_{71}$BM with (a) different donor-acceptor molar mass ratio at RT, (b) at different T$_{an}$ with constant 1:0.8 donor-acceptor molar mass ratio (c) different donor-acceptor molar mass ratio and at constant T$_{an}$= 150°C and (d) different cathode buffer layer and at optimum conditions.

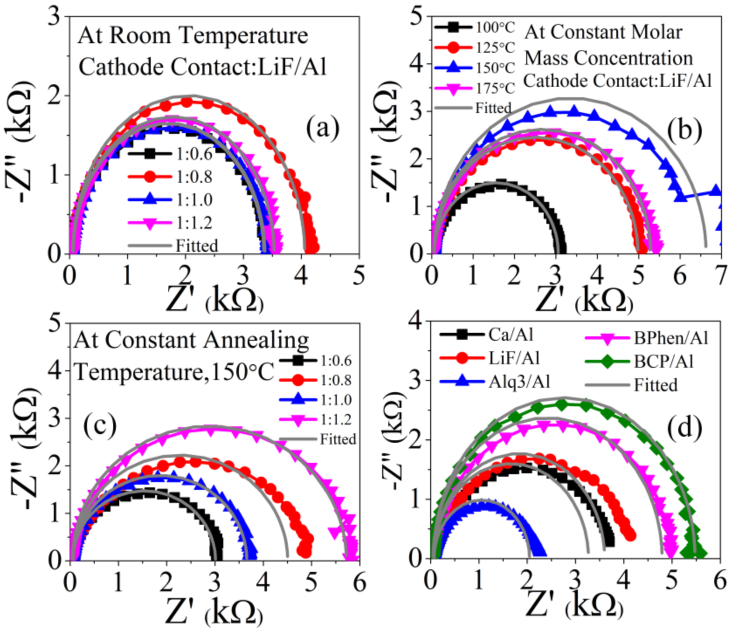

Figure 2.7. Nyquist plots of rrP3HT:PC$_{71}$BM with (a) different donor-acceptor molar mass ratio at RT, (b) at different T$_{an}$ with constant 1:0.8 donor-acceptor molar mass ratio (c) different donor-acceptor molar mass ratio and at constant T$_{an}$= 150°C and (d) different cathode buffer layer and at optimum conditions.

in ambient atmosphere. In case of Alq3/Al [having device configuration (4c)], as Alq3 is an electron injecting layer, due to the interaction of the HOMO level of this buffer material with the blend active layer, some charge carriers recombination occur at the interface (Figure. 2.5c). As a result lower PCE value ($\eta_{Alq3/Al}$=2.91%)

was observed. For the devices having configuration (4d) and (4e), we used BPhen and BCP as cathode buffer layer along with Al as cathode contact respectively. In both the cases, better photovoltaic properties were observed because of superior hole blocking capacity of these molecules due to which less charge carriers are recombined at the blend polymer-cathode contact interface. Among these two configurations, BCP/Al showed better PCE of $\eta_{BCP/Al} = 4.79\%$ with $J_{sc}=14.21$ mA/cm^2, $V_{oc}=0.58$ V and FF=57.8% compared to BPhen/Al ($\eta_{BPhen/Al}=4.36\%$) as BCP has higher band gap, due to which it shows higher selectivity towards electron and blocking the holes to minimize the charge recombination between the blend polymer-cathode contact compared to BPhen. As a result we get better band energy alignment which enhances the overall photovoltaic performance (Figure. 2.5d and Figure. 2.5e). The photovoltaic performance parameters of all the devices are summarized in Table 2.2.

Table 2.2. Summary of BHJ solar cell performance with rrP3HT:PC71BM as the active blend layer and with different variation.

Device Configuration	**J_{sc} (mA.cm^{-2})**	**V_{oc} (V)**	**FF (%)**	**PCE,η (%)**
(1)(a)	**10.20**	**0.52**	**50.62**	**2.69**
(1)(b)	**10.33**	**0.53**	**52.17**	**2.88**
(1)(c)	8.62	0.52	56.26	2.58
(1)(a)	9.75	0.50	48.02	2.34
(2)(a)	11.22	0.54	51.47	3.14
(2)(b)	11.77	0.54	54.67	3.50
(2)(c)	**12.39**	**0.54**	**58.41**	**3.94**
(2)(d)	11.72	0.54	58.06	3.70
(3)(a)	12.83	0.55	52.73	3.72
(3)(b)	**12.97**	**0.55**	**53.81**	**3.84**
(3)(c)	12.64	0.55	54.42	3.78
(3)(d)	10.48	0.53	58.45	3.25
(4)(a)	13.49	0.54	55.11	4.01
(4)(b)	12.95	0.54	45.65	3.20
(4)(c)	9.23	0.55	57.35	2.91
(4)(d)	13.18	0.57	58.43	4.36
(4)(e)	**14.21**	**0.58**	**57.8**	**4.79**

Figure. 2.6 and Figure. 2.7 represent the EQE spectra and Nyquist plots for all the fabricated BHJ devices. The EQE measurements are done outside the glove box under ambient condition. From the graphs it was observed that only varying the molar mass concentration and annealing temperature, the highest obtained quantum efficiency is ~55 % (Figure. 2.6a-2.6c). But with the influence of cathode buffer layer it improves to ~ 62% with BCP/Al as the cathode contact compared to the other (Figure. 2.6d). Also from the Nyquist plots (Figure. 2.7) it was observed that the devices with BCP/Al contact has the largest shunt resistance as compared with other device configurations and has good correlation with its photovoltaic performance. It has been reported extensively that with the variation of molar mass concentration, the annealing temperature and cathode buffer layer can also significantly improve the photovoltaic performance of organic BHJ solar cells. There are various parameters in terms of incorporation of functional organic and inorganic materials that have been mentioned in literature to improve the device performances of BHJ solar cells.[30-35] In this study we have successfully explained the influence of different molar mass ratio, the annealing temperature (T_{an}) and the cathode buffer layer on improving the photovoltaic performance rrP3HT:$PC_{71}BM$ based BHJ solar cells. The results demonstrated here, are also successfully justified by the output properties of each of the cells, their thin film growth structure and energy level diagram. These highly efficient and reproducible organic solar cells can significantly contribute to future commercialization of organic solar cell devices.

2.3 Conclusion

In conclusion, the significant effect of different molar mass ratio, the annealing temperature (T_{an}) and the cathode buffer layer on the photovoltaic performance rrP3HT:$PC_{71}BM$ based BHJ solar cells is demonstrated. The results of these BHJ devices indicated that with 1:0.8 molar mass ratios and 150°C is the optimum annealing temperature for this particular blend polymer system for getting highest photovoltaic performance. Further with this optimum condition and with BCP/Al as cathode buffer layer the device shows maximum efficiency with of η = 4.79%, J_{sc}=14.21 mA/cm^2, V_{oc}=0.58 V and FF=57.8% due to the better hole blocking capacity of BCP and superior energy band matching of BCP/Al with the active blend. In this study we could successfully demonstrate the cumulate role of each of the physical parameters and their combined influence to the PCE amendment and overall device performance with rrP3HT:$PC_{71}BM$ based organic BHJ solar cell.

2.4 References

1. Baran, D.; Ashraf, R. S.; Hanifi, D. A.; Abdelsamie, M.; Gasparini, N.; Röhr, J. A.; Holliday, S.; Wadsworth, A.; Lockett, S.; Neophytou, M.; Emmott, C. J. M.; Nelson, J.; Brabec, C. J.; Amassian, A.; Salleo, A.; Kirchartz, T.; Durrant, J. R.; McCulloch, I. Reducing the Efficiency-Stability-Cost Gap of Organic Photovoltaics with Highly Efficient and Stable Small Molecule Acceptor Ternary Solar Cells. *Nat. Mater.* **2017**, *16*, 363–369.

2. Ma, W.; Yang, C.; Gong, X.; Lee, K.; Heeger, A. J. Thermally Stable, Efficient Polymer Solar Cells with Nanoscale Control of The Interpenetrating Network Morphology. *Adv. Funct. Mater.* **2005**, *15*, 1617–1622.

3. Yu, G.; Gao, J.; Hummelen, J. C.; Wudl F.; Heeger, A. J. Polymer Photovoltaic Cells: Enhanced Efficiencies via a Network of Internal Donor-Acceptor Heterojunctions. *Science* **1995**, *270*, 1789–1791.

4. Dennler, G.; Scharber, M. C.; Brabec, C. J. Polymer-Fullerene Bulk-Heterojunction Solar Cells. *Adv. Mater.* **2009**, *21*, 1323–1338.

5. Li, G.; Shrotriya, V.; Huang, J. S.; Yao, Y.; Moriarty, T.; Emery, K.; Yang, Y. High-Efficiency Solution Processable Polymer Photovoltaic Cells by Self-Organization of Polymer Blends. *Nat. Mater.* **2005**, *4*, 864–868.

6. Li, G.; Zhu, R.; Yang, Y. Polymer Solar Cells. *Nat. Photonics* **2012**, *6*, 153–161.

7. Mayer, A. C.; Scully, S. R.; Hardin, B. E.; Rowell, M. W.; McGehee, M. D. Polymer-based Solar Cells. *Mater. Today* **2007**, *10*, 28–33.

8. Lu, L.; Zheng, T.; Wu, Q.; Schneider, A. M.; Zhao, D.; Yu, L. Recent Advances in Bulk Heterojunction Polymer Solar Cells. *Chem. Rev.* **2015**, *115*, 12666–12731.

9. Kawashima, K.; Tamai, Y.; Ohkita, H.; Osaka, I.; Takimiya, K. High-Efficiency Polymer Solar Cells with Small Photon Energy Loss. *Nat. Commun.* **2015**, *6*, 10085.

10. Liu, J.; Chen, S.; Qian, D.; Gautam, B.; Yang, G.; Zhao, J.; Bergqvist, J.; Zhang, F.; Ma, W.; Ade, H.; Inganäs, O.; Gundogdu, K.; Gao, F.; Yan, H. Fast Charge Separation in a Non-Fullerene Organic Solar Cell with a Small Driving Force. *Nat. Energy* **2016**, *1*, 16089.

11. Baran, D.; Kirchartz, T.; Wheeler, S.; Dimitrov, S.; Abdelsamie, M.; Gorman, J.; Ashraf, R. S.; Holliday, S.; Wadsworth, A.; Gasparini, N.; Kaienburg, P.; Yan, H.; Amassian, A.; Brabec, C. J.; Durrant, J. R.; McCulloch, I. Reduced Voltage Losses Yield 10% Efficient Fullerene Free Organic Solar Cells with >1 V Open Circuit Voltages. *Energy Environ. Sci.* **2016**, *9*, 3783–3793.

12. He, Z.; Xiao, B.; Liu, F.; Wu, H.; Yang, Y.; Xiao, S.; Wang, C.; Russell, T. P.; Cao, Y. Single-junction Polymer Solar Cells with High Efficiency and Photovoltage. *Nat. Photonics* **2015**, *9*, 174–179.

13. Bin, H.; Gao, L.; Zhang, Z.-G.; Yang, Y.; Zhang, Y.; Zhang, C.; Chen, S.; Xue, L.; Yang, C.; Xiao, M.; Li, Y. Efficiency Non-Fullerene Polymer Solar Cells with Trialkylsilyl Substituted 2D-conjugated Polymer as Donor. *Nat. Commun.* **2016**, *7*, 13651.

14. Pivrikas, A.; Sariciftci, N. S.; Juška, G.; Österbacka, R. A Review of Charge Transport and Recombination in Polymer/Fullerene Organic Solar Cells. *Prog. Photovolt: Res. Appl.* **2007**, *15*, 677–696.

15. Wang, W.; Guo, S.; Herzig, E. M.; Sarkar, K.; Schindler, M.; Magerl, D.; Philipp, M.; Perlich, J.; Müller-Buschbaum, P. Investigation of Morphological Degradation of P3HT:PCBM Bulk Heterojunction Films Exposed to Long-Term Host Solvent Vapor. *J. Mater. Chem. A* **2016**, *4*, 3743–3753.

16. Wang, W.; Schaffer, C. J.; Song, L.; Körstgens, V.; Pröller, S.; Indari, E. D.; Wang, T.; Abdelsamie, A.; Bernstorff, S.; Müller-Buschbaum, P.; In Operando Morphology Investigation of Inverted Bulk Heterojunction Organic Solar Cells by GISAXS. *J. Mater. Chem. A* **2015**, *3*, 8324–8331.

17. Huang, Y.-C.; Tsao, C.-S.; Chuang, C.-M.; Lee, C.-H.; Hsu, F.-H.; Cha, H.-C.; Chen, C.-Y.; Lin, T.-H.; Su, C.-J.; Jeng, U-S.; Su, W.-F. Small- and Wide-Angle X-ray Scattering Characterization of Bulk Heterojunction Polymer Solar Cells with Different Fullerene Derivatives. *J. Phys. Chem. C* **2012**, *116*, 10238–10244.

18. Li, H.; Zhang, F.; Wang, Y.; Zheng, D. Synthesis and Characterization of Tris-(8-Hydroxyquinoline)Aluminum. *Mater. Sci. Eng. B* **2003**, *100*, 40–46.

19. Vanlaeke, P.; Swinnen, A.; Haeldermans, I.; Vanhoyland, G.; Aernouts, T.; Cheyns, D.; Deibel, C.; D'Haen, J.; Heremans, P.; Poortmans, J.; Manca, J. V. P3HT/PCBM Bulk Heterojunction Solar Cells: Relation between Morphology and Electro-Optical Characteristics. *Sol. Energy Mater. Sol. Cells* **2006**, *90*, 2150–2158.

20. Verploegen, E.; Mondal, R.; Bettinger, C. J.; Sok, S.; Toney, M. F.; Bao, Z. Effects of Thermal Annealing Upon the Morphology of Polymer–Fullerene Blends. *Adv. Funct. Mater.* **2010**, *20*, 3519–3529.

21. Goto, E.; Nakamura, S.; Kawauchi, S.; Mori, H.; Ueda, M.; Higashihara, T. Precision Synthesis of Regioregular Poly(3-hexylthiophene) with low Dispersity using a Zincate Complex Catalyzed by Nickel with the Ligand of 1,2-Bis(dicyclohexylphosphino)ethane. *J. Polym. Sci. Part A: Polym. Chem.* **2014**, *52*, 2287–2296.

22. Lai, Y.-Y.; Tung, T.-C.; Liang, W.-W.; Cheng, Y.-J. Synthesis of Poly(3-hexylthiophene), Poly(3-hexylselenophene), and Poly(3-hexylselenophene-alt-3-hexylthiophene) by Direct C–H Arylation Polymerization via N-Heterocyclic Carbene Palladium Catalysts. *Macromolecules* **2015**, *48*, 2978–2988.

23. Cui, J.; Martínez-Tong, D. E.; Sanz, A.; Ezquerra, T. A.; Rebollar, E.; Nogales, A. Relaxation and Conductivity in P3HT/PC$_{71}$BM Blends as Revealed by Dielectric Spectroscopy. *Macromolecules* **2016**, *49*, 2709–2717.

24. Brabec, C. J.; Shaheen, S. E.; Winder, C.; Sariciftci, N. S. Effect of LiF/Metal Electrodes on the Performance of Plastic Solar Cells. *Appl. Phys. Lett.* **2002**, *80*, 1288–1290.

25. Peumans, P.; Yakimov, A.; Forrest, S. R. Small Molecular Weight Organic Thin-Film Photodetectors and Solar Cells. *J. Appl. Phys.* **2003**, *93*, 3693–3723.

26. Mityashin, A.; Cheyns, D.; Rand, B. P.; Heremans, P. Understanding Metal Doping for Organic Electron Transport Layers. *Appl. Phys. Lett.* **2012**, *100*, 053305.

27. Chang, C.-C.; Lin, C.-F.; Chiou, J.-M.; Ho, T.-H.; Tai, Y.; Lee, J.-H.; Chen, Y.-F.; Wang, J.-K.; Chen, L.-C.; Chen, K.-H. Effects of Cathode Buffer Layers on the Efficiency of Bulk-Heterojunction Solar Cells. *Appl. Phys. Lett.* **2010**, *96*, 263506.

28. Madogni, V. I.; Kounouhéwa, B.; Akpo, A.; Agbomahéna, M.; Hounkpatin, S. A.; Awanou, C. N. Comparison of Degradation Mechanisms in Organic Photovoltaic Devices upon Exposure to a Temperate and a Subequatorial Climate. *Chem. Phys. Lett.* **2015**, *640*, 201–214.

29. Wang, T.; Chen, C.; Guo, K.; Chen, G.; Xu, T.; Wei, B. Improved Performance of Polymer Solar Cells by using Inorganic, Organic and Doped Cathode Buffer Layers. *Chin. Phys. B* **2016**, *25*, 038402.

30. Li, Y.; Zhao, Y.; Chen, Q.; Yang, Y.; Liu, Y.; Hong, Z.; Liu, Z.; Hsieh, Y.-T.; Meng, L.; Li, Y.; Yang, Y. Multifunctional Fullerene Derivative for Interface Engineering in Perovskite Solar Cells. *J. Am. Chem. Soc.* **2015**, *137*, 15540–15547.

31. Lin, H.-W.; Lu, C.-W.; Lin, L.-Y.; Chen, Y.-H.; Lin, W.-C.; Wong, K.-T.; Lin, F. Pyridine-based Electron Transporting Materials for Highly Efficient Organic Solar Cells. *J. Mater. Chem. A* **2013**, *1*, 1770–1777.

32. Graetzel, M.; Janssen, R. A. J.; Mitzi, D. B.; Sargent, E. H. Materials Interface Engineering for Solution-Processed Photovoltaics. *Nature* **2012**, *488*, 304–312.

33. Kang, R.; Oh, S.-H.; Kim, D.-Y. Influence of the Ionic Functionalities of Polyfluorene Derivatives as a Cathode Interfacial Layer on Inverted Polymer Solar Cells. *ACS Appl. Mater. Interfaces* **2014**, *6*, 6227–6236.

34. Kim, I.; Haverinen, H. M.; Li, J.; Jabbour, G. E. Enhancement of Device Performance of Organic Solar Cells by an Interfacial Perylene Derivative Layer. *ACS Appl. Mater. Interfaces* **2010**, *2*, 1390–1394.

35. Mateker, W. R.; McGehee, M. D. Progress in Understanding Degradation Mechanisms and Improving Stability in Organic Photovoltaics. *Adv. Mater.* **2017**, *29*, 1603940.

Chapter 3

Effect of Dual Cathode Buffer Layer on the Performance of Organic Bulk Heterojunction Solar Cell

In the past few decades, organic bulk heterojunction (BHJ) solar cells have gained prominence due to their low-cost, simple fabrication and compatibility with large-area and flexible substrates.[1-3] The main advantages of BHJ solar cells are their flexibility, light-weight, large-scale production, low/room temperature processing and very small amount of material requirement for making roll-to-roll printing.[4,5] Likewise, the properties of the active materials used in BHJ are easily tunable at the molecular level using different synthesis techniques.[6] However, several crucial factors such as high power conversion efficiency (PCE), stability, lifetime etc. are yet to be achieved for the commercialization of BHJ solar cells as compared to silicon solar cells.[7,8] To accomplish this, additional attention on the improvement of PCE as well as the stability of the devices is essential. Among BHJ active materials, the blend of regioregular poly(3-hexylthiophene) (rrP3HT) with (6,6)-phenylC_{61}-butyric acid methyl ester ($PC_{61}BM$) and rrP3HT with (6,6)-phenylC_{71}-butyric acid methyl ester ($PC_{71}BM$) are the most widely studied due to their good interpenetrating network forming ability with large interfacial areas for efficient exciton dissociation. However, in order to obtain efficient device performance, especially for organic BHJ solar cells, comprehensive understanding of the contact electrodes is essential.[9-11] In this regard, substantial progress has already been made, yet modulation of contact interfaces between the electrodes and the BHJ active layer still needs to be improved. Buffer layer includes several important modifications in BHJ like tuning the work function of the electrode, improving the selectivity toward holes or electrons, improving device stability etc. The combination of Lithium fluoride / Aluminum (LiF/Al) is widely used as a cathode electrode for rrP3HT:PCBM based BHJs, where LiF plays the role of cathode buffer layer. LiF/Al helps to improve the short circuit current density (J_{sc}), open circuit voltage (V_{oc}), and overall power conversion efficiency (PCE) by driving the majority carriers towards their respective electrode through built-in voltage generated by the electrode work function difference.[12] However, there still exist opportunities for increasing the PCE by collecting photo generated charge carriers by modulating the cathode contact with additional buffer layer.[13]

In this Chapter, we incorporated three different additional buffer layers viz., Tris(8-hydroxyquinolinato) aluminum (Alq3) or Bathophenanthroline (BPhen) or Bathocuproine (BCP) with LiF/Al as conventional cathode contact in both rrP3HT:$PC_{61}BM$ and rrP3HT:$PC_{71}BM$ blend BHJ solar cells and their corresponding photovoltaic performances were systematically correlated with their energy level diagram.

3.1 Experiments

3.1.1 Materials

Indium tin oxide (ITO) coated glass substrate (having sheet resistance 15 Ω/sq.), Poly(3,4-ethylenedioxythiophene)-poly(styrene sulfonate) (PEDOT:PSS), [6,6]-Phenyl C_{61} butyric acid methyl ester ($PC_{61}BM$) (M_W ~910.88 g/mol, 99.5% pure), Bathocuproine (BCP) (M_W ~360.45 g/mol) Bathophenanthroline (BPhen) (MW~ 332.40 g/mol), Lithium fluoride (LiF) and Aluminum wire (99.999% purity) were purchased from Sigma Aldrich India and used as received. [6,6]-PhenylC_{71}-butyric acid methyl ester ($PC_{71}BM$) (MW~1030.93 g/mol, 99.5% pure) were purchased from Luminescence Technology Corp., Taiwan. Regioregular poly(3-hexylthiophene-2,5-diyl) (rrP3HT) (M_W~83 kg/mol) were used as received from Sycon Polymers India Pvt Limited. Tris(8-hydroxyquinolinato) Aluminum (Alq3) was synthesized by following the literature method.[14]

3.1.2 Characterization Details

The thin film of PEDOT:PSS and the blend polymers namely rrP3HT:PC$_{61}$BM and rrP3HT:PC$_{71}$BM were deposited on ITO coated glass substrate by spin coating technique using Laurell and Spin 150 spin coater outside and inside the Jacomax glove box. The Veeco Dektak 150 Surface Profilometer was used to measure thicknesses of the thin films. UV-Visible absorption spectra of thin film of the blend polymers were recorded on a Jaz UV-Vis spectrophotometer. AFM images of the thin films were recorded by Agilent 5500-STM instrument. All the electrical properties were characterized by Keithley-2400 digital source meter. Newport, Oriel Sol 3A solar simulator with an Oriel 500 W xenon lamp, connected to AM 1.5 Globe filter, was used as solar cell characterization. Newport Oriel IQE-200 instrument was used for external quantum efficiency (EQE) measurement. CH 680 Instrument was used to measure the impedance spectroscopy of all the devices.

3.1.3 Device Fabrication

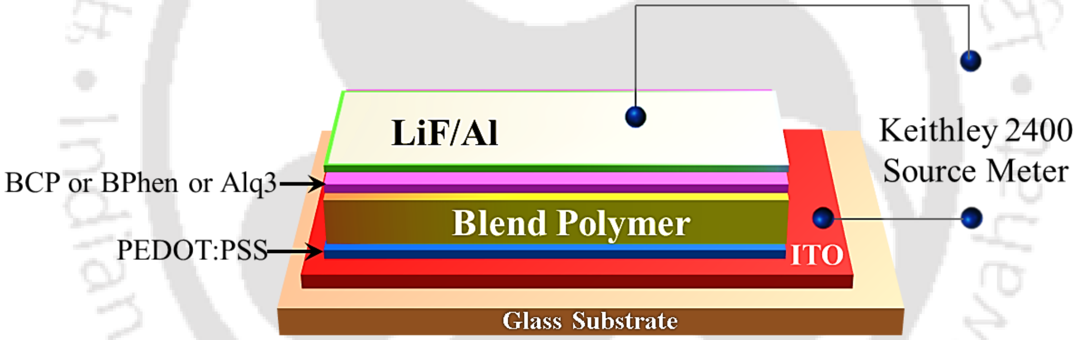

Figure 3.1. Schematic representation of the fabricated rrP3HT:PC$_{61}$BM and rrP3HT:PC$_{71}$BM blend polymer BHJ organic solar cell.

A schematic device representation of P3HT:PCBM (blend polymer) based solar cells with additional cathode buffer layer is shown in Figure 3.1. The BHJ solar cells were fabricated with rrP3HT:PC$_{61}$BM and rrP3HT:PC$_{71}$BM, according to the following procedure. The commercially available ITO-coated glass electrodes were first manually patterned by scotch tape, using diluted HCl (1:1) and Zinc dust (Figure 3.2). The patterned substrates were then cleaned by ultrasonic cleaner in successive solutions of soap, de-ionized water, acetone and isopropanol. Following this, after drying the substrate under argon atmosphere they were subjected to UV-ozone treatment for about 20 minutes in order to improve the work function of the substrates and to increase the hydrophilic nature of the surface. After this treatment, PEDOT:PSS, the hole injecting buffer layer, was spin coated at 3000 rpm for 60 seconds on the ITO and dried at 120°C for 30 minutes in argon atmosphere to improve the hole collection from the polymer to the ITO.

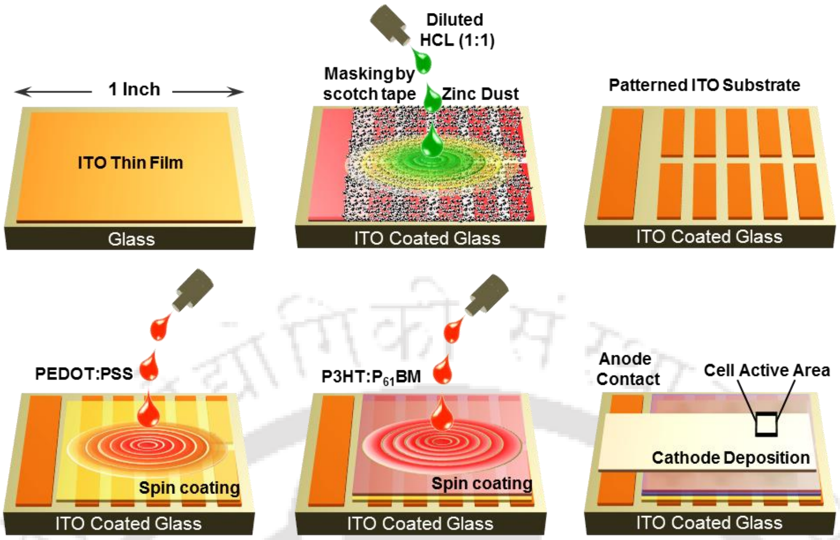

Figure 3.2. Schematic of device fabrication process.

Both the blend polymer solutions were prepared in 1,2-dichlorobenzene (o-DCB) solvent with weight ratio of 1:0.8 and stirred for 48 h at 60°C inside the glove box. After blending, the solutions were filtered with 0.45μm PTFE filter and immediately spun over PEDOT:PSS buffer layer. The thickness of the active layer was optimized at 110(±5) nm, confirmed by Surface Profilometer. In order to demonstrate the impact of different additional buffer layers with LiF/Al cathode contact on the photovoltaic device performances, solar cells were fabricated using the same procedure except for the choice of the hole blocking and electron injecting layers. We used BCP and BPhen as hole blocking layer and Alq3 as electron injecting layer. After spin coating, the active layers were first annealed at 150 °C for 10 min and subsequently, the different cathode buffer layers, namely BCP or BPhen or Alq3 were thermally evaporated. Finally, ~100 nm thin film of LiF/Al (LiF = 1 nm and Al = 100 nm) cathode electrodes were thermally evaporated under base pressure of ~10^{-6} mbar through a shadow mask determining the active area of the device ~6 mm^2.

3.2 Results and Discussion

3.2.1 Thin Film Characterization

UV-Vis analysis: The UV-Vis absorption spectra of rrP3HT:PC_{61}BM and rrP3HT:PC_{71}BM blend polymers (wt. ratio 1:0.8) were recorded in both solution state and thin films mode

(Figure 3.3). UV-Vis spectra of rrP3HT, $PC_{61}BM$ and $PC_{71}BM$ in solution were also recorded as reference. A quenching of the absorption in both these blends was observed which can be attributed to the interaction between the rrP3HT and PCBM. It was also observed that the absorption of the thin film has a red-shift compared to the absorption in solution, attributed to the increase in solid state molecular packing of rrP3HT with PCBM.[15]

AFM analysis: The AFM images of all the additional cathode buffer layers over rrP3HT:$PC_{61}BM$ and rrP3HT:$PC_{71}BM$ were recorded and shown in Figure 3.4 a-c and Figure 3.4 d-f respectively. It has been observed that among all the additional cathode buffer layers, rrP3HT:PCBM/Alq3 (Figure 3.4a and Figure 3.4d) thin film has the smallest R.M.S. roughness ($\sigma_{r.m.s.}$=7.89 nm and 9.07 nm) that forms very uniform film. On the other hand rrP3HT:PCBM/BPhen (Figure 3.4b and Figure 3.4e) showed larger grains and higher surface roughness ($\sigma_{r.m.s.}$= 11.74 nm and 14.88 nm). In case of rrP3HT:PCBM/BCP (Figure 3.4c and Figure 3.4f) the R.M.S. roughness of the film is less than BPhen and almost equal to the Alq3 buffer layer. Additionally, BCP is seen forming larger grain size compared to the Alq3 and almost equal to BPhen. It has already been mentioned in several reports that, in case of organic BHJ solar cells, high surface roughness and less grain size of cathode buffer layer resists the charge transport from photoactive layer to the cathode contact.[16] Because of this the BCP/LiF/Al dual cathode buffer layer shows higher efficiency electrical output with both the blend polymer systems.

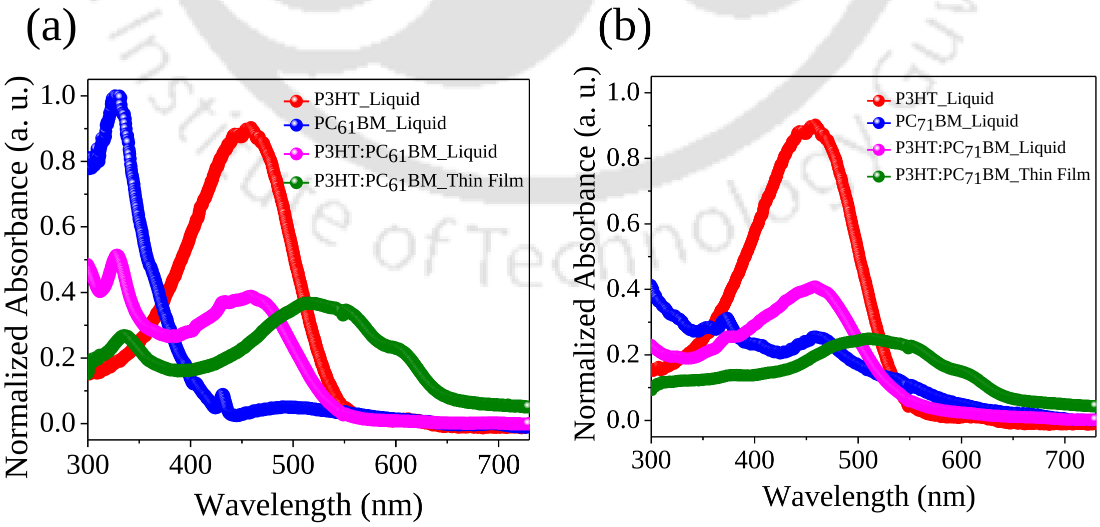

Figure 3.3. UV-Vis absorption spectra of (a) rrP3HT, $PC_{61}BM$, rrP3HT:$PC_{61}BM$ (solution) and rrP3HT:$PC_{61}BM$ thin film and (b) rrP3HT, $PC_{71}BM$, rrP3HT:$PC_{71}BM$ (solution) and rrP3HT:$PC_{71}BM$ thin film.

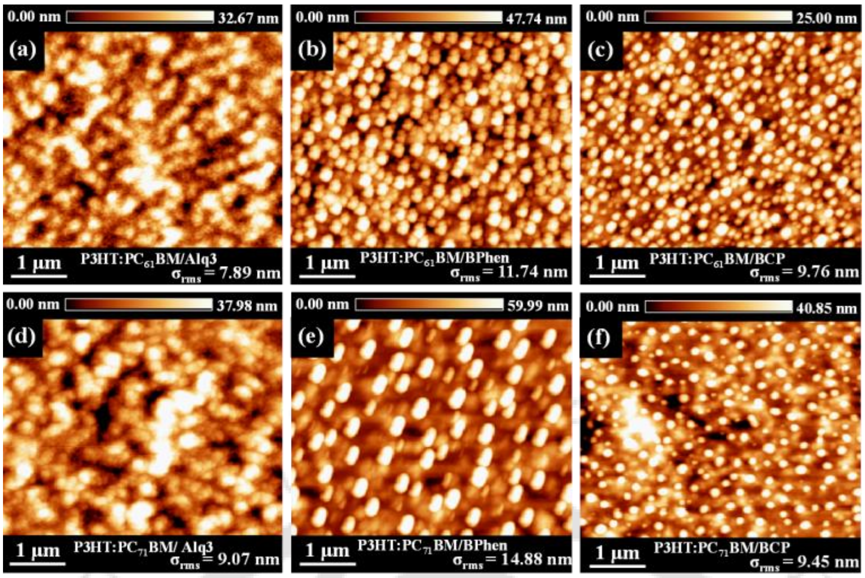

Figure 3.4. AFM images of (a) Alq3 (b) BPhen and (c) BCP on rrP3HT:PC$_{61}$BM and (d) Alq3 (e) BPhen and (f) BCP on rrP3HT:PC$_{71}$BM blend polymer thin film.

For reference the AFM images of ITO substrate, ITO with PEDOT:PSS layer and the active layers PC$_{61}$BM and PC$_{71}$BM were also recorded (Figure 3.5).

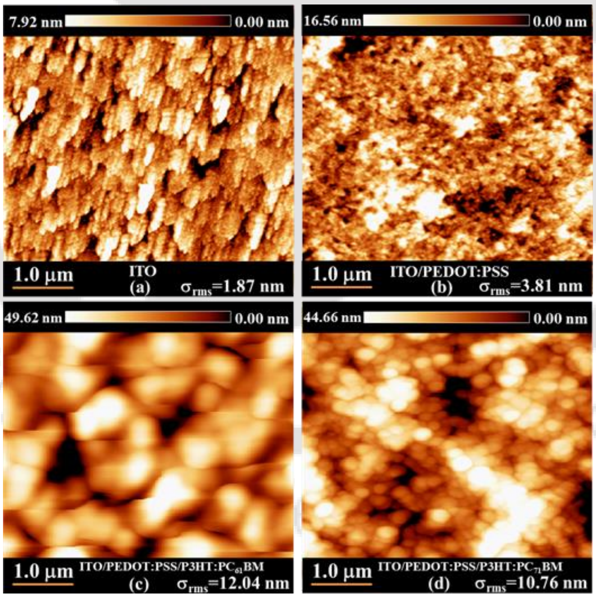

Figure 3.5. AFM image of (a) ITO coated glass substrate (b) ITO/PEDOT:PSS (c) ITO/PEDOT:PSS/rrP3PH:PC$_{61}$BM and (d) ITO/PEDOT:PSS/rrP3PH:PC$_{71}$BM.

The AFM of rrP3HT:PC$_{61}$BM and rrP3HT:PC$_{71}$BM films were recorded after thermal annealing at 150 °C for 10 min. Both these films were highly ordered with good phase separation. From these images, it was clearly visible that the blend polymers contain clusters of PCBM signifying excellent blending of PCBM with rrP3HT polymer.[17].

3.2.2 Photovoltaic Characterizations

Figure 3.6, 3.7 and 3.8 displayed the current density-voltage (J-V) characteristics, EQE spectra and the Nyquist plots of all the fabricated devices. Herein, we have fabricated devices with four different configurations, (i) ITO (150 nm) /PEDOT:PSS (40 nm) /Blend Polymer (110 nm) /LiF (1 nm) /Al(100 nm), (ii) ITO (150 nm) /PEDOT:PSS (40 nm) /Blend Polymer (110 nm) /Alq3 (6 nm) /LiF (1 nm) /Al (100 nm), (iii) ITO (150 nm) /PEDOT:PSS (40 nm) /Blend Polymer (110 nm) /BPhen (6 nm) /LiF (1 nm) /Al (100 nm) and (iv) ITO (150 nm) /PEDOT:PSS (40 nm) /Blend Polymer (110 nm) /BCP (6 nm) /LiF (1 nm) /Al (100 nm) with rrP3HT:$PC_{61}BM$ and rrP3HT:$PC_{71}BM$ respectively. The Nyquist plots, for all the BHJs, demonstrate good concurrence for higher charge transport with different additional cathode buffer electrodes. Generally, the shunt resistance of the device can be estimated from the diameter of the semicircle under its test conditions.[18-21] It has been observed that the devices with BCP/LiF/Al contact has the largest shunt resistance as compared with other device configurations and has good correlation with its photovoltaic performance.

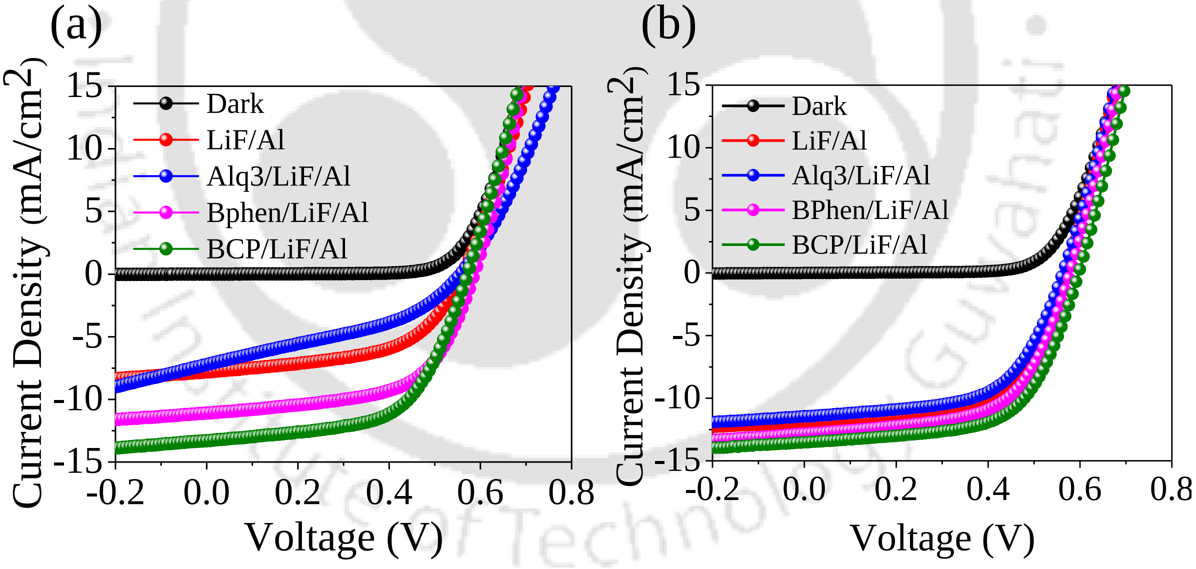

Figure 3.6. Current density-Voltage (J-V) characteristics curves of (a) rrP3HT:$PC_{61}BM$ and (b) rrP3HT:$PC_{71}BM$ solar cell with different dual cathode buffer layer.

For the device, having configuration (i), fabricated with only LiF/Al electrodes (shown in Figure 3.9 (i)), the PCE was observed to be η=2.4% with J_{sc}=7.8 mA/cm², V_{oc}=0.57 V and FF= 54% for rrP3HT:$PC_{61}BM$, whereas for rrP3HT:$PC_{71}BM$ it was observed to be η=4.04% with J_{sc}=11.9 mA/cm², V_{oc}=0.57 V and FF= 60%. We consider this device configuration as the conventional solar cell and compared the performances of other fabricated devices under identical conditions with this device.

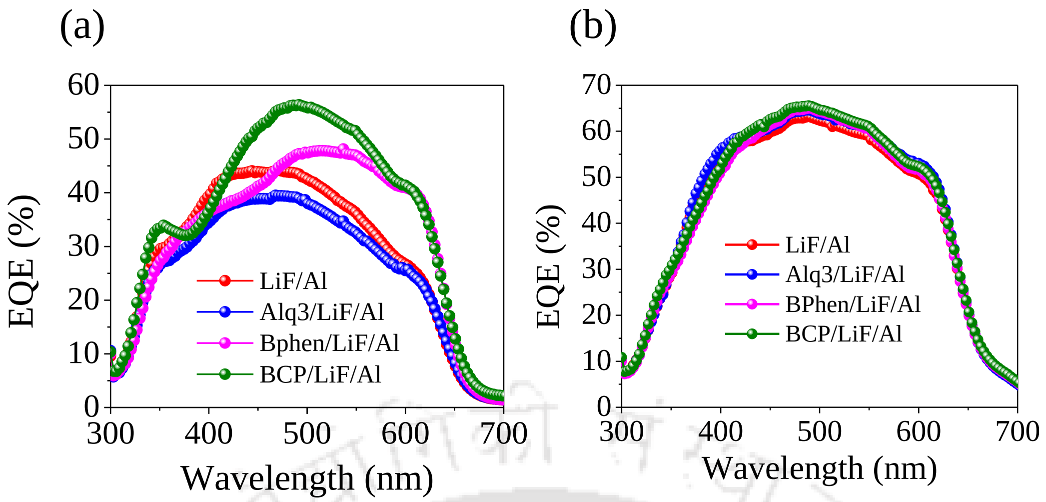

Figure 3.7. EQE spectra of (a) rrP3HT:PC$_{61}$BM and (b) rrP3HT:PC$_{71}$BM solar cell with different dual cathode buffer layer.

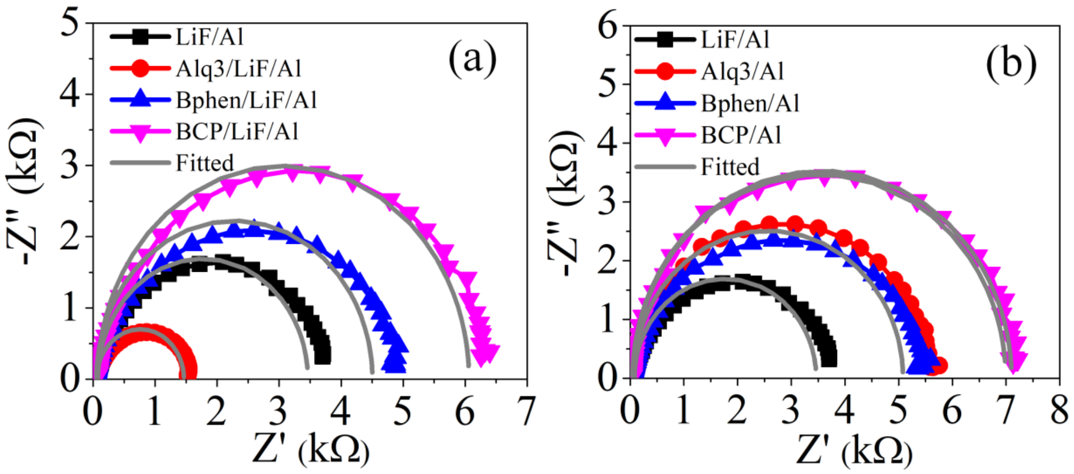

Figure 3.8. Nyquist plots of (a) rrP3HT:PC$_{61}$BM and (b) rrP3HT:PC$_{71}$BM solar cell with different dual cathode buffer layer.

For the device configuration (ii) (shown in Figure 3.9 (ii)), we used Alq3 as additional electron injection layer to provide better Ohmic contact, to enhance the PCE. However, due to the interaction between HOMO level of Alq3 of the dual buffer layer cathode contact with the blend polymer some charge carriers recombine as a result of which we obtained η=1.4% with J_{sc}=7.2 mA/cm^2, V_{oc}=0.56 V and FF= 39% for rrP3HT:PC$_{61}$BM solar cell. On the contrary for rrP3HT:PC$_{71}$BM we obtained η= 3.82% with J_{sc}=11.4 mA/cm^2, V_{oc}=0.56 V and FF= 49%. For the configuration (iii) and (iv), we introduced BPhen and BCP as additional hole blocking layer along with LiF/Al cathode contact respectively. In both the cases, we observed better photovoltaic performance because of lesser charge carrier recombination due to this additional layer with LiF/Al that likely helps to drive the majority carriers towards their respective electrode through built-in voltage which further enhances charge carrier transport. The configuration (iii) (shown in Figure 3.9 (iii)), showed better PCE of η= 3.8% with J_{sc}=11.9 mA/cm², V_{oc}=0.59 V and FF=55% for rrP3HT:PC$_{61}$BM, whereas for rrP3HT:PC$_{71}$BM the PCE obtained was η=4.45%, J_{sc}=12.8 mA/cm², V_{oc}=0.58 V and FF= 60%. BCP, a high band gap material, used here as an additional hole blocking cathode buffer layer, showed the best results among all the device configurations due to its excellent band alignment with both rrP3HT:PC$_{61}$BM and rrP3HT:PC$_{71}$BM active layers and high selectivity towards electron and blocking the holes to minimize the charge recombination between the blend polymer-cathode contact. This led to the improvement in the current density and overall photovoltaic performance. The corresponding energy level diagrams of the devices having configuration BCP/LiF/Al with rrP3HT:PC$_{61}$BM and rrP3HT:PC$_{71}$BM are shown in Figure 3.9. The configuration (iv) showed higher PCE of η= 4.5%, J_{sc}=13.3 mA/cm², V_{oc}=0.59 V and FF= 59% for rrP3HT:PC$_{61}$BM whereas for rrP3HT:PC$_{71}$BM the PCE was η= 4.96%, J_{sc}=13.5 mA/cm², V_{oc}=0.60 V and FF= 61% which is the highest PCE value for BHJ device with dual cathode buffer layer possessing BCP. The photovoltaic performance parameters of all the devices are summarized in Table 3.1.

Table 3.1. Summary of rrP3HT:PC$_{61}$BM and rrP3HT:PC$_{71}$BM devices with different dual cathode buffer layer.

Blend polymer	**Device configuration with ITO/PEDOT:PSS / Blend polymer/**	**R_s (Ω.cm^{-2}) [From Nyquist plots]**	**R_{sh} (Ω.cm^{-2}) [From Nyquist plots]**	**J_{sc} (mA.cm^{-2})**	**V_{oc} (V)**	**FF (%)**	**PCE,η (%)**
rrP3HT:PC$_{61}$BM	(i) LiF/Al	79.67	3483	7.8	0.57	54	2.4
	(ii) Alq3/LiF/Al	61.04	1403	7.2	0.56	39	1.4
	(iii) BPhen/LiF/Al	54.73	4450	11.9	0.59	55	3.8
	(iv) BCP/LiF/Al	74.58	7056	13.3	0.59	59	4.5
rrP3HT:PC$_{71}$BM	(i) LiF/Al	50.96	6735	11.9	0.57	60	4.04
	(ii) Alq3/LiF/Al	53.96	5709	11.4	0.56	59	3.82
	(iii) BPhen/LiF/Al	48.58	6867	12.8	0.58	60	4.45
	(iv) BCP/LiF/Al	51.39	7327	13.5	0.60	61	4.96

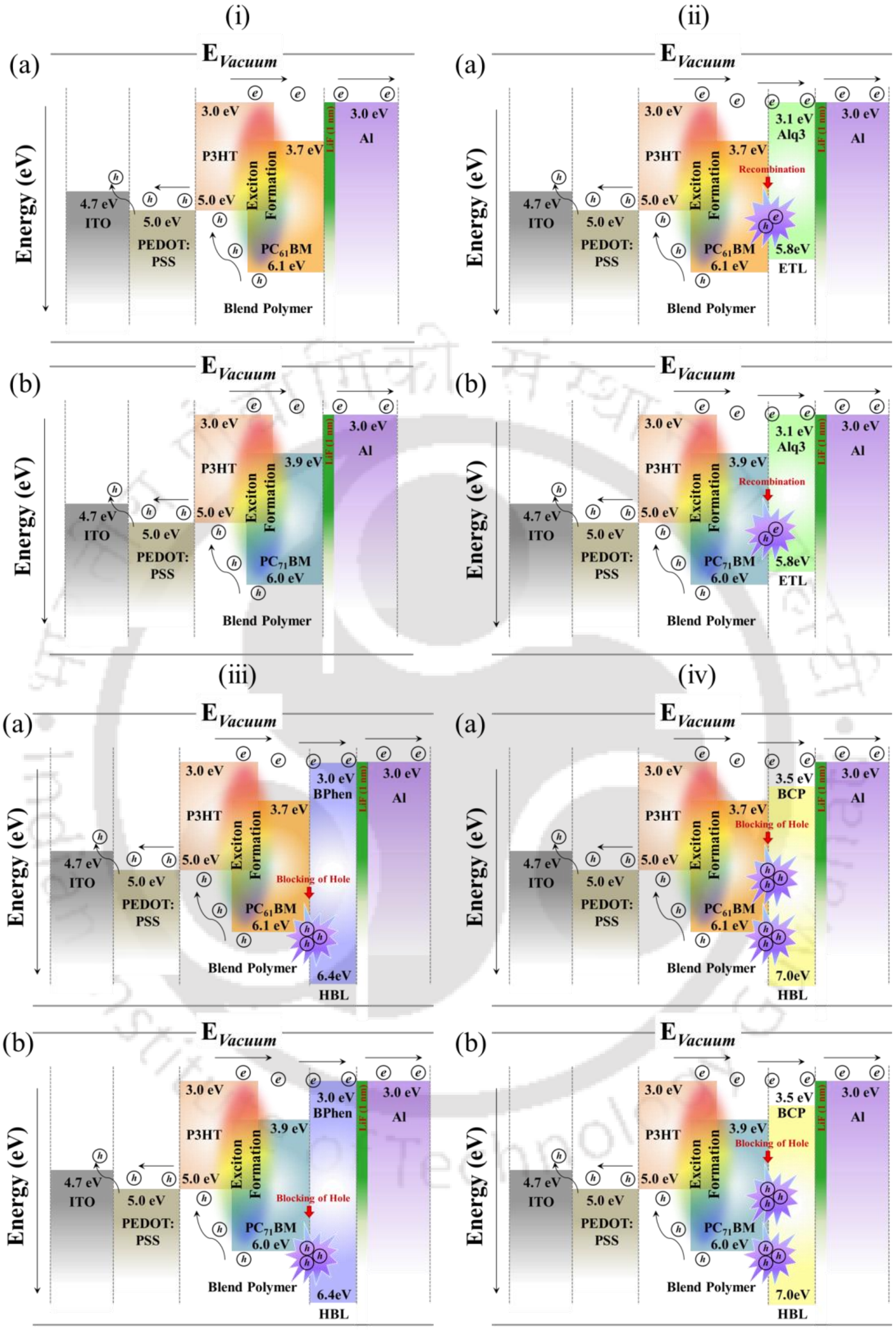

Figure 3.9. Band energy diagram of the fabricated devices having configuration (i), (ii), (iii) and (iv) with blend polymer (a) rrP3HT:PC$_{61}$BM and (b) rrP3HT:PC$_{71}$BM respectively.

3.3 Conclusion

In this Chapter, the significant effect of incorporating different dual cathode buffer layers on the performance of photovoltaic properties of rrP3HT:$PC_{61}BM$ and rrP3HT:$PC_{71}BM$ based bulk heterojunction solar cell was demonstrated. The results of these BHJ devices indicated that the presence of Alq3 acts as an additional electron injecting buffer layer, with LiF/Al cathode, thereby lowering the PCE due to the charge carrier recombination. The BCP and BPhen, act as additional hole blocking buffer layers with LiF/Al showing enhancement in the device performance due to their good band alignment with the active layer. These buffer layers having larger band gap than that of blend polymer helps them to prevent the charge carrier recombination at the cathode electrode. Specifically, BCP with LiF/Al showed the best performance compared to other devices, with η= 4.5%, J_{sc}=13.3 mA/cm^2, V_{oc}=0.59 V and FF= 59% and PCE, η= 4.96%, J_{sc}=13.5 mA/cm^2, V_{oc}=0.60 V and FF= 61% for rrP3HT:$PC_{61}BM$ and rrP3HT:$PC_{71}BM$ respectively, due to its better hole-blocking capacity. In this study we could successfully demonstrate the vital role of dual cathode buffer layers for enhancing the power convention efficiency of rrP3HT:PCBM based organic bulk heterojunction solar cells.

3.4 References

1. Ma, W. L.; Yang, C. Y.; Gong, X.; Lee, K.; Heeger, A. J. Thermally Stable, Efficient Polymer Solar Cells with Nanoscale Control of the Interpenetrating Network Morphology. *Adv. Funct. Mater.* **2005**, *15*, 1617–1622.

2. Li, G.; Shrotriya, V.; Huang, J. S.; Yao, Y.; Moriarty, T.; Emery, K.; Yang, Y. High-Efficiency Solution Processable Polymer Photovoltaic Cells by Self-Organization of Polymer Blends. *Nat. Mater.* **2005**, *4*, 864–868.

3. Dennler, G.; Scharber, M. C.; Brabec, C. J. Polymer-Fullerene Bulk-Heterojunction Solar Cells. *Adv. Mater.* **2009**, *21*, 1323–1338.

4. Li, G.; Zhu, R.; Yang, Y. Polymer Solar Cells. *Nature Photon.* **2012**, *6* (3), 153–161.

5. Deibel, C.; Dyakonov, V. Polymer-Fullerene Bulk Heterojunction Solar Cells. *Rep. Prog. Phys.* **2010**, *73,* 096401.

6. Nelson, J. Polymer: Fullerene Bulk Heterojunction Solar Cells. *Mater. Today* **2011**, *14*, 462–470.

7. Jørgensen, M.; Norrman, K.; Gevorgyan, S. A.; Tromholt, T.; Andreasen, B.; Krebs, F. C. Stability of Polymer Solar Cells. *Adv. Mater.* **2012**, *24*, 580–612.

8. Grossiord, N.; Kroon, J. M.; Andriessen, R.; Blom, P. W. M. Degradation Mechanisms in Organic Photovoltaic Devices. *Org. Electron.* **2012**, *13*, 432–456.

9. Wong, W.-Y.; Wang, X.-Z.; He, Z.; Djurisic, A. B.; Yip, C.-T.; Cheung, K.-Y.; Wang, H.; Mak, C. S. K.; Chan, W.-K. Metallated Conjugated Polymers as a New Avenue towards High-Efficiency Polymer Solar Cells. *Nat. Mater.* **2007**, *6*, 521–527.

10. Pandey, R.; Holmes, R. J. Graded Donor-Acceptor Heterojunctions for Efficient Organic Photovoltaic Cells. *Adv. Mater.* **2010**, *22*, 5301–5305.

11. Hoven, C. V.; Dang, X.-D.; Coffin, R. C.; Peet, J.; Nguyen, T.-Q.; Bazan, G. C. Improved Performance of Polymer Bulk Heterojunction Solar Cells through the Reduction of Phase Separation via Solvent Additives. *Adv. Energy Mater.* **2010**, *22,* E63–E66.

12. Brabec, C. J.; Shaheen, S. E.; Winder, C.; Sariciftci, N. S.; Denk, P. Effect of LiF/Metal Electrodes on the Performance of Plastic Solar Cells. *Appl. Phys. Lett.* **2002**, *80*, 1288–1290.

13. Hill, I. G.; Rajagopal, A.; Kahn, A.; Hu, Y. Molecular Level Alignment at Organic Semiconductor-Metal Interfaces. *Appl. Phys. Lett.* **1998**, *73*, 662–664.

14. Li, H. R.; Zhang, F. J.; Wang, Y. Y.; Zheng, D. S. Synthesis and Characterization of Tris-(8-Hydroxyquinoline)Aluminum. *Mat. Sci. Eng. B-Solid* **2003**, *100*, 40–46.

15. Shrotriya, V.; Ouyang, J.; Tseng, R. J.; Li, G.; Yang, Y. Absorption Spectra Modification in Poly(3-Hexylthiophene): Methanofullerene Blend Thin Films. *Chem. Phys. Lett.* **2005**, *411*, 138–143.

16. Lai, T.-H.; Tsang, S.-W.; Manders, J. R.; Chen, S.; So, F. Properties of Interlayer for Organic Photovoltaics. *Mater. Today* **2013**, *16*, 424–432.

17. Erb, T.; Zhokhavets, U.; Gobsch, G.; Raleva, S.; Stühn, B.; Schilinsky, P.; Waldauf, C.; Brabec, C. J. Correlation Between Structural and Optical Properties of Composite Polymer/Fullerene Films for Organic Solar Cells. *Adv. Funct. Mater.* **2005**, *15*, 1193–1196.

18. Leever, B. J.; Bailey, C. A.; Marks, T. J.; Hersam, M. C.; Durstock, M. F. In Situ Characterization of Lifetime and Morphology in Operating Bulk Heterojunction Organic Photovoltaic Devices by Impedance Spectroscopy. *Adv. Energy Mater.* **2012**, *2*, 120–128.

19. Perrier, G.; de Bettignies, R.; Berson, S.; Lemaître, N.; Guillerez, S. Impedance Spectrometry of Optimized Standard and Inverted P3HT-PCBM Organic Solar Cells. *Sol. Energ. Mat. Sol. Cells* **2012**, *101*, 210–216.

20. Garcia-Belmonte, G.; Munar, A.; Barea, E. M.; Bisquert, J.; Ugarte, I.; Pacios, R. Charge Carrier Mobility and Lifetime of Organic Bulk Heterojunctions Analyzed by Impedance Spectroscopy. *Org. Electron.* **2008**, *9*, 847–851.

21. Chi, D.; Qu, S. C.; Wang, Z. G.; Wang, J. Z. High Efficiency P3HT:PCBM Solar Cells with an Inserted PCBM Layer. *J. Mater. Chem. C* **2014**, *2*, 4383–4387.

22. Park, S. H.; Roy, A.; Beaupré, S.; Cho, S.; Coates, N.; Moon, J. S.; Moses, D.; Leclerc, M.; Lee, K.; Heeger, A. J. Bulk Heterojunction Solar Cells with Internal Quantum Efficiency Approaching 100%. *Nature Photon.* **2009**, *3*, 297–303.

23. Lee, J. H.; Cho, S.; Roy, A.; Jung, H.-T.; Heeger, A. J. Enhanced Diode Characteristics of Organic Solar Cells using Titanium Suboxide Electron Transport Layer. *Appl. Phys. Lett.* **2010**, *96,* 163303.

24. Li, G.; Chu, C.-W.; Shrotriya, V.; Huang, J.; Yang, Y. Efficient Inverted Polymer Solar Cells. *Appl. Phys. Lett.* **2006**, *88,* 253503.

25. Zhao, D. W.; Liu, P.; Sun, X. W.; Tan, S. T.; Ke, L.; Kyaw, A. K. K. An Inverted Organic Solar Cell with an Ultrathin Ca Electron-Transporting Layer and MoO_3 Hole-Transporting Layer. *Appl. Phys. Lett.* **2009**, *95,* 153304.

26. White, M. S.; Olson, D. C.; Shaheen, S. E.; Kopidakis, N.; Ginley, D. S. Inverted Bulk-Heterojunction Organic Photovoltaic Device using a Solution-Derived ZnO Underlayer. *Appl. Phys. Lett.* **2006**, *89,* 143517.

27. Kyaw, A. K. K.; Wang, D. H.; Gupta, V.; Leong, W. L.; Ke, L.; Bazan, G. C.; Heeger, A. J. Intensity Dependence of Current-Voltage Characteristics and Recombination in High-Efficiency Solution-Processed Small-Molecule Solar Cells. *ACS Nano* **2013**, *7,* 4569–4577.

28. Wang, D. H.; Kyaw, A. K. K.; Gupta, V.; Bazan, G. C.; Heeger, A. J. Enhanced Efficiency Parameters of Solution-Processable Small-Molecule Solar Cells Depending on ITO Sheet Resistance. *Adv. Energy Mater.* **2013**, *3,* 1161–1165.

29. Yang, X. N.; Loos, J.; Veenstra, S. C.; Verhees, W. J. H.; Wienk, M. M.; Kroon, J. M.; Michels, M. A. J.; Janssen, R. A. J. Nanoscale Morphology of High-Performance Polymer Solar Cells. *Nano Lett.* **2005**, *5*, 579–583.

30. Wang, T.; Chen, C.; Guo, K.; Chen, G.; Xu, T.; Wei, B. Improved Performance of Polymer Solar Cells by using Inorganic, Organic, and Doped Cathode Buffer Layers. *Chin. Phys. B* **2016**, *25,* 038402.

31. Oh, I. S.; Ji, C. H.; Oh, S. Y. Effects of Ytterbium on Electrical and Optical Properties of BCP/Ag/WO_3 Transparent Electrode based Organic Photovoltaic Cells. *Electron. Mater. Lett.* **2016**, *12*, 156–162.

32. Kim, J.-H.; Park, J.-G. Effect of a Co-Evaporated Alq(3):Liq Cathode Buffer Layer on the Performance of a Polymer Photovoltaic Cell. *J. Korean. Phys. Soc.* **2015**, *66*, 1872–1878.

33. Chang, C.-C.; Lin, C.-F.; Chiou, J.-M.; Ho, T.-H.; Tai, Y.; Lee, J.-H.; Chen, Y.-F.; Wang, J.-K.; Chen, L.-C.; Chen, K.-H. Effects of Cathode Buffer Layers on the Efficiency of Bulk-Heterojunction Solar Cells. *Appl. Phys. Lett.* **2010**, *96,* 263506.

34. Cheng, Y.-J.; Cao, F.-Y.; Lin, W.-C.; Chen, C.-H.; Hsieh, C.-H. Self-Assembled and Cross-Linked Fullerene Interlayer on Titanium Oxide for Highly Efficient Inverted Polymer Solar Cells. *Chem. Mater.* **2011**, *23,* 1512–1518.

35. Xiao, T.; Fungura, F.; Cai, M.; Anderegg, J. W.; Shinar, J.; Shinar, R. Improved Efficiency and Stability of Inverted Polymer Solar Cells with a Solution-Processed BPhen Interlayer and Polystyrene Beads. *Org. Electron.* **2013**, *14*, 2555–2563.

36. Jung, G. H.; Lee, J.-L. Origin of Gap States in the Electron Transport Layer of Organic Solar Cells. *J. Mater. Chem. A* **2013**, *1*, 3034–3039.

37. Roy, A.; Park, S. H.; Cowan, S.; Tong, M. H.; Cho, S. N.; Lee, K.; Heeger, A. J. Titanium Suboxide as an Optical Spacer in Polymer Solar Cells. *Appl. Phys. Lett.* **2009**, *95,* 013302.

38. Hau, S. K.; Yip, H.-L.; Baek, N. S.; Zou, J. Y.; O'Malley, K.; Jen, A. K.-Y. Air-Stable Inverted Flexible Polymer Solar Cells using Zinc Oxide Nanoparticles as an Electron Selective Layer. *Appl. Phys. Lett.* **2008**, *92,* 253301.

39. Hau, S. K.; Yip, H.-L.; Ma, H.; Jen, A. K.-Y. High Performance Ambient Processed Inverted Polymer Solar Cells through Interfacial Modification with a Fullerene Self-Assembled Monolayer. *Appl. Phys. Lett.* **2008**, *93,* 233304.

Chapter 4

Combined Influence of Plasmonic Metal Nanoparticle and Dual Cathode Buffer Layer on PCE of Organic BHJ Solar Cell

The development of highly efficient organic bulk heterojunction (BHJ) solar cells has been rapidly increasing in the last few decades due to their considerable fabrication advantage, that is, the potential to achieve mechanically flexible and light weight devices with large area production capability compared to the silicon technology.[1–10] However, there are several important issues such as high power conversion efficiency (PCE), device life time, large area production, etc., that are yet to be improved in the organic device technology to compete with the conventional silicon technology which dominates the market presently.[11–16] The PCE of BHJ solar cells is primarily controlled by two factors, namely (1) the amount of light absorbed by the active blend material, and (2) the collection of dissociated charges at the cathode contact. Several reports have mentioned methods to overcome these factors separately by performing device modifications.[17–27] Due to the low mobility of organic semiconductors and lower lifetime of the photo generated excitons, the thicknesses of the blend polymers are limited to few nanometre scales. As a consequence, the absorption path length also becomes lower. With the increment of blend polymer thickness, most of the dissociated charges recombine in the active layer, whereas a few are collected at the electrodes as a result of which the PCE value decreases.[28–32] In contrast, the cathode buffer layer plays a very significant role in enhancing the PCE of BHJ solar cells by tuning the contact work function, thereby improving the selectivity towards the particular charge carrier.[33–35] The combination of a particular buffer layer with a cathode contact helps in increasing the short circuit current density (Jsc) and open circuit voltage (Voc), by changing the built-in-potential generated by the work function difference of the electrodes. This modified built-in-potential helps in driving the charge carriers towards their respective electrodes and finally as a result of which the PCE value increases.[36,37] However, by combining the two separate effects, namely, the plasmonic effect of metal NPs and the effect of the cathode buffer layer, the PCE of organic BHJ solar cells can be further enhanced.

In this Chapter, freshly synthesized AuNPs and AgNPs were blended with the PEDOT:PSS hole transport layer and their combined effect was carefully analysed with cathode contacts containing different dual buffer layers with rrP3HT:PC61BM and rrP3HT:PC71BM as blend polymer systems. For the dual cathode buffer layer, we chose two different hole blocking layers, BPhen and BCP, with a LiF/Al cathode contact. It has been observed that for both the blend polymer systems the power conversion efficiency (PCE) increases significantly in the presence of the PEDOT:PSS + AuNPs and PEDOT:PSS + AgNPs with BCP/LiF/Al as a cathode contact compared to the bare PEDOT:PSS layer. In particular, in the presence of PEDOT:PSS + AuNPs and BCP/LiF/Al, the highest PCE was observed for both the blend polymers because of the better band alignment of BCP/LiF/Al with the active layers and the superior surface plasmon resonance of the AuNPs in the visible spectrum compared to AgNPs.

4.1 Experiments

4.1.1 Materials

Gold (III) chloride trihydrate ($HAuCl_4 \cdot 3H_2O$) (Mw~393.83 g/mol), Silver nitrate ($AgNO_3$) (Mw~169.87 g/mol), Bathocuproine (BCP) (Mw~360.45 g/mol), Bathophenanthroline (BPhen) (Mw~332.40 g/mol), Lithium fluoride (LiF), Aluminum wire (99.999% purity), Indium tin oxide (ITO) coated glass substrate (R_{Sheet}~15Ω/sq.), Poly(3,4-ethylenedioxythiophene)-poly(styrenesulfonate) (PEDOT:PSS), [6,6]-Phenyl C_{61} butyric acid methyl ester ($PC_{61}BM$) (Mw~910.88 g/mol), were purchased from Sigma Aldrich. Tri-sodium citrate 2-hydrate was obtained from Merck Specialties Pvt. Ltd., India. [6,6]-Phenyl C_{71} butyric acid methyl ester ($PC_{71}BM$) (Mw~1030.93 g/mol, 99.5% pure) was purchased from Luminescence Technology Corp., Taiwan. Regioregular poly(3-hexylthiophene-2,5-diyl) (rrP3HT) (Mw~83 kg/mol) was used as received from Sycon Polymers India Pvt. Ltd.

4.1.2 Characterization Details

The UV-Visible absorption spectra and the Transmission Electron Microscopy (TEM) image of the synthesized metal NPs were characterized by Jaz UV-Vis spectrophotometer and Tecnai G2 F20 S-twin JEOL 2100 transmission electron microscope respectively. Field emission scanning electron microscopy (FESEM) images were recorded in a Sigma Carl Zeiss scanning electron microscope. Grazing-Incidence wide-Angle X-ray Scattering (GIWAXS) and Grazing-Incidence small-Angle X-ray Scattering (GISAXS) were recorded by Xenocs Xeuss 2.0 instrument photon energy of 8.04 keV and a sample–detector distance of 177.33 mm for GIWAXS and 2503.3 mm for GISAXS with a grazing incidence angle of 0.18°. The steady state PL spectra were recorded by Fluromax-4 spectrophotometer. Laurell and Spin 150 spin coaters were used for the deposition of metal NPs doped PEDOT:PSS as well as the blend polymers on ITO coated glass substrate. The thicknesses of the films were measured by Veeco Dektak 150 Surface Profilometer. Agilent 5500-STM instrument was used for the AFM analysis. Newport, Oriel Sol 3A solar simulator and Oriel IQE-200 instrument were used for solar cell J-V characterization and for the measurement of external quantum efficiency (EQE) of all the fabricated BHJ solar cells. Impedance Spectroscopy was recorded by CH 680 Instrument. Finally Keithley-2400 digital source meter was used to measure all the electrical properties of the fabricated devices.

4.1.3 Device Fabrication

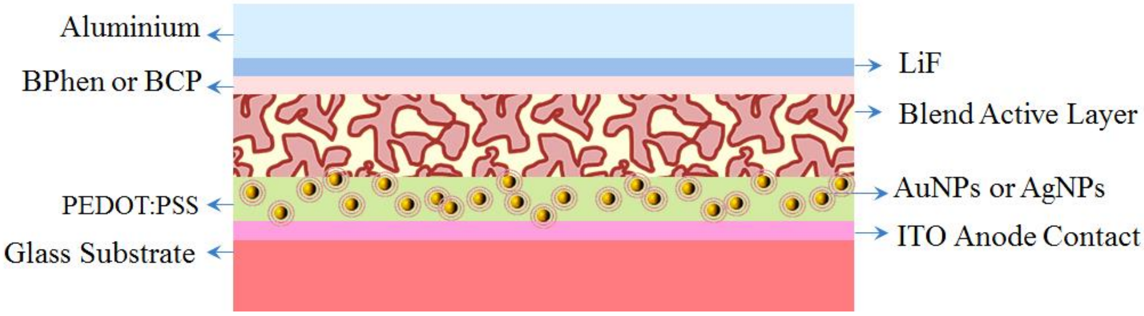

Figure 4.1. Schematic representation of the fabricated rrP3HT:PC$_{61}$BM and rrP3HT:PC$_{71}$BM based plasmonic BHJ organic solar cell.

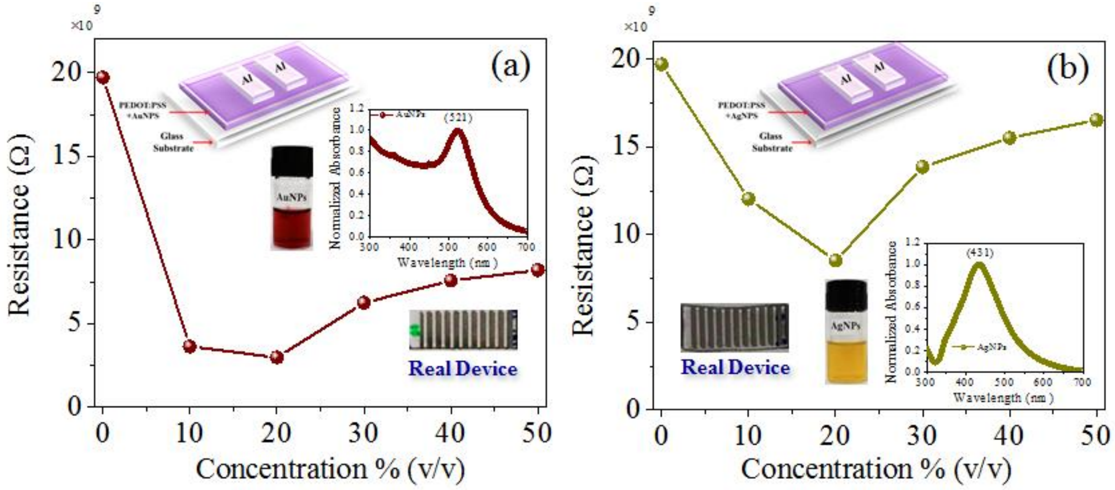

Figure. 4.2. Graphical representation of resistive device of PEDOT:PSS layer at different concentration of (a) AuNPs and (b) AgNPs. Inset of this graph, the schematic of the fabricated resistive device (AL/PEDOT:PSS (with or without metal NPs at different concentration/Al) and UV-Vis Spectra of AuNPs and AgNPs.

A schematic device representation of P3HT:PCBM (blend polymer) based plasmonic solar cell with additional cathode buffer layer is shown in Figure. 4.1. For the fabrication of plasmonic BHJ solar cells, the AuNPs and AgNPs were first synthesized by chemical reduction method. The details of the synthesis technique of the metal NPs and their respective characterizations are given in the result and discussion section. After synthesizing the metal NPs two separate blend solutions were made with the standard hole injecting layers (HIL), PEDOT:PSS, namely PEDOT:PSS + AuNPs and PEDOT:PSS + AgNPs having concentration of 20% (v/v). Before the device fabrication we systematically standardized the concentration of the metal NPs in PEDOT:PSS HIL by measuring resistive device for bare and doped PEDOT:PSS Figure. 4.2. Followed by this, the modified hole injecting layers, were spin coated at 3000 rpm for 60 seconds on the pre-cleaned, UV-ozone treated ITO coated glass substrate and dried at 120 °C for 30 minutes under argon atmosphere to improve the hole collection from the polymer to the ITO. The rest of the device fabrication steps are identical to literature.[38]

4.2 Results and Discussion

4.2.1 Synthesis and Characterization of the Metal NPs

The metal NPs were freshly prepared by chemical reduction method using tri-sodium citrate solution as reducing and stabilizing agent. All the solutions were prepared in double distilled water. For the synthesis of AuNPs, 50 mL 10 mM $HAuCl_4$ was heated to boiling using hot plate with continuous stirring using a controlled magnetic stirrer. This solution was boiled until the temperature reached 100°C followed by the rapid addition of 1.5% tri-sodium citrate to this boiling solution with simultaneous stirring. The color of the solution gradually changed from transparent light yellow to dark black and finally to the characteristic wine red, which indicated the formation of AuNPs.

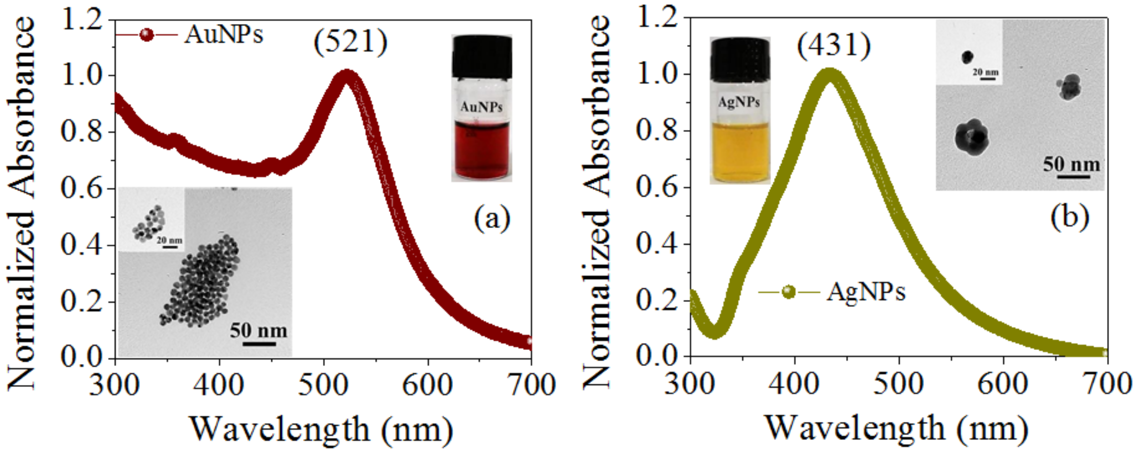

Figure. 4.3. UV-vis absorption spectra (in solution) and TEM image (in inset) of (a) AuNPs and (b) AgNPs

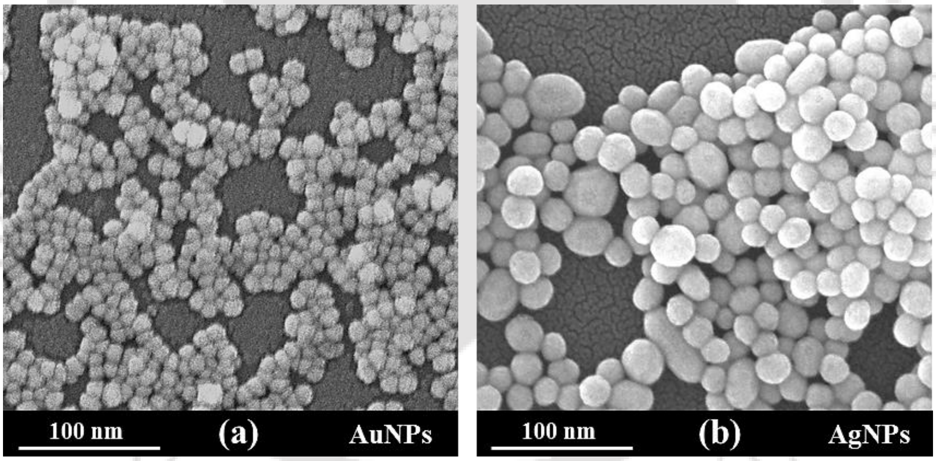

Figure. 4.4. FESEM images of (a) AuNPs and (b) AgNPs respectively

Similarly for the synthesis of AgNPs, 50 mL of 1 mM AgNO3 was heated to boiling using hot plate magnetic stirrer. To this solution 5 mL of 1% tri-sodium citrate was added drop wise. During this process the solution was mixed vigorously and heated until a color change was evident (yellowish brown). Further, it was removed from the heating element and stirred until cool to room temperature. The synthesized metal NPs were characterized by UV-visible spectrophotometer, TEM and FESEM analysis [Figure 4.3 and Figure 4.4]. The characteristic surface plasmon resonance peak of AuNPs and AgNPs were observed at

521 nm and 431 nm whereas the average particle sizes were found to be ~10 nm and ~20 nm respectively.

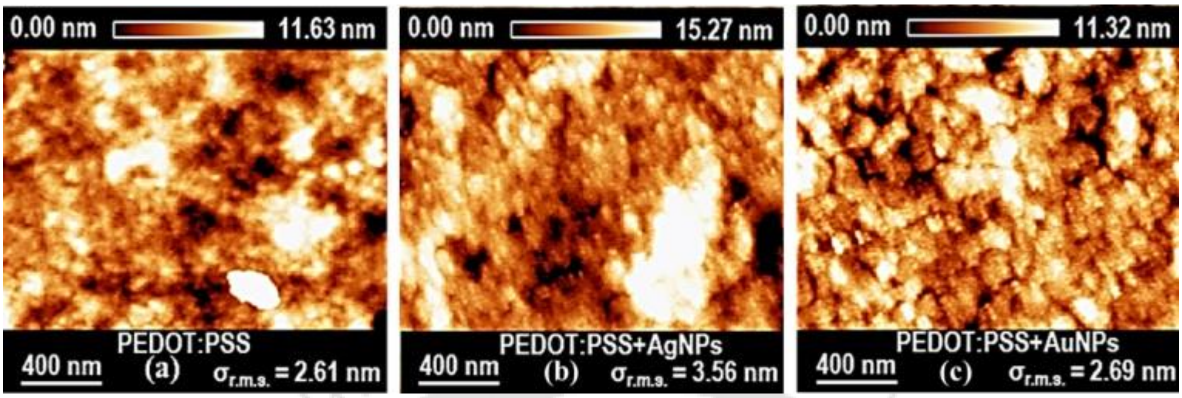

Figure 4.5. AFM topography images (under tapping mode; scan size: 2 μm × 2 μm) of 40 nm thin (a) PEDOT:PSS (b) PEDOT:PSS + AgNPs and (c) PEDOT:PSS + AuNPs deposited on the top ITO coated glass substrate.

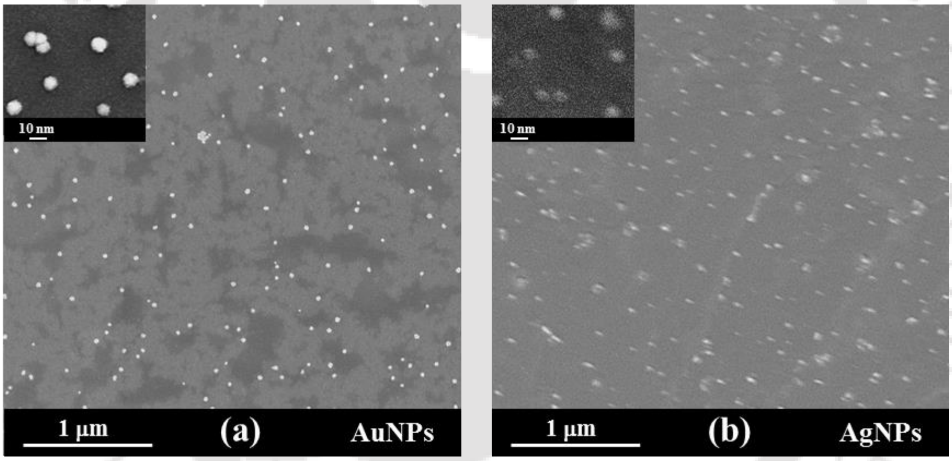

Figure 4.6. FESEM images of PEDOT:PSS doped with 20% (v/v) (a) AuNPs and (b) AgNPs respectively.

It has been observed that the r.m.s. surface roughness of the bare PEDOT:PSS layer was ~2.61 nm whereas for PEDOT:PSS + AuNPs and PEDOT:PSS + AgNPs it was ~2.69 nm and 3.56 nm respectively (Figure. 4.5). The distribution of the metal NPs in the PEDOT:PSS layers are shown in Figure. 4.6. It has been already reported in the literature that, lager size of the metal NPs is always better for enhancing the light scattering and light absorption properties of the BHJ solar cell, which further increase the J_{sc} value of the cell, as a result, one can obtain higher PCE value.[26,27] In this study, it was observed that higher particle size increase the surface roughness (Figure 4.7), as a result, the size of AuNPs and AgNPs was optimized to ~10 nm and ~20 nm respectively.

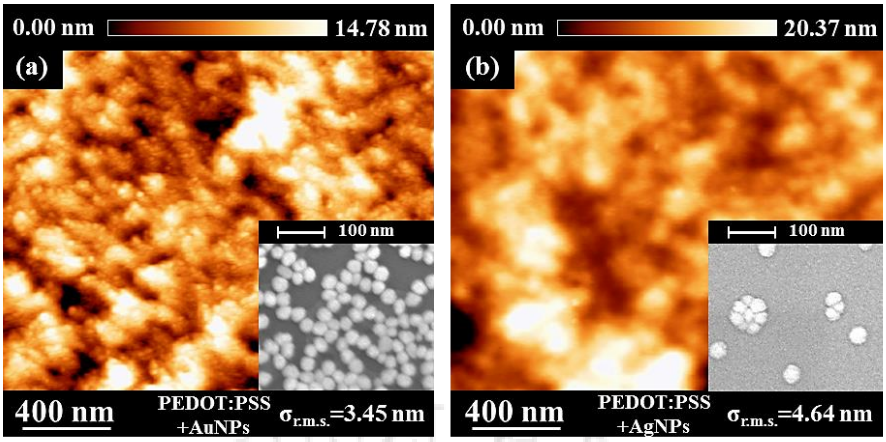

Figure 4.7. AFM topography images (scan size: 2 µm × 2 µm) of 40 nm thin (a) PEDOT:PSS + AuNPs (~40 nm) and (b) PEDOT:PSS + AgNPs (~50 nm) deposited on the top ITO coated glass substrate. The FESEM images of bare and lager in sized AuNPs and AgNPs are shown in the inset of (a) and (b) respectively.

Since sizes of these synthesized NPs are very small compared to the thickness of the PEDOT:PSS thin film (~40 nm) it does not compromise the morphology of the PEDOT:PSS layer. Also as observed from GIWAXS analyses, the crystallinity of the active layers also remains similar in presence of metal nanoparticle doped PEDOT:PSS layer like the bare PEDOT:PSS layer (Figure.4.8). Hence, both these metal NPs can be added to the hole injecting layer to improve the photo absorption and light scattering within the organic BHJ solar cell. From GIWAXS analysis [Figure.4.8a and Figure.4.8b], three major peaks are observed, among which (100) signified almost similar lamellar phase of P3HT, which are 1.64 nm (0.3821 Å^{-1}) and 1.65 nm (0.3818 Å^{-1}) for PC$_{61}$BM and PC$_{71}$BM system on AuNPs doped PEDOT:PSS surface after 30 min exposure time [Figure.4.8c and Figure.4.8e]. Both the films possess the edge on orientation and standard dimension of P3HT. No significant effect in the crystallinity was observed for both the active layers which indicated that there were no crystallinity changes occurring in the active layers due to the incorporation of the metal NPs inside the PEDOT:PSS layer, which is also supported by AFM and electrical performance of the fabricated devices. There is a small difference between the characteristic dimensions obtained from PCBM amorphous peak i.e., 1.364 Å^{-1} (0.46 nm) for PC$_{61}$BM and 1.316 Å^{-1} (0.48 nm) for PC$_{71}$BM which identifies the change in C-chain length in PCBM. The analysis of GIWAXS data was analysed by using the software

GIXSGUI.[38-44]

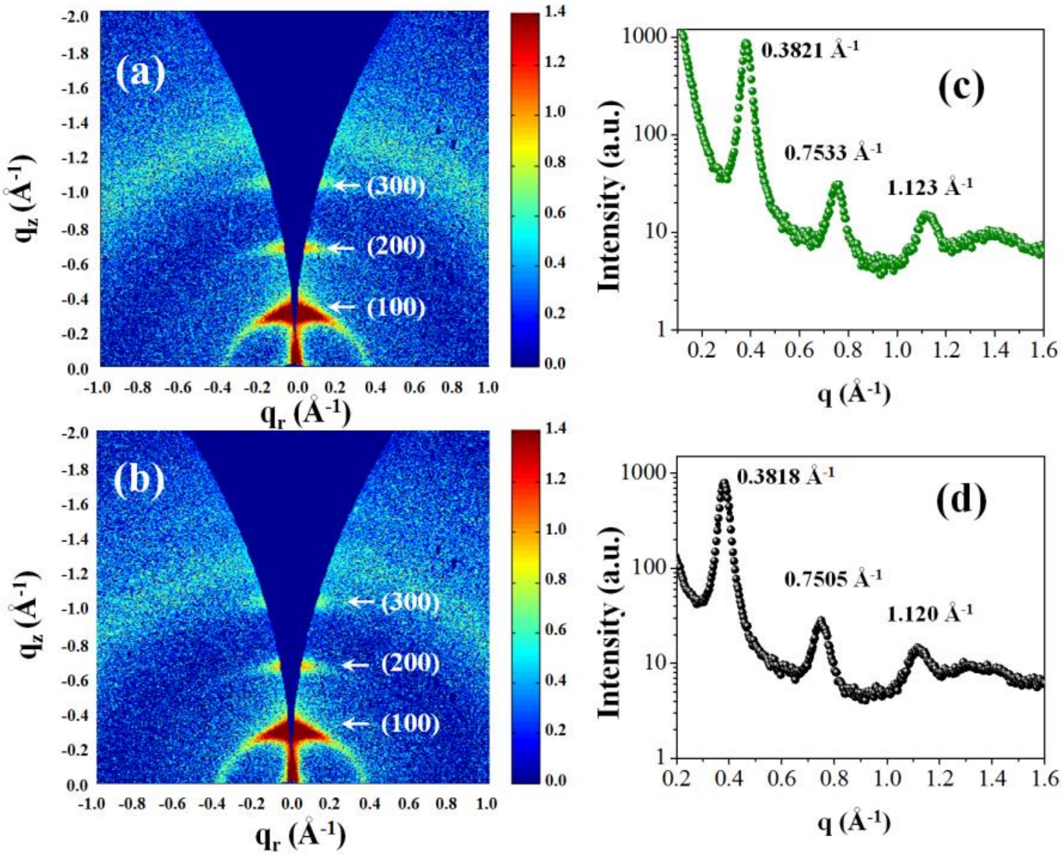

Figure 4.8. GIWAXS images of (a) P3HT:$PC_{61}BM$ and (b) P3HT:$PC_{71}BM$ active layers on PEDOT:PSS + AuNPs coated thin film. The corresponding integrated diffraction intensity plots are shown in (c) and (d) for P3HT:$PC_{61}BM$ and P3HT:$PC_{71}BM$ respectively.

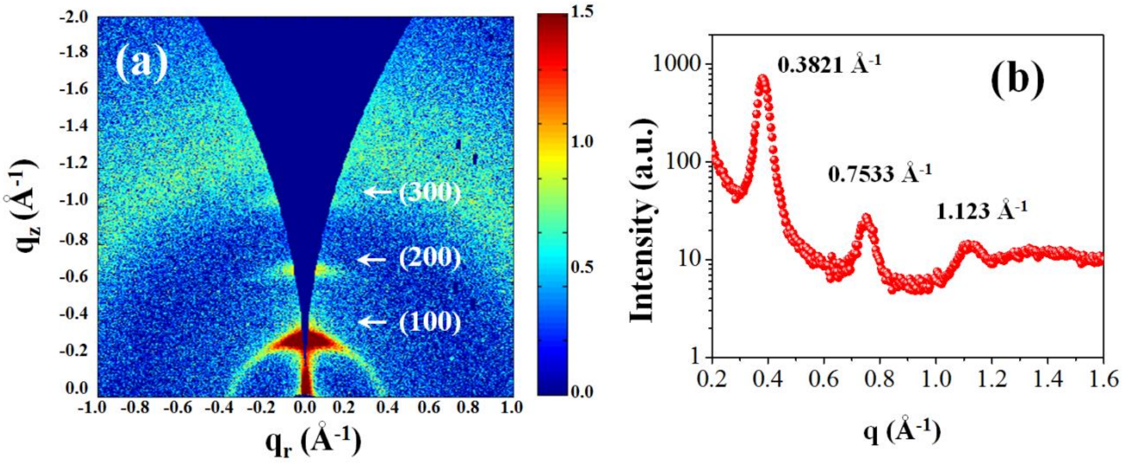

Figure 4.9. (a) GIWAXS images and (b) the corresponding integrated diffraction intensity plot of P3HT:$PC_{71}BM$ active layers on PEDOT:PSS + AgNPs coated thin film.

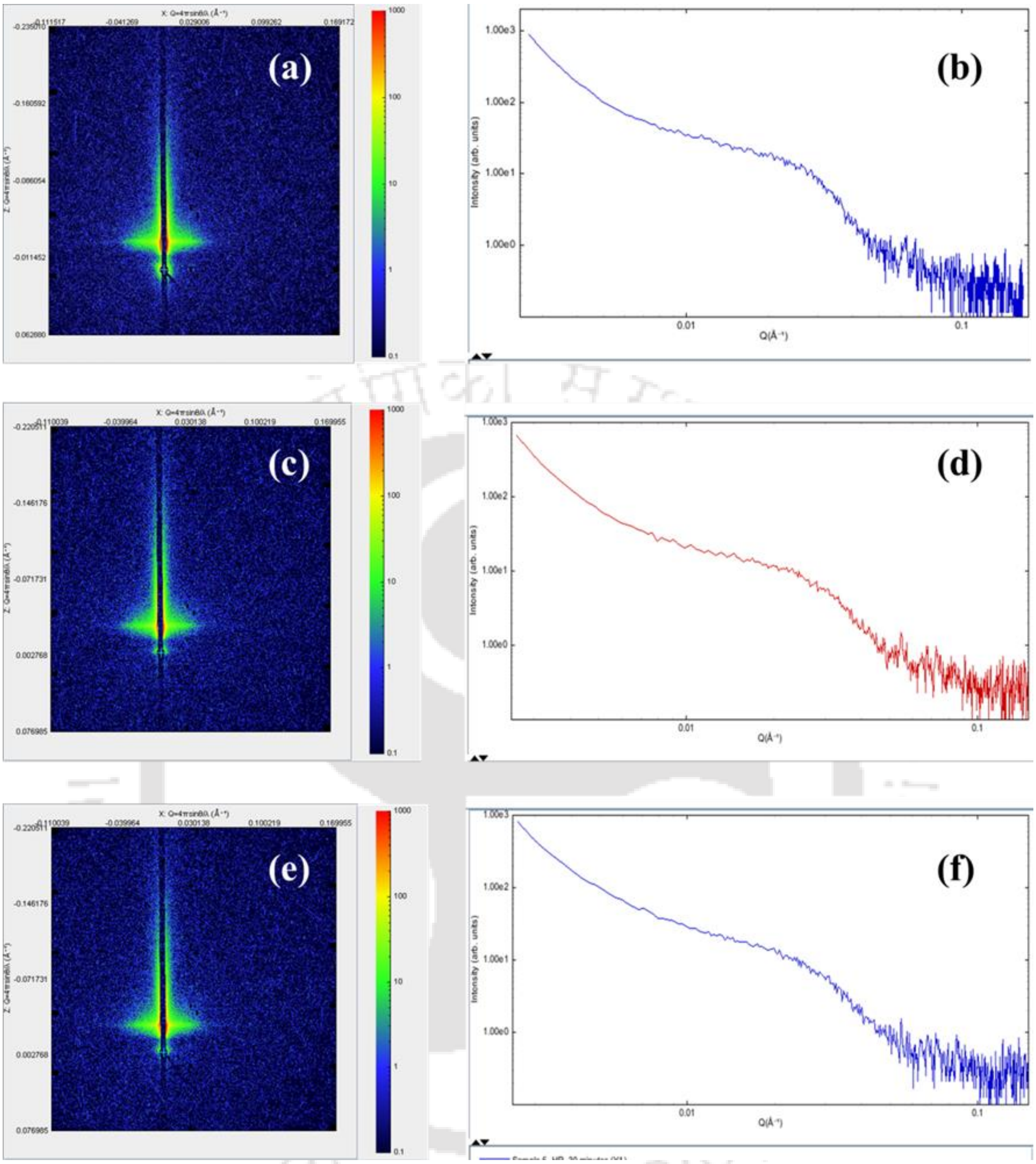

Figure 4.10. GISAXS images of (a) P3HT:PC$_{61}$BM and (b) P3TH:PC$_{71}$BM active layers on PEDOT: PSS + AuNPs coated thin film. The corresponding horizontal cuts from the 2D GISAXS data plots are shown in (b) and (d). GISAXS images and its corresponding horizontal cuts from the 2D GISAXS data of P3TH:PC$_{71}$BM active layers on PEDOT:PSS + AgNPs are shown in (e) and (f) respectively.

For reference purpose, GIWAXS profile of P3HT:PC$_{71}$BM on PEDOT:PSS + AgNPs thin film and AFM images of metal doped PEDOT:PSS layers with both the active blend polymers were also recorded (Figure. 4.9 and Figure. 4.11). The corresponding GISAXS profile of both the blend polymer with metal NPs are also shown in Figure. 4.10.[42] The AFM images of both the active layers on the NPs modified PEDOT:PSS layer recorded post thermal annealing at 150°C for 10 min showed morphology with good phase separation.

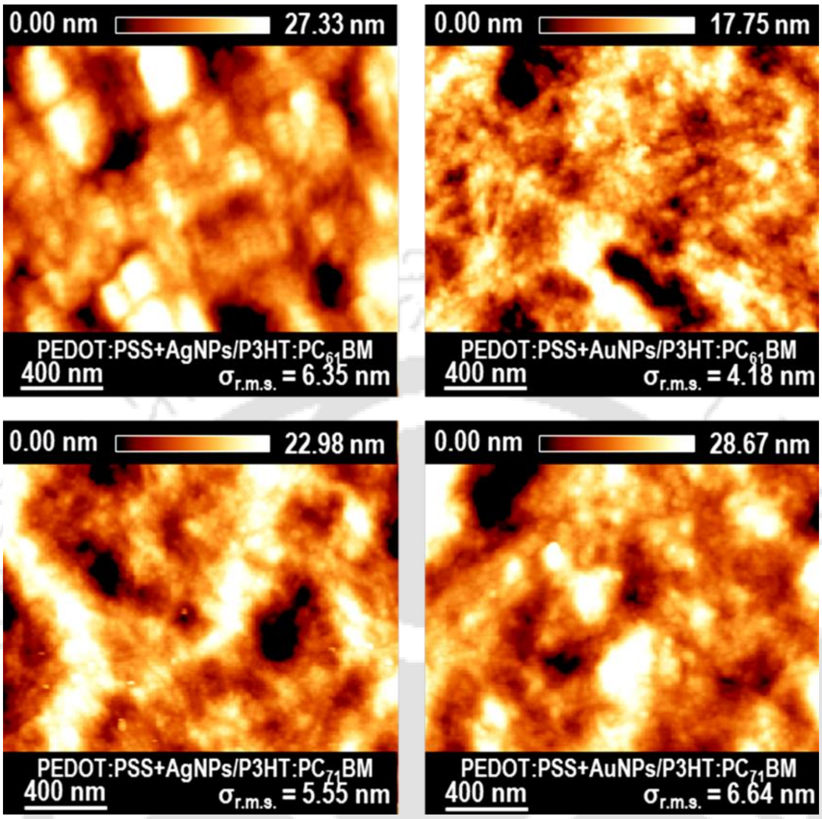

Figure 4.11. AFM topography images (2μm×2μm) of rrP3Ht:PC$_{61}$BM and rrP3HT:PC$_{71}$BM blend polymers on PEDOT:PSS+AgNPs and PEDOT:PSS+AuNPs layers respectively.

4.2.2 Photovoltaic Characterizations

In this work two blend polymer systems namely (i) rrP3HT:PC$_{61}$BM and (ii) rrP3HT:PC$_{71}$BM were used for the fabrication of plasmonic BHJ solar cell. For the fabrication of the devices we used bare PEDOT:PSS as the hole injecting layer and two metal NPs modified hole injecting layers viz. PEDOT:PSS + AgNPs and PEDOT:PSS + AuNPs with two different cathode buffer layers, namely BCP and BPhen. Figure. 4.12 shows the schematic representation of the combined effect of plasmonic metal NPs as well as the dual cathode buffer layer with rrP3HT:PCBM active layer. The UV-Vis spectra and PL spectra of both the blend polymer upon the bare and metal NPs doped PEDOT:PSS are also recorded and are shown in Figure. 4.12 and Figure. 4.13 respectively.

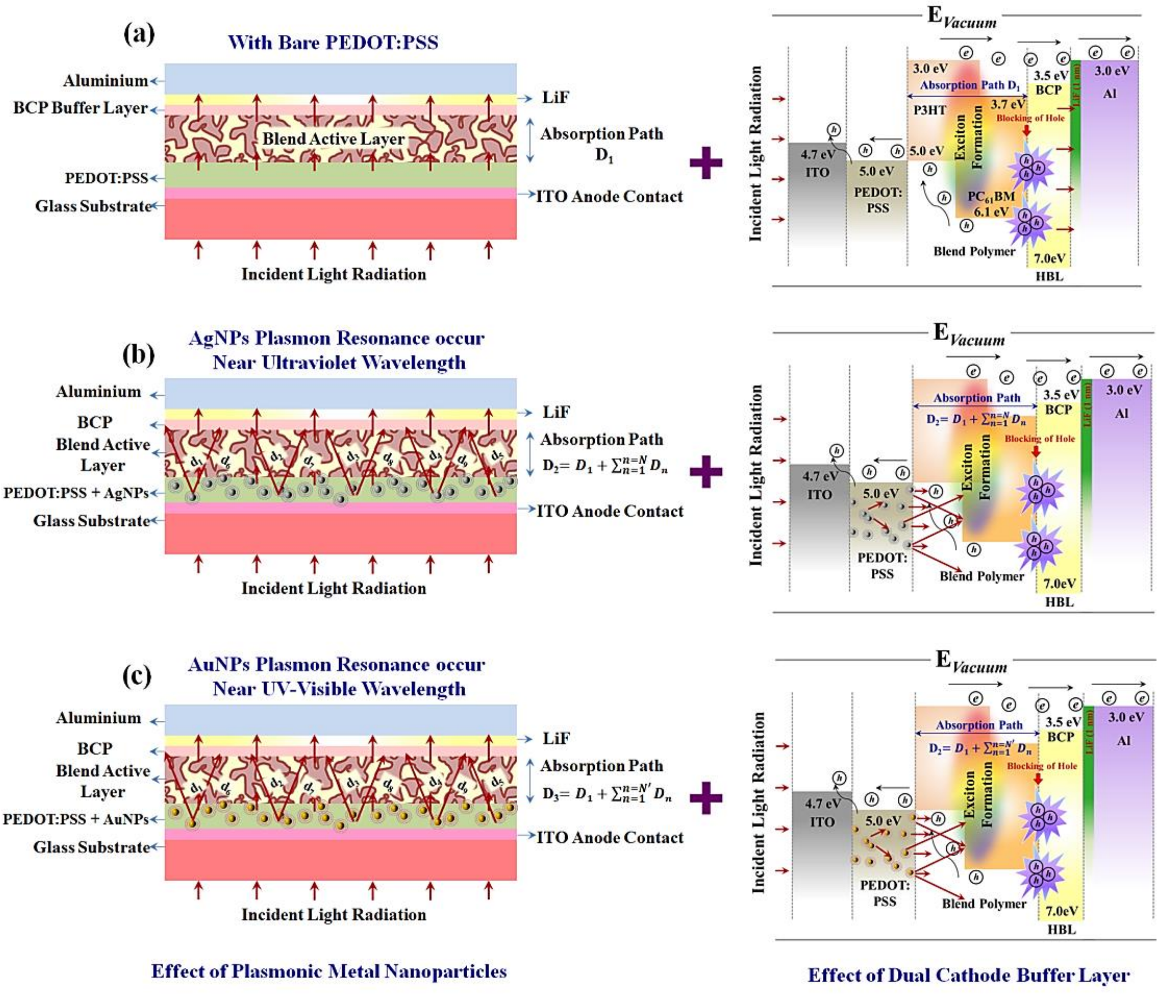

Figure. 4.12. Schematic representation of the combined effect of plasmonic metal NPs and BCP/LiF/Al as the dual cathode buffer layers on rrP3HT:PCBM based bulk heterojunction solar cell with (a) bare PEDOT:PSS, (b) PEDOT:PSS + AgNPs and (c) PEDOT:PSS + AuNPs.

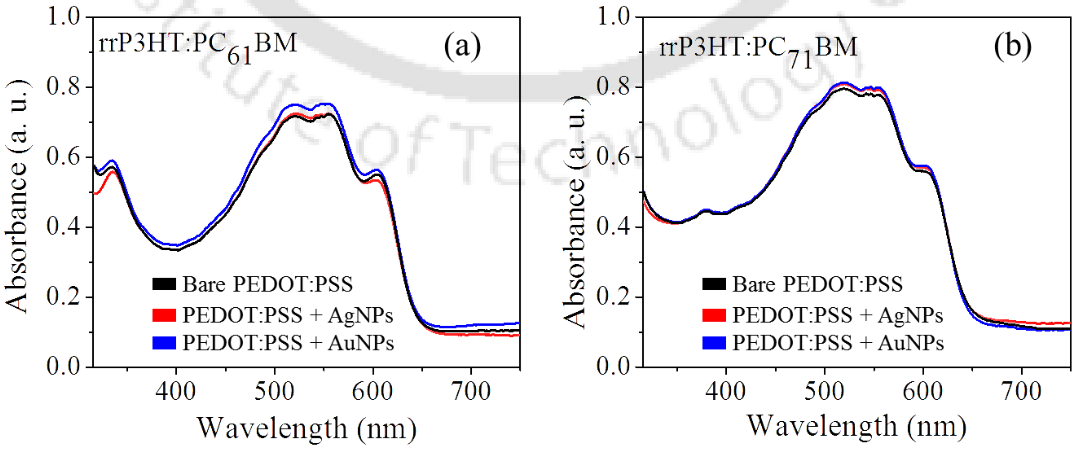

Figure. 4.13. UV-Vis absorption spectra of (a) rrP3HT:PC$_{61}$BM and (b) rrP3HT:PC$_{71}$BM BHJ solar cells in presence of bare PEDOT:PSS, PEDOT:PSS + AgNPs and PEDOT:PSS + AuNPs respectively.

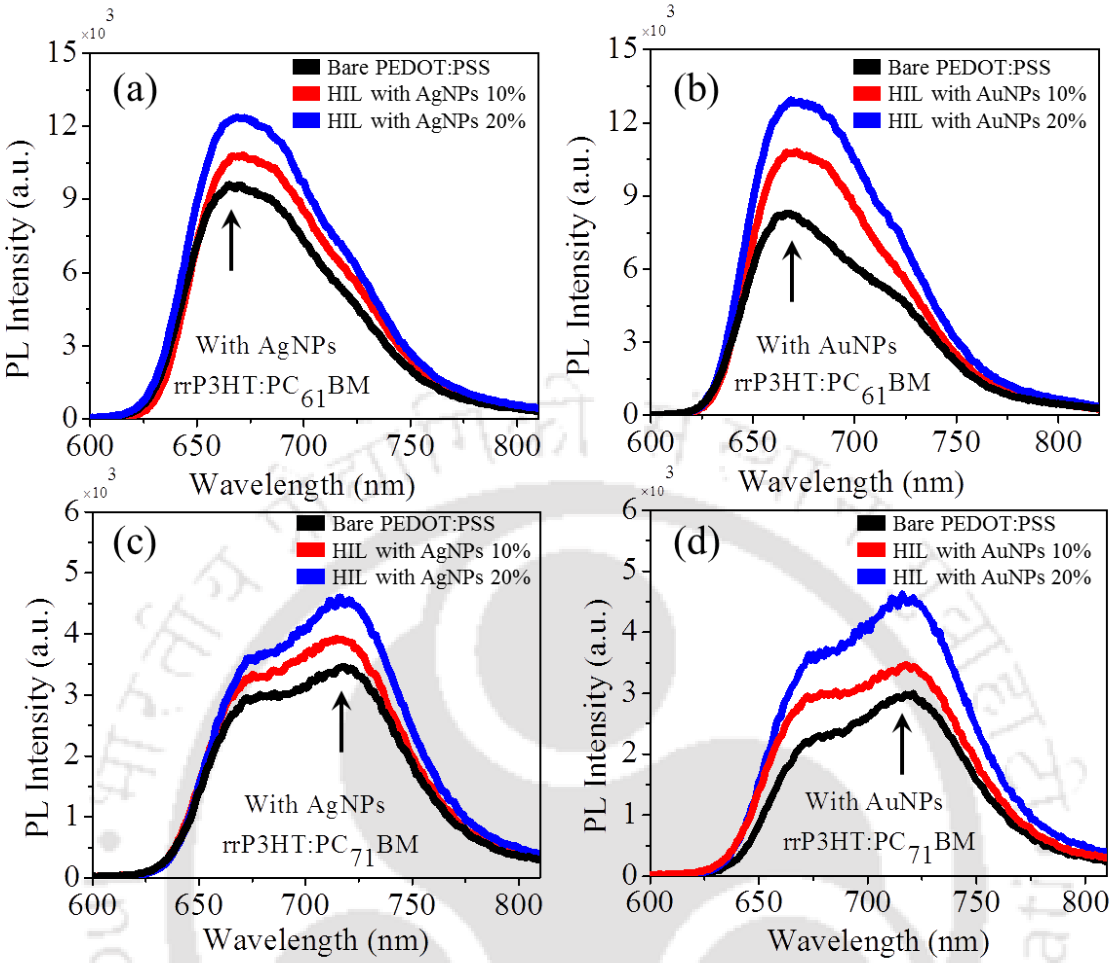

Figure. 4.14. Steady-state photoluminescence (PL) spectra of (a, b) rrP3HT:PC$_{61}$BM and (c, d) rrP3HT:PC$_{71}$BM in presence of different concentration of AgNPs and AuNPs respectively.

Here BCP/LiF/Al is considered as the dual cathode buffer layer since we obtained more efficient results in the case of BCP compared to BPhen. The schematic representation of the same with BPhen/LiF/Al as the dual cathode buffer layer with rrP3HT:PCBM active layer is shown in Figure. 4.15. The mechanism of both the buffer layers along with the metal nanoparticles is almost same. Though the band alignment of BCP and BPhen with rrP3HT:PCBM active layers are different and the morphological growth nature of these two cathode buffer layers upon rrP3HT:PCBM active layer, is created the main difference among them which also affect their BHJ solar cell output performance. For better understanding, the AFM images of BCP and BPhen over rrP3HT:PC$_{61}$BM and rrP3HT:PC$_{71}$BM are shown in Figure. 4.16. It has been observed that among these two additional cathode buffer layers, rrP3HT:PCBM/BPhen [Figure. 4.16a and Figure. 4.16c] showed larger grains and higher surface roughness ($\sigma_{r.m.s.}$ = 11.74 nm and 14.88 nm) compared to BCP. It has already been mentioned in several reports that, in case of organic

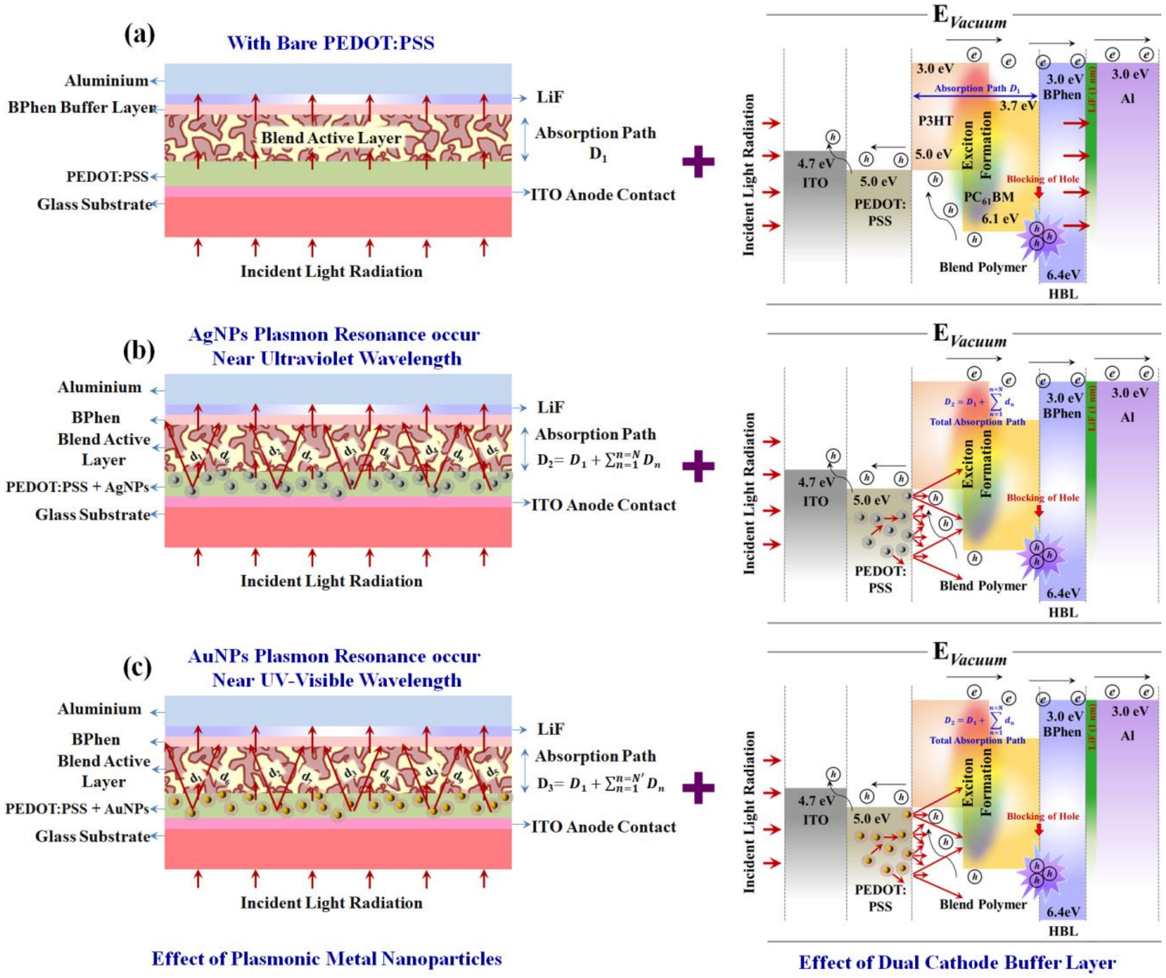

Figure. 4.15. Schematic representation of the combined effect of plasmonic metal NPs and BPhen/LiF/Al as the dual cathode buffer layers on rrP3HT:PCBM based bulk heterojunction solar cell with (a) bare PEDOT:PSS, (b) PEDOT:PSS + AgNPs and (c) PEDOT:PSS + AuNPs.

BHJ solar cells, high surface roughness of cathode buffer layer resists the charge transport from photoactive layer to the cathode contact. This is one of the vital reason due to which the BCP/LiF/Al dual cathode buffer layer shows higher efficient electrical output with both the blend polymer systems compared to BPhen/LiF/Al. Here, the Figure. 4.12a represents the effect of dual cathode buffer layer with bare PEDOT:PSS, whereas Figure 4.12b and Figure 4.12c represents the effect of the same along with PEDOT:PSS + AgNPs and PEDOT:PSS + AuNPs respectively. Each of the device configurations which were fabricated and analysed in the present study are listed in Table 4.1. The devices with bare PEDOT:PSS and dual cathode buffer layers were fabricated for reference purpose as reported previously.[45]

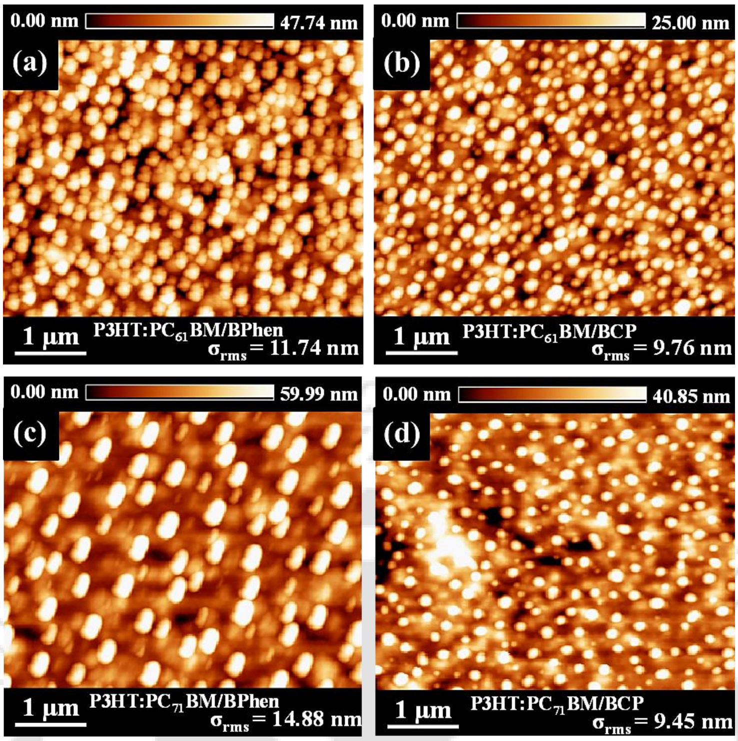

Figure. 4.16. AFM images of (a) BPhen and (b) BCP on rrP3HT:PC$_{61}$BM and (c) BPhen and (d) BCP on rrP3HT:PC$_{71}$BM blend polymer thin film.

Table 4.1 List of the fabricated BHJ device configurations of rrP3HT:PC$_{61}$BM and rrP3HT:PC$_{71}$BM with different dual cathode buffer layer.

Blend Polymer	Hole Injecting Layer (HIL)	Device Configuration with cathode buffer layers
(i) rrP3HT:PC$_{61}$ BM	(a)Bare PEDOT:PSS	(1) ITO / HIL (a) / Blend Polymer (i) / LiF / Al
		(2) ITO / HIL (a) / Blend Polymer (i) / BPhen / LiF / Al
		(3) ITO / HIL (a) / Blend Polymer (i) / BCP / LiF / Al
	(b)PEDOT:PSS +AgNPs	(4) ITO / HIL (b) / Blend Polymer (i) / LiF/Al
		(5) ITO / HIL (b) / Blend Polymer (i) / BPhen / LiF / Al
		(6) ITO / HIL (b) / Blend Polymer (i) / BCP / LiF / Al
	(c)PEDOT:PSS +AuNPs	(7) ITO / HIL (c) / Blend Polymer (i) / LiF / Al
		(8) ITO / HIL (c) / Blend Polymer (i) / BPhen / LiF / Al
		(9) ITO / HIL (c) / Blend Polymer (i) / BCP / LiF / Al
(ii) rrP3HT:PC$_{71}$ BM	(a)Bare PEDOT:PSS	(10) ITO / HIL (a) / Blend Polymer (ii) / LiF / Al
		(11) ITO / HIL (a) / Blend Polymer (ii) / BPhen / LiF / Al
		(12) ITO / HIL (a) / Blend Polymer (ii) / BCP / LiF / Al
	(b)PEDOT:PSS +AgNPs	(13) ITO / HIL (b) / Blend Polymer (ii) / LiF / Al
		(14) ITO / HIL (b) / Blend Polymer (ii) / BPhen / LiF / Al
		(15) ITO / HIL (b) / Blend Polymer (ii) / BCP / LiF / Al
	(c)PEDOT:PSS +AuNPs	(16) ITO / HIL (c) / Blend Polymer (ii) / LiF / Al
		(17) ITO / HIL (c) / Blend Polymer (ii) / BPhen / LiF / Al
		(18) ITO / HIL (c) / Blend Polymer (ii) / BCP / LiF / Al

Herein, we have designed total eighteen different device configurations where the thickness of the HIL (~40 nm) and the blend polymer (~110 nm) layers were kept identical for all the devices. The thickness of the cathode buffer layers, BPhen and BCP were kept at ~6 nm upon which LiF (~1 nm)/Al (~100 nm), conventional cathode contact were deposited.

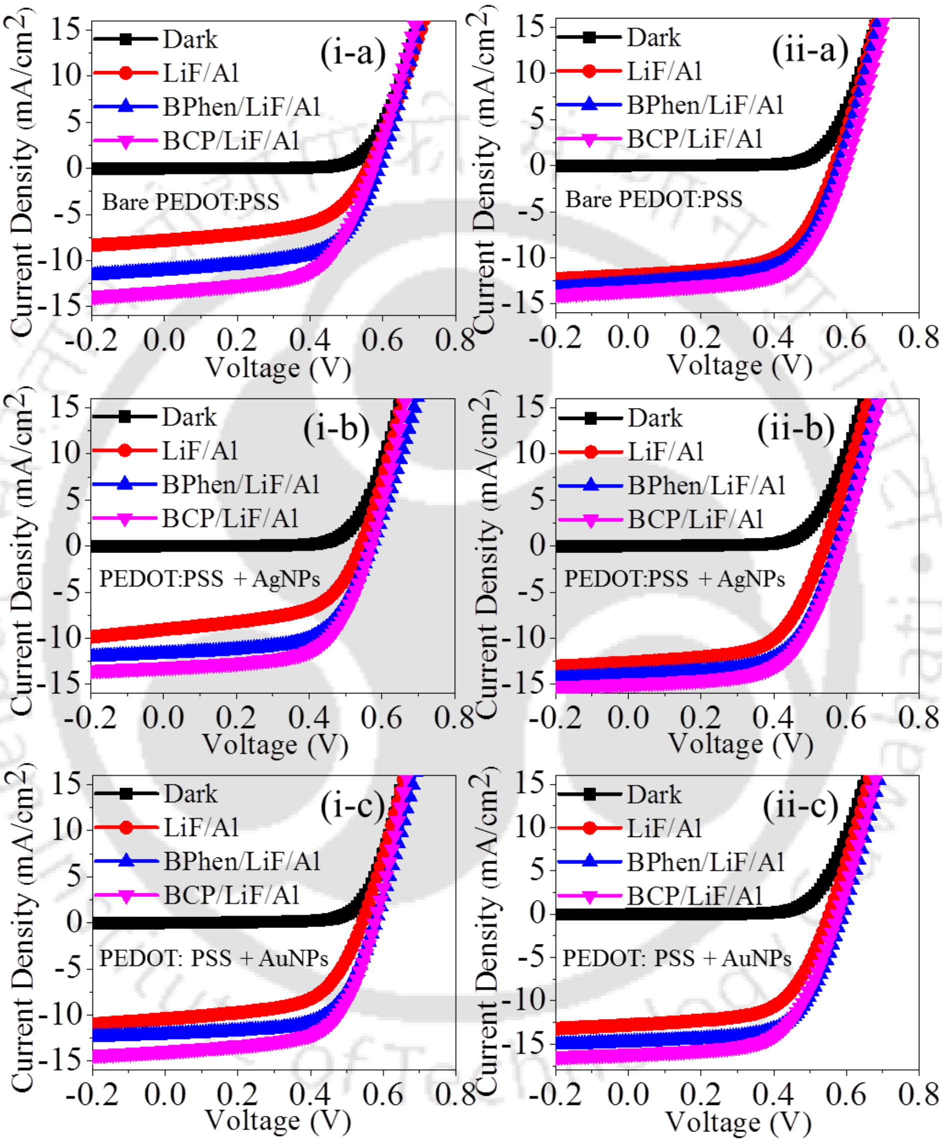

Figure. 4.17. Current density vs. voltage (J-V) characteristics of (i) rrP3HT:PC$_{61}$BM and (ii) rrP3HT:PC$_{71}$BM BHJ solar cells with (a) bare PEDOT:PSS, (b) PEDOT:PSS + AgNPs and (c) PEDOT:PSS + AuNPs with different dual cathode buffer layer.

Figure. 4.17 represent the current density-voltage (J-V) characteristics of all the fabricated devices. From these J-V characteristic graphs, with bare PEDOT:PSS hole injecting layer [Figure. 4.17i-a and Figure. 4. 17ii-a], we observed that by the systematic variation of only the dual cathode buffer layer the PCE (η) value of both the rrP3HT:PC$_{61}$BM and rrP3HT:PC$_{71}$BM BHJ solar cells can be improved. In the devices having configuration (3) we found that the maximum value of η=4.65% with J_{sc}=13.6 mA/cm^2, V_{oc}=0.59 V and FF= 61% for rrP3HT:PC$_{61}$BM blend polymer, whereas, the maximum PCE of the device having configuration (12) fabricated with rrP3HT:PC$_{71}$BM, was observed to be η=4.96% with J_{sc}=13.5 mA/cm^2, V_{oc}=0.59 V and FF= 61%. These highest PCE values obtained in presence of BCP/LiF/Al as compared to the other dual cathode buffer layers are due to the better morphology and excellent band alignment of BCP/LiF/Al with both rrP3HT:PC$_{61}$BM and rrP3HT:PC$_{71}$BM active layers compared to BPhen/LiF/Al and conventional LiF/Al.[45] Also BCP has high selectivity towards electrons due to its high band gap (Eg ~3.5 eV) and deeper HOMO energy level (~ -7 eV) and it can block holes to minimize the charge recombination between the blend polymer-cathode contacts [Figure. 4.12a].

The same phenomenon was also observed when bare PEDOT:PSS was replaced with metal NP incorporated PEDOT:PSS hole injecting layers. Moreover, in the presence of PEDOT:PSS + AgNPs and PEDOT:PSS + AuNPs better device performances were observed compared to the bare PEDOT:PSS because of the surface plasmon effect which increases the photo absorption length, scattering and trapping of the incident light that passes through the HIL [Figure. 4.12b and Figure. 4.12c]. The maximum PCE of the devices, having configuration (6) and (15) fabricated with PEDOT:PSS + AgNPs and BCP/LiF/Al cathode contact, was observed to be η=4.94% with J_{sc}=13.1 mA/cm^2, V_{oc}=0.58 V and FF=62% for rrP3HT:PC$_{61}$BM blend polymer whereas, the maximum PCE of the device having configuration (15) fabricated with rrP3HT:PC$_{71}$BM, was observed to be η=5.29% with J_{sc}=14.7 mA/cm^2, V_{oc}=0.58 V and FF= 61% [Figure. 4.17i-b and Figure. 4.17ii-b]. Further, from the Figure. 4.17i-c and Figure. 4.17ii-c, we observed that the devices having configuration (9) and (18) fabricated with PEDOT:PSS + AuNPs and BCP/LiF/Al cathode contact showed maximum η=4.99% with J_{sc}=13.9 mA/cm^2, V_{oc}=0.59 V and FF=62% for rrP3HT:PC$_{61}$BM blend polymer and maximum η=5.65% with J_{sc}=16.1 mA/cm^2, V_{oc}=0.58 V and FF= 61% for rrP3HT:PC$_{71}$BM blend polymer respectively. In case of the metal NP incorporated PEDOT:PSS hole injecting layers we observed that the device with PEDOT:PSS + AuNPs as the HIL and BCP/LiF/Al as the cathode contact showed better device performance compared to the device containing PEDOT:PSS + AgNPs with the same cathode contact since AuNPs have surface plasmon resonance at the visible spectrum region (~531 nm) whereas AgNPs have the same near the UV region (~421 nm) (Figure. 4.3).[46]

Table 4.2 Summary of plasmonic BHJ solar cell performance with rrP3HT:$PC_{61}BM$ and rrP3HT:$PC_{71}BM$ as the active blend layer and with different dual cathode buffer layer.

Blend polymer	Hole Injecting Layer (HIL)	Device Configuration with ITO/HIL/Blend Polymer/	$J_{sc,max}$ ($^{\#}J_{sc,avg}$) ($mA.cm^{-2}$)	$J_{sc,EQE}$ ($mA.cm^{-2}$)	$V_{oc,max}$($^{\#}V_{oc,avg}$) (V)	FF_{max} (FF_{avg}) (%)	PCE,η_{max} ($^{\#}\eta_{avg}$) (%)
(i) rrP3HT:$PC_{61}BM$	(a)Bare PEDOT:PSS	(1) LiF/Al	10.6 (8.9±1.09)	6.94	0.57 (0.56±0.01)	55 (54±02)	3.30 (2.71±0.32)
		(2) BPhen/LiF/Al	12.4 (11.6±1.31)	8.02	0.59 (0.58±0.01)	60 (58±02)	4.02 (3.69±0.41)
		(3) BCP/LiF/Al	**13.6 (12.7±0.99)**	**8.70**	**0.59 (0.58±0.01)**	**61 (59±02)**	**4.68 (4.44±0.24)**
	(b)PEDOT:PSS +AgNPs	(4) LiF/Al	12.6 (9.9±2.13)	7.43	0.54 (0.53±0.01)	56 (54±02)	3.45 (2.87±0.62)
		(5) BPhen/LiF/Al	12.8 (11.5±1.08)	9.57	0.58 (0.57±0.01)	61 (59±02)	4.18 (3.90±0.29)
		(6) BCP/LiF/Al	**13.1 (12.6±0.72)**	**10.01**	**0.58 (0.56±0.01)**	**62 (58±04)**	**4.94 (4.16±0.56)**
	(c)PEDOT:PSS +AuNPs	(7) LiF/Al	11.6 (10.6±1.07)	8.50	0.55 (0.55±0.01)	59 (58±01)	3.96 (3.39±0.30)
		(8) BPhen/LiF/Al	12.1 (11.2±1.02)	8.94	0.58 (0.57±0.01)	61 (59±02)	4.43 (3.82±0.45)
		(9) BCP/LiF/Al	**13.9 (12.7±1.33)**	**10.04**	**0.59 (0.58±0.01)**	**62 (60±02)**	**4.99 (4.39±0.51)**
(ii) rrP3HT:$PC_{71}BM$	(a)Bare PEDOT:PSS	(10) LiF/Al	12.0 (11.8±1.21)	10.81	0.57 (0.55±0.02)	60 (55±04)	4.04 (3.48±0.67)
		(11) BPhen/LiF/Al	12.8 (11.9±0.99)	11.05	0.58 (0.57±0.01)	60 (55±05)	4.45 (3.79±0.65)
		(12) BCP/LiF/Al	**13.5 (12.8±1.01)**	**11.02**	**0.59 (0.59±0.01)**	**62 (57±05)**	**4.96 (4.36±0.61)**
	(b)PEDOT:PSS +AgNPs	(13) LiF/Al	12.7 (12.6±0.52)	11.01	0.55 (0.54±0.01)	60 (58±02)	4.05 (3.98±0.44)
		(14) BPhen/LiF/Al	14.1 (12.4±1.63)	11.29	0.59 (0.57±0.01)	63 (60±03)	4.92 (4.30±0.47)
		(15) BCP/LiF/Al	**14.7 (13.1±0.93)**	**11.85**	**0.58 (0.57±0.01)**	**61 (59±02)**	**5.29 (4.55±0.48)**
	(c)PEDOT:PSS +AuNPs	(16) LiF/Al	12.8 (11.8±1.36)	10.51	0.55 (0.54±0.01)	61 (58±02)	4.66 (3.81±0.46)
		(17) BPhen/LiF/Al	14.9 (13.1±1.85)	11.61	0.58 (0.57±0.01)	63 (61±02)	5.52 (4.63±0.89)
		(18) BCP/LiF/Al	**16.1 (15.4±1.05)**	**11.92**	**0.58 (0.57±0.01)**	**61 (59±02)**	**5.65 (5.25±0.31)**

$^{\#}$ Average of ten different cells of each of the device configurations are represented in bracket.

Thus, initially with the help of dual cathode buffer layer the PCE of rrP3HT:$PC_{61}BM$ and rrP3HT:$PC_{71}BM$ based BHJ solar cell increased from 3.30% (LiF/Al) to 4.68% (BCP/LiF/Al) and 4.04% (LiF/Al) to 4.96% (BCP/LiF/Al) respectively.

In the second step, using the combined effect of plasmonic AgNPs blended PEDOT:PSS and dual cathode buffer layers the PCE value further increased from 3.45% (LiF/Al) to 4.94% (BCP/LiF/Al) for rrP3HT:$PC_{61}BM$ and from 4.05% (LiF/Al) to 5.29% (BCP/LiF/Al) for rrP3HT:$PC_{71}BM$ active layers. Finally, utilizing the PEDOT:PSS + AuNPs and dual cathode buffer layer combination the maximum PCE value for both the blend polymers increased from 3.96% (LiF/Al) to 4.99% (BCP/LiF/Al) for rrP3HT:$PC_{61}BM$ and 4.66% (LiF/Al) to 5.65% (BCP/LiF/Al) for rrP3HT:$PC_{71}BM$. Moreover, from the dark J-V characteristic of all the fabricated devices no significant changes were observed in presence of both the metal nanoparticles.

All the device parameters including their average and maximum values were calculated from the J-V characteristics in presence of bare PEDOT:PSS and both the metal NPs blended PEDOT:PSS layers with all the cathode contacts viz. LiF/Al, BPhen/LiF/Al and BCP/LiF/Al (Table 4.2).[43] The calculated series and shunt resistance (R_s and R_{sh}) values are summarized in Table 4.3.

Table 4.3. Summary of the series and shunt resistance value of all the fabricated BHJ devices obtained from J-V characteristics curves.

Blend polymer	Hole Injecting Layer (HIL)	Device Configuration with ITO/HIL/Blend Polymer/	R_s ($\Omega.cm^{-2}$)	R_{sh} ($\Omega.cm^{-2}$)
(i) rrP3HT: $PC_{61}BM$	(a)Bare PEDOT:PSS	(1) LiF/Al	119	4921
		(2) BPhen/LiF/Al	112	5181
		(3) BCP/LiF/Al	100	5257
	(b)PEDOT:PSS+AgNPs	(4) LiF/Al	114	5021
		(5) BPhen/LiF/Al	95	7368
		(6) BCP/LiF/Al	88	8051
	(c)PEDOT:PSS+AuNPs	(7) LiF/Al	103	5089
		(8) BPhen/LiF/Al	99	7442
		(9) BCP/LiF/Al	82	8510
(ii) rrP3HT: $PC_{71}BM$	(a)Bare PEDOT:PSS	(10) LiF/Al	114	5488
		(11) BPhen/LiF/Al	107	6349
		(12) BCP/LiF/Al	103	6435
	(b)PEDOT:PSS+AgNPs	(13) LiF/Al	106	6583
		(14) BPhen/LiF/Al	102	8347
		(15) BCP/LiF/Al	101	8130
	(c)PEDOT:PSS+AuNPs	(16) LiF/Al	104	6775
		(17) BPhen/LiF/Al	98	8944
		(18) BCP/LiF/Al	102	8665

Figure. 4.18 and Figure. 4.19 represent the EQE and IQE spectra of all the fabricated devices.[48] All the EQE and IQE measurements were done under ambient conditions. From Figure. 4.18 it was observed that all the devices having BCP/LiF/Al as the cathode contact showed highest quantum efficiency compared to the other cathode contact in the wavelength range between 300 nm and 700 nm with EQE values over 55%. For rrP3HT:$PC_{61}BM$ with BCP/LiF/Al as cathode contact the maximum EQE values were

56.3%, 58.6% and 60.2% at 489 nm for bare PEDOT:PSS, PEDOT:PSS + AgNPs and PEDOT:PSS + AuNPs respectively.

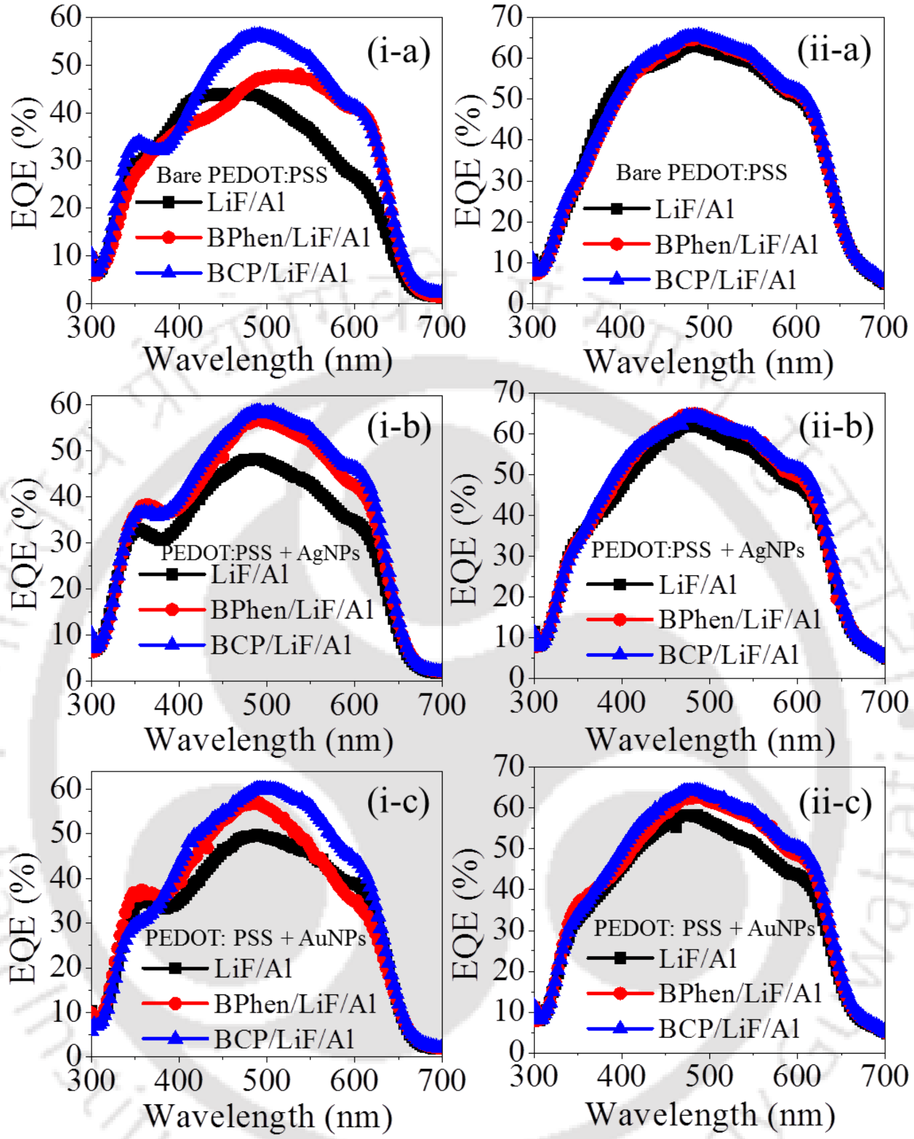

Figure 4.18. EQE spectra of (i) rrP3HT:PC$_{61}$BM and (ii) rrP3HT:PC$_{71}$BM BHJ solar cells with (a) bare PEDOT:PSS, (b) PEDOT:PSS + AgNPs and (c) PEDOT:PSS + AuNPs with different dual cathode buffer layers.

In case of rrP3HT:PC$_{71}$BM blend active layer system with same cathode contact the observed maximum EQE values for bare PEDOT:PSS, PEDOT:PSS + AgNPs and PEDOT:PSS + AuNPs were 64.2%, 64.47 % and 65.6% respectively at 470 nm wavelength values. All the calculated J$_{sc}$ value extracted from EQE spectra are also listed in Table 4.2. The estimated IQE spectra of all the devices are represented in Figure. 4.19. The observed wide (300 nm to 700 nm) and high IQE curves (~70%) of all the fabricated devices reveal that the morphology of both the blend polymer films deposited on the bare PEDOT:PSS and metal NPs blended PEDOT:PSS layers

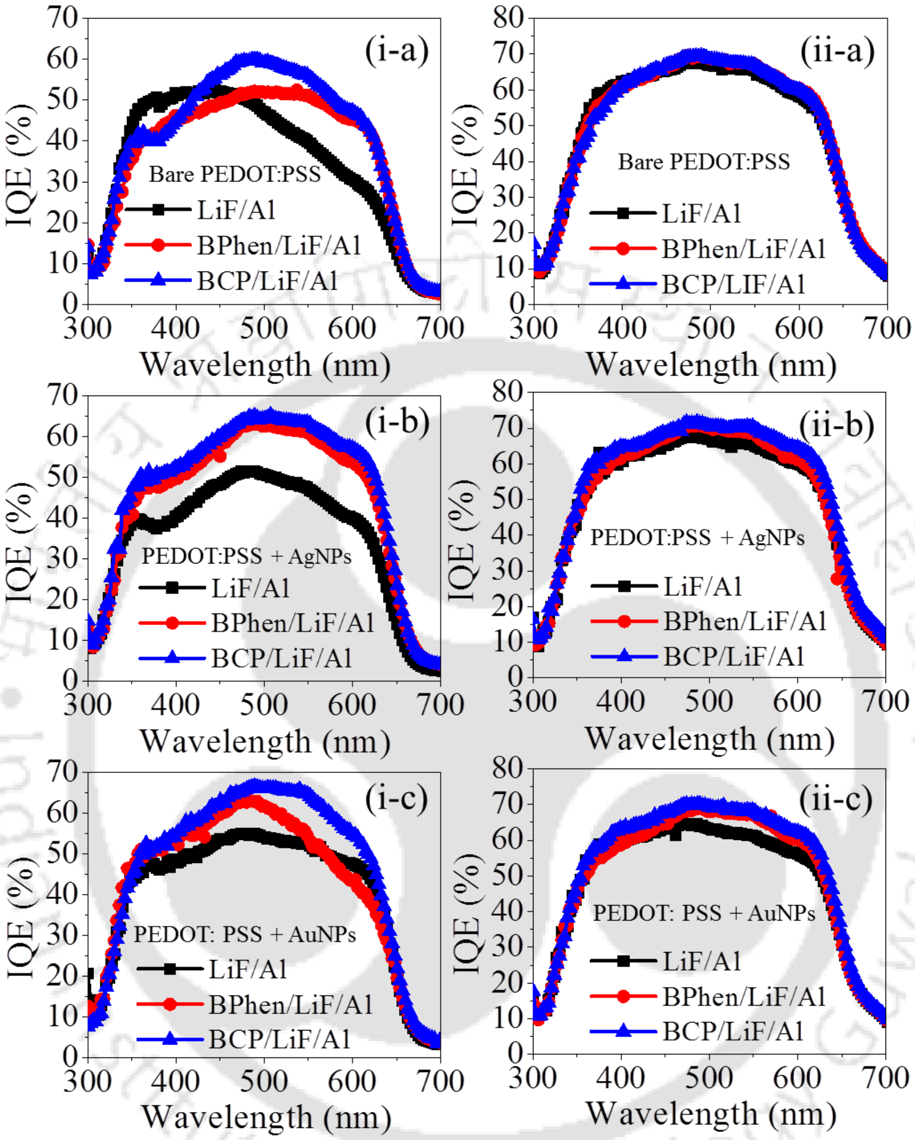

Figure 4.19. IQE spectra of (i) rrP3HT:PC$_{61}$BM and (ii) rrP3HT:PC$_{71}$BM BHJ solar cells with (a) bare PEDOT:PSS, (b) PEDOT:PSS + AgNPs and (c) PEDOT:PSS + AuNPs with different dual cathode buffer layers.

are ideal for the highly efficient BHJ solar cell. These results are in very good agreement with the experimental IQE data where a systematic increment in quantum efficiency in presence of PEDOT:PSS + AgNPs and PEDOT:PSS + AuNPs compared to bare PEDOT:PSS system was observed. To support these experimental data we further recorded the Nyquist plots (Figure. 4.20) of all the fabricated plasmonic BHJ solar cell. Generally, from the diameter of the semicircle of Nyquist plot the shunt resistance of the fabricated devices under its test condition can be determined. Herein, we observed that

BCP/LiF/Al contact had the largest shunt resistance as compared with the other contact, except the device having configuration (18), due to the less FF and higher Jsc value compared to BPhen/LiF/Al due to the presence of AuNPs.

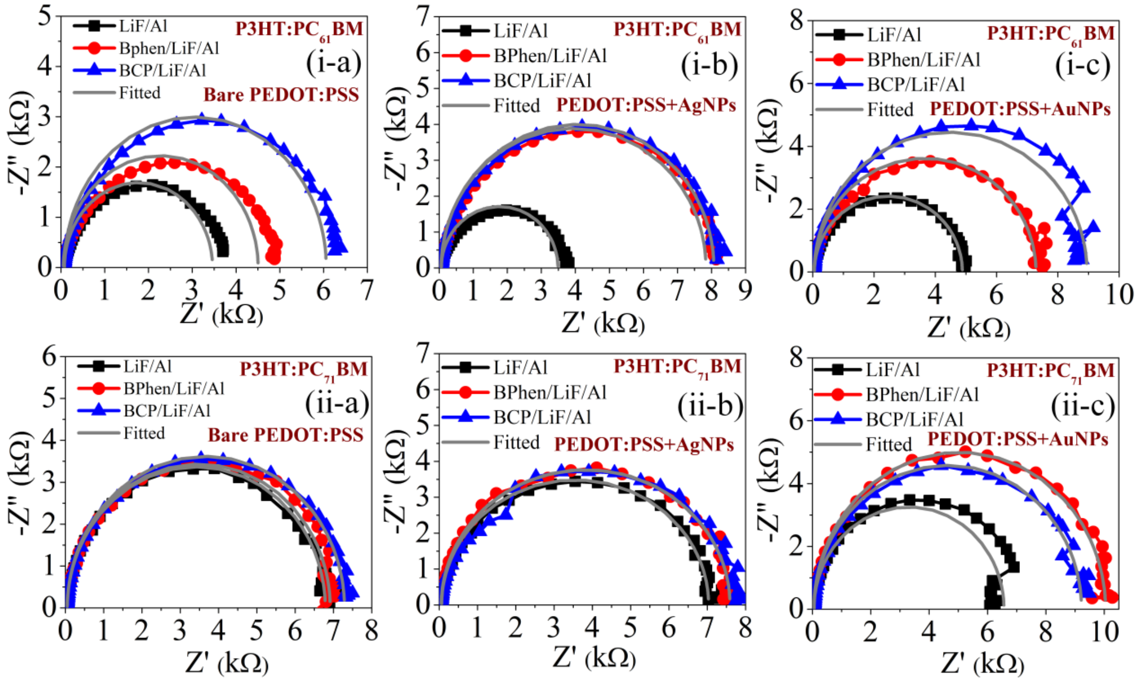

Figure 4.20. Nyquist plots of (i) rrP3HT:PC$_{61}$BM and (ii) rrP3HT:PC$_{71}$BM BHJ solar cells with (a) bare PEDOT:PSS, (b) PEDOT:PSS + AgNPs and (c) PEDOT:PSS + AuNPs with different dual cathode buffer layers.

In literature, different approaches are used to improve the efficiency of BHJ solar cells by incorporating different molecular modifications and device engineering. Modification of cathode contact by inserting functional buffer layer is one of the efficient approaches among them. Recently, it has also been reported that incorporation of metallic NP in various layers of the device architecture was an additional technique for improving the PCE of BHJ solar cell because of their strong interacting nature with solar photons. Especially, AuNPs and AgNPs have immense potential to be incorporated in the fabrication of BHJ solar cells since gold has less oxidation effect, whereas silver is cost effective compared to other metals. Table 4.4 provides a summary of recent data on P3HT:PCBM based bulk heterojunction solar cells having different device architecture modification in cathode buffer layers and incorporation of metallic NPs in various layer of BHJ solar cell for getting efficient device parformance.[49-62]

Table 4.4 Summary of recent literature data on P3HT:PCBM based BHJ cells using various cathode buffer layers and metal NPs.

Device configuration with ITO/PEDOT:PSS / P3HT:PCBM /	Effect of	Device Modified in	Improved PCE (%)	Reference
BPhen/Al	Buffer Layer	Cathode Contact	3.26	48
BPhen:Liq/Al	Buffer Layer	Cathode Contact	3.58	
BPhen:Cs_2CO_3/Al	Buffer Layer	Cathode Contact	3.54	
Yb/BCP/Ag	Buffer Layer	Cathode Contact	4.09	49
BCP/Ag	Buffer Layer	Cathode Contact	3.66	
BCP/LiF/Al	Buffer Layer	Cathode Contact	3.2	50
BCP: Liq/Al	Buffer Layer	Cathode Contact	3.5	
BCP/Al	Buffer Layer	Cathode Contact	4.11	51
BPhen/Al	Buffer Layer	Cathode Contact	3.32	52
CsI/BPhen/Al	Buffer Layer	Cathode Contact	3.51	
CsCl/BPhen/Al	Buffer Layer	Cathode Contact	3.72	
BCP:Ag (30nm)/Ag	Buffer Layer	Cathode Contact	3.44	53
LiF/Al	Metal NPs	AuNPs in PEDOT:PSS Layer	3.19	54
Ca/Al	Metal NPs	AuNPs in PEDOT:PSS Layer	4.24	55
Ca/Al	Metal NPs	AuNPs in PEDOT:PSS Layer	4.19	56
Al	Metal NPs	AuNPs in Active Layer	3.71	57
LiF/Al	Metal NPs	AuNPs modified ITO Layer	1.53	58
LiF/Al	Metal NPs	AuNPs in PEDOT:PSS and Active Layer	3.85	59
Ca/Al	Metal NPs	Au-Ag alloy NPs in active layer	4.73	60
Ca/Al	Metal NPs	Ag NPs and Ag Nanoprisms in active layer	4.30	61
Al	Metal NPs	AuNPs in Anodic Buffer Layer	2.45	62

The dispersion of AuNPs and AgNPs in PEDOT:PSS layer is comparatively easy and straightforward. Since PEDOT:PSS can be dispersed in aqueous medium; therefore, the AuNPs and AgNPs synthesized by chemical reduction method can be easily mixed with PEDOT:PSS without any chemical functionalization. In this regard, without using a stabilizer, NaBH4 based AuNPs synthesized directly in PEDOT:PSS increases the PCE value up to 3.19% of P3HT:PCBM based solar cell with LiF/Al as cathode contact.[52] It has been found that the size of the metal NPs can also strongly affect the efficiency of BHJ solar cell. AuNPs with 50 nm size doped in PEDOT:PSS layer increases the efficiency of P3HT:PCBM based solar cell from 3.57% to 4.24%.[56] Again, the combination of Au-Ag alloy NPs in active layer further increases the PCE value of P3HT:PCBM based solar cell with Ca/Al as cathode contact up to 4.73%.[61] Yet, to the best of our knowledge, the maximum PCE value of P3HT:PCBM solar cell reported with bare PEDOT:PSS and BCP/Al cathode contact is 4.11%.[52]

In this study, we have successfully improved the PCE value of both the rrP3HT:$PC_{61}BM$ and rrP3HT:$PC_{71}BM$ based solar cells by the collective effect of the plasmonic metal NPs and the dual cathode buffer layer. Two different types of metal NPs, namely AgNPs and AuNPs are blended separately in the PEDOT:PSS hole transport layer. For the dual cathode buffer layer, we chose two different hole blocking layers, BPhen and BCP, along with LiF/Al conventional blocking layers. For both the blend polymer systems the observed PCE increases significantly in the presence of PEDOT:PSS + AuNPs and PEDOT:PSS + AgNPs with BCP/LiF/Al as the cathode contact because of better band alignment of the dual cathode buffer layers with the active layers and the superior surface plasmonic effect of the metallic NPs. We observed the best device performance in the presence of AuNPs because of its surface plasmon resonance at the visible region. The results demonstrated here successfully explain the role of metal NP modified PEDOT:PSS layers with different dual cathode buffer layers and their contribution to the overall device performance. Moreover, this study introduced a very easy and simple technique for the fabrication of highly efficient organic BHJ solar cell based on rrP3HT:$PC_{61}BM$ and rrP3HT:$PC_{71}BM$ with PCE close to 6 %, a value which can be further improved by engineering the device architecture and by using preferential additives.

4.3 Conclusion

In conclusion, the combined influence of different dual cathode buffer layers with two different metal NPs on the performance of rrP3HT:$PC_{61}BM$ and rrP3HT:$PC_{71}BM$ based bulk heterojunction solar cell was demonstrated. Both the metal NPs, i.e. AuNPs and AgNPs that were utilized for device fabrication were freshly synthesized by chemical reduction method with tri-sodium citrate as reducing and stabilizing agent. The significance of both the NPs contained PEDOT:PSS layer on the device performances were justified by their remarkable performances and these results were compared with conventional device architecture. It was established that the device comprising PEDOT:PSS + AuNPs with BCP/LiF/Al cathode contact showed the best device performance i.e. η=5.65% with J_{sc}=16.1 mA/cm^2, V_{oc}=0.58 V and FF=61% for rrP3HT:$PC_{71}BM$ and η=4.99% with J_{sc}=13.9 mA/cm^2, V_{oc}=0.59 V and FF= 62% for rrP3HT:$PC_{61}BM$ compared to the PEDOT:PSS + AgNPs and bare PEDOT:PSS device architecture containing the same dual cathode contact. This PEDOT:PSS + AuNPs with BCP/LiF/Al device architecture showed better results compared to all the other devices reported here due to the simultaneous effect of AuNPs which improves the absorption length by scattering of incident solar photon and the BCP/LiF dual cathode buffer layer that can block more holes to minimize the charge recombination between the blend polymer-cathode contacts. Overall, in this study we could successfully demonstrate a very simple and easy fabrication technique to achieve highly efficient organic BHJ solar cells by combination the two effects simultaneously.

4.4 References

1. Christopher, P.; Xin, H., Marimuthu, A.; Linic, S. Singular Characteristics and Unique Chemical Bond Activation Mechanisms of Photocatalytic Reactions on Plasmonic Nanostructures. *Nat. Mater.* **2012**, *11*, 1044–1050.

2. Banerjee, S.; Pillai, S. C.; Falaras, P.; O'Shea, K. E.; Byrne, J. A.; Dionysiou, D. D. New Insights into the Mechanism of Visible Light Photocatalysis. *J. Phys. Chem. Lett.* 2014, **5**, 2543–2554.

3. Ravelli, D.; Fagnoni, M.; Albini, A. Photoorganocatalysis. What for? *Chem. Soc. Rev.* **2013**, *42*, 97–113.

4. Lang, X. J.; Chen, X. D.; Zhao, J. C. Heterogeneous Visible Light Photocatalysis for Selective Organic Transformations. *Chem. Soc. Rev.* **2014**, *43*, 473–486.

5. Ma, W. L.; Yang, C. Y.; Gong, X.; Lee K.; Heeger, A. J. Thermally Stable, Efficient Polymer Solar Cells with Nanoscale Control of the Interpenetrating Network Morphology. *Adv. Funct. Mate*r. **2005**, *15*, 1617–1622.

6. Deibe,l C.; Dyakonov, V. Polymer–Fullerene Bulk Heterojunction Solar Cells. *Rep. Prog. Phys.* **2010**, *73*, 096401.

7. Dennler, G.; Scharber M. C.; Brabec, C. J. Polymer-Fullerene Bulk-Heterojunction Solar Cells. *Adv. Mater.* **2009**, *21*, 1323–1338.

8. Li, G.; Zhu, R.; Yang, Y. Polymer Solar Cells. *Nat. Photonics* **2012**, ***6***, 153–161.

9. Li, G.; Shrotriya, V.; Huang, J. S.; Yao, Y.; Moriarty, T.; Emery, K.; Yang, Y. High-Efficiency Solution Processable Polymer Photovoltaic Cells by Self-Organization of Polymer Blends. *Nat. Mater.* **2005**, *4*, 864–868.

10. Su, Y.-W.; Lan, S.-C.; Wei, K.-H. Organic Photovoltaics. *Mater. Today* **2012**, *15*, 554–562.

11. Nelson, J. Polymer:Fullerene Bulk Heterojunction Solar Cells. *Mater. Today*, **2011**, *14*, 462–470.

12. Walter, M. G.; Warren, E. L.; McKone, J. R.; Boettcher, S. W.; Mi, Q. X.; Santori, E. A.; Lewis, N. S. Solar Water Splitting Cells. *Chem. Rev.* **2010**, *110*, 6446–6473.

13. Jørgensen, M.; Norrman, K.; Gevorgyan, S. A.; Tromholt, T.; Andreasen, B.; Krebs, F. C. Stability of Polymer Solar Cells. *Adv. Mater.* **2012**, *24*, 580–612.

14. Jiang, R. B.; Li, B. X.; Fang, C. H.; Wang, J. F. Metal/Semiconductor Hybrid Nanostructures for Plasmon-Enhanced Applications. *Adv. Mater.* **2014**, *26*, 5274–5309.

15. Grossiord, N.; Kroon, J. M.; Andriessen, R.; Blom, P. W. M. Degradation Mechanisms in Organic Photovoltaic Devices. *Org. Electron.* **2012**, *13*, 432–456.

16. Zhang, X.; Liu, Y.; Lee, S.-T.; Yang, S.; Kang, Z. Coupling Surface Plasmon Resonance of Gold Nanoparticles with Slow-Photon-Effect of TiO_2 Photonic Crystals for Synergistically Enhanced Photoelectrochemical Water Splitting. *Energy Environ. Sci.* **2014**, *7*, 1409–1419.

17. Liu, C.-M.; Chen, C.-M.; Su, Y.-W.; Wang, S.-M.; Wei, K.-H. The Dual Localized Surface Plasmonic Effects of Gold Nanodots and Gold Nanoparticles Enhance the Performance of Bulk Heterojunction Polymer Solar Cells. *Org. Electron.* **2013**, *14*, 2476–2483.

18. Hu, T.; Li, L.; Xiao, S.; Yuan, K.; Yang, H.; Chen, L.; Chen, Y. In Situ Implanting Carbon Nanotube-Gold Nanoparticles into ZnO as Efficient Nanohybrid Cathode Buffer Layer for Polymer Solar Cells. *Org. Electron.* **2016**, *38*, 350–356.

19. Yuan, K.; Chen, L.; Chen, Y. In Situ Photocatalytically Heterostructured ZnO–Ag Nanoparticle Composites as Effective Cathode-Modifying Layers for Air-Processed Polymer Solar Cells. *Chem. Eur. J.* **2015**, *21*, 11899–11906.

20. Yuan, K.; Chen, L.; Chen, Y. Optical Engineering of Uniformly Decorated Graphene Oxide Nanoflakes via in Situ Growth of Silver Nanoparticles with Enhanced Plasmonic Resonance. *ACS Appl. Mater. Interfaces.* **2014**, *6*, 21069–21077.

21. Yuan, K.; Chen, L.; Chen, Y. Versatile Electron-Collecting Interfacial Layer by in Situ Growth of Silver Nanoparticles in Nonconjugated Polyelectrolyte Aqueous Solution for Polymer Solar Cells. *J. Phys. Chem. B* **2014**, *118*, 11563–11572.

22. Chiu, M.-Y.; Jeng, U.-S.; Su, M.-S.; Wei, K.-H. Morphologies of Self-Organizing Regioregular Conjugated Polymer/Fullerene Aggregates in Thin Film Solar Cells *Macromolecules* 2010, **43**, 428–432.

23. Chiu, M.-Y.; Jeng, U.-S.; Su, C.-H.; Liang, K. S.; Wei, K.-H. Simultaneous Use of Small- and Wide-Angle X-ray Techniques to Analyze Nanometerscale Phase Separation in Polymer Heterojunction Solar Cells. *Adv. Mater.* **2008**, *20*, 2573–2578.

24. Schilinsky, P.; Waldauf, C.; Brabec, C. J. Recombination and Loss Analysis in Polythiophene based Bulk Heterojunction Photodetectors. *Appl. Phys. Lett.* **2002**, *81*, 3885–3887.

25. Street, R. A.; Schoendorf, M.; Roy, A.; Lee, J. H. Interface State Recombination in Organic Solar Cells. *Phys. Rev. B* **2010**, *81*, 205307.

26. Jung, K.; Song, H. -J.; Lee, G.; Ko, Y.; Ahn, K.; Choi, H.; Kim, J. Y.; Ha, K.; Song, J.; Lee, J.-K.; Lee, C.; Choi, M. Plasmonic Organic Solar Cells Employing Nanobump Assembly via Aerosol-Derived Nanoparticles. *ACS Nano* **2014**, *8*, 2590–2601.

27. Fung, D. D. S.; Qiao, L. F.; Choy, W. C. H.; Wang, C.; Sha, W. E. I.; Xie, F.; He, S. Optical and Electrical Properties of Efficiency Enhanced Polymer Solar Cells with Au Nanoparticles in a PEDOT–PSS Layer. *J. Mater. Chem.* **2011**, *21*, 16349–16356.

28. Halls, J. J. M.; Pichler, K.; Friend, R. H.; Moratti, S. C.; Holmes, A. B. Exciton Diffusion and Dissociation in a Poly(p-Phenylenevinylene)/C_{60} Heterojunction Photovoltaic Cell. *Appl. Phys. Lett.* **1996**, ***68***, 3120–3122.

29. Theander, M.; Yartsev, A.; Zigmantas, D.; Sundström, V.; Mammo, W.; Andersson, M. R.; Inganäs, O. Photoluminescence Quenching at a Polythiophene/C_{60} Heterojunction. *Phys. Rev. B* **2000**, *61*, 12957–12963.

30. Kirchartz, T.; Agostinelli, T.; Campoy-Quiles, M.; Gong, W.; Nelson, J. Understanding the Thickness-Dependent Performance of Organic Bulk Heterojunction Solar Cells: The Influence of Mobility, Lifetime, and Space Charge. *J. Phys. Chem. Lett.* **2012**, ***3***, 3470−3475.

31. Nam, Y. M.; Huh, J.; Jo, W. H. Optimization of Thickness and Morphology of Active Layer for High Performance of Bulk-Heterojunction Organic Solar Cells. *Sol. Energy Mater. Sol. Cells* **2010**, *94*, 1118–1124.

32. Namkoong, G.; Kong, J.; Samson, M.; Hwang, I. W.; Lee, K. Active Layer Thickness Effect on the Recombination Process of PCDTBT: $PC_{71}BM$ Organic Solar Cells. *Org. Electron.* **2013**, *14*, 74–79.

33. Wong, W.-Y.; Wang, X.-Z.; He, Z.; Djurisic, A. B.; Yip, C.-T.; Cheung, K.-Y.; Wang, H.; Mak, C. S. K.; Chan, W.-K. Metallated Conjugated Polymers as a New Avenue towards High-Efficiency Polymer Solar Cells *Nat. Mater.* **2007**, *6*, 521–527.

34. Pandey, R.; Holmes, R. J. Graded Donor-Acceptor Heterojunctions for Efficient Organic Photovoltaic Cells. *Adv. Mater.* **2010**, ***22***, 5301–5305.

35. Hoven, C. V.; Dang, X.-D.; Coffin, R. C.; Peet, J.; Nguyen, T.-Q.; Bazan, G. C. Improved Performance of Polymer Bulk Heterojunction Solar Cells Through the Reduction of Phase Separation via Solvent Additives. *Adv. Mater.* **2010**, *22*, E63–E66.

36. Brabec, C. J.; Shaheen, S. E.; Winder, C.; Sariciftci, N. S.; Denk, P. Effect of LiF/Metal Electrodes on the Performance of Plastic Solar Cells. *Appl. Phys. Lett.* **2002**, *80*, 1288–1290.

37. Hill, I. G.; Rajagopal, A.; Kahn, A.; Hu, Y. Molecular Level Alignment at Organic Semiconductor-Metal Interfaces. *Appl. Phys. Lett.* **1998**, *73*, 662–664.

38. Reinspach, J. A.; Diao, Y.; Giri, G.; Sachse, T.; England, K.; Zhou, Y.; Tassone, C.; Worfolk, B. J.; Presselt, M.; Toney, M. F.; Mannsfeld, S.; Bao, Z. Tuning the Morphology of Solution-Sheared P3HT:PCBM Films. *ACS Appl. Mater. Interfaces* **2016**, *8*, 1742–1751.

39. Shao, M.; Keum, J.; Chen, J.; He, Y.; Chen, W.; Browning, J. F.; Jakowski, J.; Sumpter, B. G.; Ivanov, I. N.; Ma, Y.-Z.; Rouleau, C. M.; Smith, S. C.; Geohegan, D. B.; Hong K.; Xiao K. The Isotopic Effects of Deuteration on Optoelectronic Properties of Conducting Polymers. *Nat. Commun.* **2014**, *5*, 4180.

40. Singh, A.; Dey, A.; Das, D.; Iyer, P. K. Effect of Dual Cathode Buffer Layer on the Charge Carrier Dynamics of rrP3HT:PCBM based Bulk Heterojunction Solar Cell. *ACS Appl. Mater. Interfaces* **2016**, *8*, 10904–10910.

41. Guo, S.; Ruderer, M. A.; Rawolle, M.; Körstgens, V.; Birkenstock, C.; Perlich, J.; Müller-Buschbaum, P. Evolution of Lateral Structures during the Functional Stack Build-up of P3HT:PCBM-Based Bulk Heterojunction Solar Cells. *ACS Appl. Mater. Interfaces* **2013**, ***5***, 8581–8590.

42. Müller-Buschbaum, P. The Active Layer Morphology of Organic Solar Cells Probed with Grazing Incidence Scattering Techniques. *Adv. Mater.* **2014**, *16*, 7692–7709.

43. Oesinghaus, L.; Schlipf, J.; Giesbrecht, N.; Song, L.; Hu, Y.; Bein, T.; Docampo, P.; Müller-Buschbaum, P. Toward Tailored Film Morphologies: The Origin of Crystal Orientation in Hybrid Perovskite Thin Films. Adv. Mater. Interfaces, 2016, 3, 1600403.

44. Jiang, Z. GIXSGUI: a MATLAB Toolbox for Grazing-Incidence X-Ray Scattering Data Visualization and Reduction, and Indexing of Buried Three-Dimensional Periodic Nanostructured Films. *J. Appl. Crystallogr.* **2015**, *48*, 917–926.

45. Notarianni, M.; Vernon, K.; Chou, A.; Aljada, M.; Liu, J. Z.; Motta, N. Plasmonic Effect of Gold Nanoparticles in Organic Solar Cells. *Sol. Energy* **2014**, *106*, 23–37.

46. Luber, E. J.; Buriak, J. M. Reporting Performance in Organic Photovoltaic Devices. *ACS Nano* **2013**, *7*, 4708–4714.

47. Zimmermann, E.; Ehrenreich, P.; Pfadler, T.; Dorman, J. A.; Weickert, J.; Schmidt-Mende, L. Erroneous Efficiency Reports Harm Organic Solar Cell Research. *Nat. Photonics* **2014**, *8*, 669–672.

48. Wang, T.; Chen, C.; Guo, K.; Chen, G.; Xu, T.; Wei, B. Improved Performance of Polymer Solar Cells by using Inorganic, Organic, and Doped Cathode Buffer Layers. *Chin. Phys. B* **2016**, *25,* 038402.

49. Oh, I. S.; Ji, C. H.; Oh, S. Y. Effects of Ytterbium on Electrical and Optical Properties of BCP/Ag/WO_3 Transparent Electrode based Organic Photovoltaic Cells *Electron. Mater. Lett.* **2016**, *12*, 156–162.

50. Kim, J.-H.; Park, J.-G. Effect of a Co-evaporated Alq_3:Liq Cathode Buffer Layer on the Performance of a Polymer Photovoltaic Cell. *J. Korean. Phys. Soc.* 2015, **66**, 1872–1878.

51. Chang, C.-C.; Lin, C.-F.; Chiou, J.-M.; Ho, T.-H.; Tai, Y.; Lee, J.-H.; Chen, Y.-F.; Wang, J.-K.; Chen, L.-C.; Chen, K.-H. Effects of Cathode Buffer Layers on the Efficiency of Bulk-Heterojunction Solar Cells. *Appl. Phys. Lett.* **2010**, *96,* 263506.

52. Xiao, T.; Fungura, F.; Cai, M.; Anderegg, J. W.; Shinar, J.; Shinar, R. Improved Efficiency and Stability of Inverted Polymer Solar Cells with a Solution-Processed BPhen Interlayer and Polystyrene Beads. *Org. Electron.* **2013**, *14*, 2555–2563.

53. Jung, G. H.; Lee, J.-L. Origin of Gap States in the Electron Transport Layer of Organic Solar Cells. *J. Mater. Chem. A* **2013**, *1*, 3034–3039.

54. Woo, S.; Jeong, J. H.; Lyu, H. K.; Han, Y. S.; Kim, Y. In Situ-Prepared Composite Materials of PEDOT:PSS Buffer Layer-Metal Nanoparticles and their Application to Organic Solar Cells. *Nanoscale Res. Lett.* **2012**, *7*, 641.

55. Wu, J. L.; Chen, F. C.; Hsiao, Y. S.; Chien, F. C.; Chen, P. L.; Kuo, C. H.; Huang, M. H.; Hsu, C. S. Surface Plasmonic Effects of Metallic Nanoparticles on the Performance of Polymer Bulk Heterojunction Solar Cells. *ACS Nano* 2011**, 5**, 959–967.

56. Chen, F. C.; Wu, J. L.; Lee, C. L.; Hong, Y.; Kuo, C. H.; Huang, M. H. Plasmonic-Enhanced Polymer Photovoltaic Devices Incorporating Solution Processable Metal Nanoparticles. *Appl. Phys. Lett.* **2009**, *95*, 013305.

57. Spyropoulos, G. D.; Stylianakis, M. M.; Stratakis, E.; Kymakis, E. Organic Bulk Heterojunction Photovoltaic Devices with Surfactant-Free Au Nanoparticles Embedded in the Active Layer. *Appl. Phys. Lett.* **2012**, *100*, 213904.

58. Shahin, S.; Gangopadhyay, P.; Norwood, R. A. Ultrathin Organic Bulk Heterojunction Solar Cells: Plasmon Enhanced Performance using Au Nanoparticles. *Appl. Phys. Lett.* **2012**, *101*, 053109.

59. Xie, F.-X.; Choy, W. C. H.; Wang, C. C. D.; Sha, W. E. I.; Fung, D. D. S. Improving the Efficiency of Polymer Solar Cells by Incorporating Gold Nanoparticles into all Polymer Layers. *Appl. Phys. Lett.* **2011**, *99*, 153304.

60. Chen, H.-C.; Chou, S.-W.; Tseng, W.-H.; Chen, I. W. P.; Liu, C.-C.; Liu, C.; Liu, C.-L.; Chen, C.-H.; Wu, C.-I.; Chou, P.-T. Large AuAg Alloy Nanoparticles Synthesized in Organic Media Using a One-Pot Reaction: Their Applications for High-Performance Bulk Heterojunction Solar Cells. *Adv. Funct. Mater.* **2012**, *22*, 3975–3984.

61. Li, X. H.; Choy, W. C. H.; Lu, H. F.; Sha, W. E. I.; Ho, A. H. P. Efficiency Enhancement of Organic Solar Cells by using Shape-Dependent Broadband Plasmonic Absorption in Metallic Nanoparticles. *Adv. Funct. Mater.* **2013**, *23*, 2728–2735.

62. Khoo, S. Y.; Yang, H. B.; He, Z. M.; Miao, J. W.; Leong, K. C.; Li, C. M.; Tan, T. T. Y. Enhanced Charge Extraction of Polymer Solar Cell by Solution-Processable Gold Nanoparticles. *J. Mater. Chem. C* **2013**, *1*, 5402–5409.

Chapter 5

Collective Effect of Hybrid Metals Nanoparticles and Dual Cathode Buffer Layers on PCE of Organic BHJ Solar Cell

The augmented universal demand of cost efficacious sustainable energy sources has inspired researchers and engineers in identical proportions to develop new methods to convert solar energy into electrical energy.[1-5] Among them, the third generation Organic Photovoltaic (OPV) technology is one of the most promising one because of its capability to obtain a faster, economical and their compatibility with larger area and flexible substrates to assemble devices compared to the conventional first generation- silicon wafer and second generation-CdTe and CIGS based thin film solar cell technologies.[6-9] The Organic Bulk Heterojunction (BHJ) solar cell is one of the third-generation solar cells having its simplest device architecture with a blend active layer of two kinds of organic material, one is electron donator and the other electron acceptor. However, because of the low carrier mobility of organic semiconductors, the Power Conversion Efficiency (PCE) of BHJ organic solar cells are not yet high enough for commercialization. Therefore, efforts to develop the PCE of BHJ organic solar cells has become one of the most interesting research topics at the present time due to their promising application as a replacement of their inorganic counter parts in future.[10-15]

The efficiency of BHJ solar cell are mainly influence by two parameters, viz., (1) the light absorption capability of the blend active materials, and (2) the dissociated charge collection ability of the contact electrodes. There are several methods already reported in the literature to overcome these factors.[16-25] Since the organic active materials have very low carrier mobility and the photo generated excitons have shorter lifetime, the thickness of the active layer blends are restricted to a few nanometre range, which further reduces the absorption path length. Again, on increasing the thickness, the dissociated charges start to recombine inside the active layer itself and only a few are able to reach at the electrodes, which further decreases the PCE value.[26-29] For improving the point (1), trapping of light by the inducing plasmonic metal nanoparticles (NPs) in the various layers of BHJ solar cells was found to be useful for better photo absorption in organic BHJ solar cells. Al, Ag, Au and Cu are some standard metal nanoparticles generally used in organic solar cell applications as they are able to show strong localized surface plasmon resonances (LSPRs) property near UV, visible and near infrared (NIR) wavelength regions by interacting with incident sunlight. Specifically, Al and Ag lead to SPR in the UV region while Au and Cu show in the visible spectrum. Surface plasmon is the physical phenomenon where bound excitation is generated on noble metal surface when incident photon interacted with the free conduction electrons of the metal surface. After excitation, surface plasmon decay either by radiatively or non-radiatively, follow-on absorption or scattering of light respectively, as result of which internal absorption path length increases.[30-33]

On the contrary, in order to improve the point (2), the contact interfacial layer plays very important role for improving the efficiency of BHJ solar cells by modulating the electrode work function and thereby increasing the selectivity towards the particular carrier.[34,35] The coalescence of a definite interfacial layer with cathode aims to increment the short circuit current density (J_{sc}) and open circuit voltage (V_{oc}), by transmuting the built-in-potential engendered by the electrodes work function difference. This modification support the charge carriers to move easily towards their respective contacts and as a result of which efficiency increases.[36,37] Further, by combining these two phenomenon, namely, the plasmon induced metallic nanoparticle effect and the effect of cathode interfacial layer, the efficiency of organic BHJ solar cells can be modified.

In this study, the collective effect of plasmon induced hybrid metal nanoparticles (NPs) and the dual cathode interfacial layers on improving the power conversion efficiency of regioregular P3HT-PCBM based Bulk Hetero Junction solar cell are systematically demonstrated. Initially, two different types of plasmonic NPs, viz. citrate stabilized gold (Au) and silver (Ag) were separately synthesized and then physically blended together with three different volume ratio [AuNPs + AgNPs (25:75), AuNPs + AgNPs (50:50) and AuNPs + AgNPs (75:25)]. These three blended nanoparticle solutions were then mixed with hole injecting layer (HIL) PEDOT:PSS and their collective effect was systematically observed with cathode electrode modified by different interfacial organic materials with rrP3HT:$PC_{61}BM$ and rrP3HT:$PC_{71}BM$ as the blend active system respectively. Two different hole blocking organic materials namely, BPhen and BCP, along with LiF/Al were chosen together as modified cathode contact. For both the blend active layers, it was observed that the efficiency of BHJ solar cell increases notably in presence of PEDOT:PSS + AuNPS:AgNPs (25:75) HIL layer with BCP/LiF/Al as the cathode electrode compared to other combination because of the energy level alignment of BCP/LiF/Al with the active blends and excellent SPR of the AuNPs:AgNPs (25:75) at the UV-visible region compared to AuNPs:AgNPs (50:50) and AuNPs:AgNPs (75:25).

5.1 Experiments

5.1.1 Materials

In this chapter, for the synthesis of Au and Ag nanoparticles, Gold (III) chloride trihydrate ($HAuCl_4·3H_2O$) (M_w ~393.83 g/mol, Sigma Aldrich, India), Silver nitrate ($AgNO_3$) (M_w ~169.87 g/mol, Sigma Aldrich, India) and tri-sodium citrate 2-hydrate (Merck Specialties Pvt Ltd) were used without any further purification. For the solar cells fabrication, Indium tin oxide (ITO) substrate (R_{Sheet}~15Ω/sq., Sigma Aldrich, India), Poly (3, 4-ethylenedioxythiophene)-poly (styrenesulfonate) (PEDOT:PSS, Sigma Aldrich, India), [6, 6]-Phenyl C_{61} butyric acid methyl ester ($PC_{61}BM$) (M_w ~910.88 g/mol, Sigma Aldrich, India), were purchased and used as received. For cathode, Aluminium wire (99.999% purity) and the cathode interfacial layers, namely, Bathocuproine (BCP) (M_w ~360.45 g/mol, Sigma Aldrich, India), Bathophenanthroline (BPhen) (M_w~332.40 g/mol, Sigma Aldrich, India) and Lithium Fluoride (LiF, Sigma Aldrich, India) are also used as received. [6, 6]-Phenyl C_{71} butyric acid methyl ester ($PC_{71}BM$) (M_w ~1030.93 g/mol, 99.5% pure) was purchased from Luminescence Technology Corp., Taiwan and used as received. The donor polymer, regioregular poly (3-hexylthiophene-2, 5-diyl) (rrP3HT) (M_w~83 kg/mol) was used as received from Sycon Polymers India Private Limited.

5.1.2 Characterization Details

The synthesized bare and blended metal NPs with different ratios were characterized by Jaz UV-Vis spectrophotometer and Tecnai G2 F20 S-twin JEOL 2100 transmission electron microscope respectively to determine the absorbance and the size of the NPs. Laurell spin coaters were used for the deposition of metal NPs doped PEDOT:PSS in ambient condition and the rrP3HT: PCBM active layer blends were coated upon NPs doped PEDOT:PSS layer using Spin 150 spin coaters inside the glove box. The thicknesses of all the layers of the fabricated BHJ devices were measured by using Veeco Dektak 150 Surface Profilometer. All the photovoltaics properties namely, J-V characteristics, external quantum efficiency (EQE) and impedance spectroscopy of the fabricated devices were measured by Newport Oriel Sol 3A solar simulator, Oriel IQE-200 instrument and CH 680 Instrument respectively connecting with Keithley-2400 digital source meter.

5.1.3 Device Fabrication

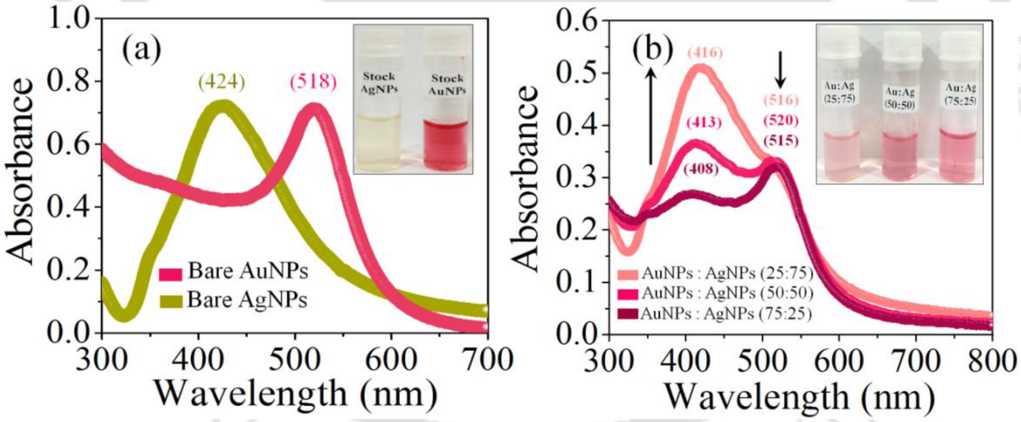

Figure 5.1. UV-Vis absorption study of (a) the synthesized Au and Ag Nanoparticles and (b) blended AuNPs: AgNPs at three different blend ratios.

The plasmonic AuNPs and AgNPs were synthesized by simple chemical reduction method in double distilled water using tri-sodium citrate 2-hydrate as the reducing and stabilizing agent. For AuNPs synthesis, 50 mL of 10 mM $HAuCl_4$ was heated up to boiling with continuous stirring using a hot plate containing controlled magnetic stirrer. When the solution boiled and the temperature reached up to 100°C, 1.5% tri-sodium citrate 2-hydrate was rapidly added to the solution with simultaneous stirring. Due to the reduction mechanism, the colour of the solution changes slowly from transparent light yellow to characteristic wine red, which signifies the formation of very smaller sized

AuNPs. Similar procedure was followed for the synthesis of AgNPs. In this case, 50 mL of 1 mM $AgNO_3$ was heated up to its boiling point and when the solution boiled, 5 mL of 1% tri-sodium citrate 2-hydrate was added drop wise to it with vigorous stirring. The solution was mixed vigorously until it changed to the characteristic yellowish brown. Both the solutions, after the formation of the nanoparticles were removed from the hot plate and stirred until the temperature reached room temperature. The NPs were then characterized by UV-visible spectrophotometer, FESEM and TEM analysis to determine the characteristics absorption peaks and the size of the particles. The observed UV-Vis plasmonic peaks of AuNPs and AgNPs were observed at 518 nm and 424 nm (Figure. 5.1a) and their corresponding average sizes were observed as ~10 nm for AuNPs and ~20 nm for respectively (shown as Figure. 4.3 and Figure 4.4 in Chapter 4).

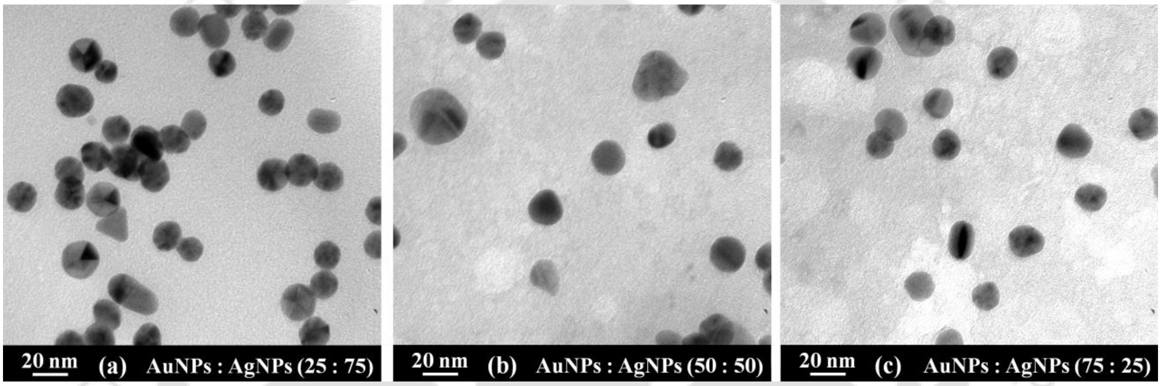

Figure 5.2. TEM images of blended AuNPs: AgNPs at three different blend ratios.

For the fabrication of plasmonic BHJ solar cell, initially three different blend solutions of metal nanoparticles were prepared from the above mentioned bare nanoparticles solutions namely, (A) AuNPs:AgNPs (25:75) vol %, (B) AuNPs:AgNPs (50:50) vol % and (C) AuNPs:AgNPs (75:25) vol % which were again characterized by UV-Vis spectrophotometer and TEM analysis (Figure. 5.1b and Figure. 5.2) to further determine the characteristic absorption peaks and the average size/shape of the particles. From UV-Vis absorption spectra it was observed that both the characteristic peaks of AuNPs and AgNPs were present in the same positions after the physical blending which signified no deformation occurring in the average size or shape of the nanoparticles (Figure.5.1b). These results were supported by TEM analyses which are shown in Figure. 5.2. The blend solutions of the metal NPs were then mixed with PEDOT:PSS hole injecting layer (HIL) with a doping concentration of 20% (v/v). The doping concentration of the blended metal nanoparticles into the PEDOT:PSS layer were standardized prior to the BHJ device fabrication by measuring the thin film resistivity of the doped PEDOT:PSS layer. It was observed that the thin film resistivity value of the NPs modified PEDOT:PSS layers for 20% (v/v) was lesser compared to the other doping concentration (Figure. 5.3).

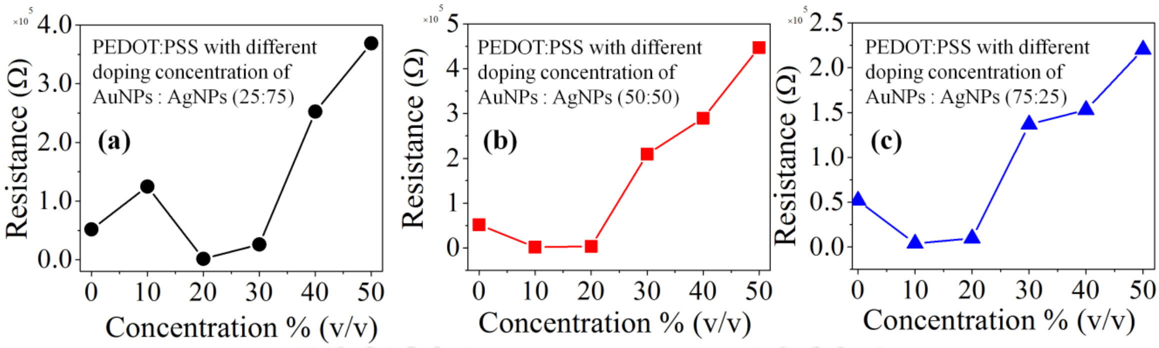

Figure. 5.3. Graphical representation of resistive device of PEDOT:PSS layer at different concentration of (a) AuNPs: AgNPs (25:75), (b) AuNPs: AgNPs (50:50) and (c) AuNPs: AgNPs (75:25).

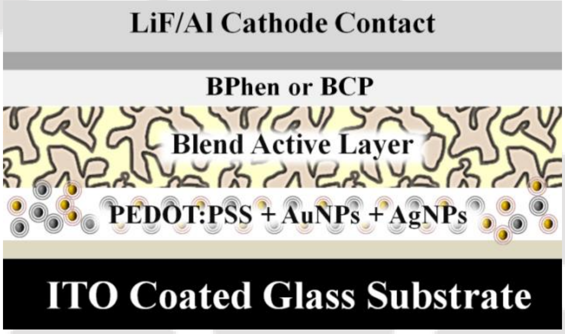

Figure 5.4. Schematic of the fabricated plasmonic bulk hetero junction solar cell.

Following this, the new HILs, were spun on the pre-cleaned, UV-ozone modified ITO substrate (~40 nm) and annealed at 120 °C for 30 minutes in globe box. Since the average size of these blended NPs is very small (< 25 nm) compared to the thickness of HIL, hence it does not create any significant change in the morphology of the HIL film. The rest of the BHJ cell fabrication processes are similar to previously reported literature.[38] The layer-by-layer schematic of the fabricated plasmonic BHJ cells with regioregular P3HT:PCBM (blend active layer) dual cathode interfacial layer is shown in Figure. 5.4.

5.2 Results and Discussion

5.2.1 Photovoltaic Characterizations

The schematic of the mechanism involved in the fabricated plasmonic solar cell containing three different hybrid NPs doped hole injecting layers and dual cathode interfacial layers are represented in Figure. 5.5. In this case, two different phenomenon, i.e., (1) the plasmonic effect of the hybridizes metal NPs and (2) the influence of dual cathode interfacial layers, simultaneously act together and help to improve the photovoltaic properties of the fabricated BHJ cells. Two different blend active polymers viz., (i) rrP3HT:$PC_{61}BM$ and (ii) rrP3HT:$PC_{71}BM$ along with three different hybridized NPs doped HIL namely, (a) PEDOT:PSS + AuNPS:AgNPs (25:75), (b) PEDOT:PSS+ AuNPS:AgNPs (50:50) and (c) PEDOT:PSS+ AuNPs:AgNPs (75:25) were used in this study. The LiF/Al was chosen as conventional cathode contact whereas BPhen and BCP were considered as two different cathode interfacial layers. It was observed that the doping ratio of the two metal NPs in the hole injecting layer have significant effect on the photovoltaic performance of the fabricated plasmonic BHJ solar cell. As the concentration of AgNPs increases in the HIL, the efficiency of all the devices also increases irrespective to the cathode contact. For the HIL (a) PEDOT:PSS + AuNPs:AgNPs (25:75), better device property was observed for all the devices due to the highest absorption capacity of AuNPs:AgNPs (25:75) compared to AuNPs:AgNPs (50:50) and AuNPs:AgNPs (75:25) as shown in Figure. 5.1a. Again the effect of both the dual cathode interfacial layers along with the three NPs modified HILs were nearly identical and it showed significant enhancement in the photovoltaic parameters of the BHJ devices compared to conventional LiF/Al cathode contact. Further, due to the better band energy alignment of BCP/LiF/Al with the active layers compared to BPhen/LiF/Al, BCP/LiF/Al shows better device characteristics compared to BPhen/LiF/Al.

Additionally, the surface roughness of BPhen ($\sigma_{r.m.s.}$~11.47 nm for rrP3HT:$PC_{61}BM$ and ~14.88 nm for rrP3HT:$PC_{71}BM$) upon the rrP3HT:PCBM active layer is higher compared to BCP ($\sigma_{r.m.s.}$~9.76 nm for rrP3HT: $PC_{61}BM$ and ~9.45 nm for rrP3HT:$PC_{71}BM$) (shown as Figure. 4.16 in Chapter 4) and it has been already mentioned in various reports that, in case of organic solar cells, the flow of charges from blend active layer to the cathode contact is resisted by the surface roughness of cathode interfacial layer, as a result of which efficiency decreases.

Figure. 5.5a, Figure. 5.5b and Figure. 5.5c presented schematically the mechanism involved in the collective effect of dual cathode interfacial layer with (a) PEDOT:PSS + AuNPs:AgNPs (25:75), (b) PEDOT:PSS + AuNPs:AgNPs (50:50) and (c) PEDOT:PSS + AuNPs:AgNPs (75:25) respectively. Each of the configurations of the fabricated devices were listed in Table 5.1. In this study, we have fabricated total eighteen different device configurations in which the thickness of the HIL (~40 nm) and the blend polymer (~110 nm) layers were kept similar for all configurations. The thickness of BPhen and BCP were kept ~6 nm upon which LiF (~1 nm)/Al (~100 nm), was deposited. The current density-voltage (J-V) characteristics of all the plasmonic BHJ solar cells are shown in Figure. 5.6.

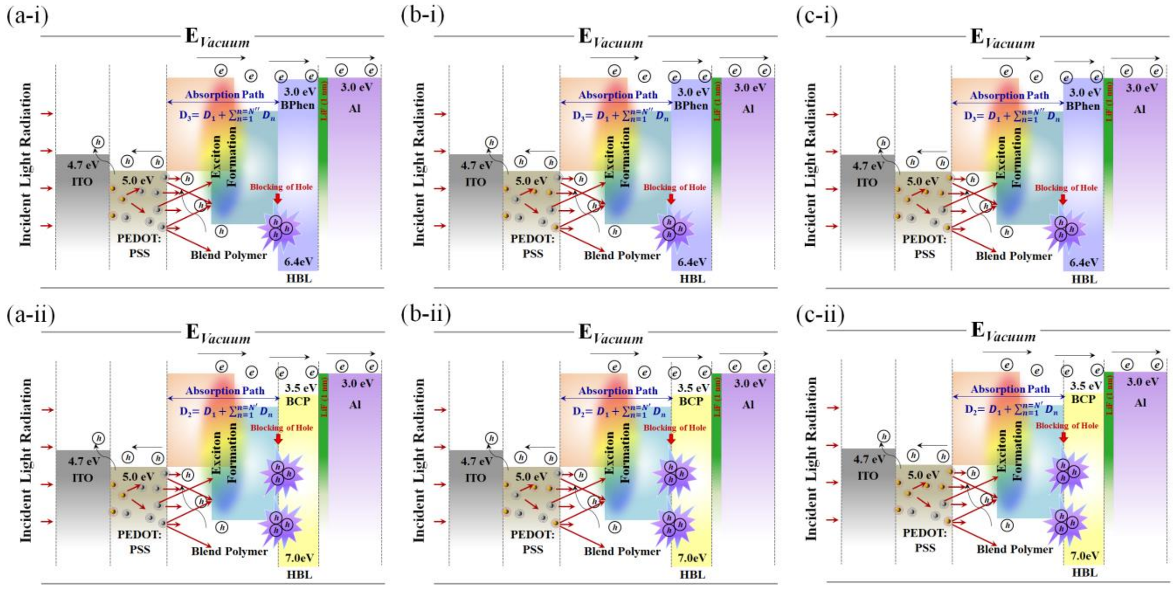

With PEDOT: PSS + AuNPs: AgNPs (25:75) With PEDOT: PSS + AuNPs: AgNPs (50:50) With PEDOT: PSS + AuNPs: AgNPs (75:25)

Figure 5.5. Schematic of the mechanism involved with collective effect of hybrid metal NPs and dual cathode interfacial layers on P3HT:PCBM based BHJ solar cell with (a) PEDOT:PSS + AuNPs: AgNPs (25:75), (b) PEDOT:PSS + AuNPs: AgNPs (50:50)and (c) PEDOT:PSS + AuNPs: AgNPs (75:25) in presence of (i) BPhen/LiF/Al and (ii) BCP/LiF/Al respectively.

With conventional cathode contact (Figure. 5.6 i-a and Figure. 5.6 ii-a), it was observed that with the variation of doping ratio of hybridized NPs, the PCE (η) value can be improved for both the blend polymer systems. For the device having configuration (1) it has been observed that the maximum η=4.03% with J_{sc}=12.87 mA/cm^2, V_{oc}=0.54 V and FF= 58% for rrP3HT:PC$_{61}$BM blend polymer, on the other hand, the maximum η for the device having configuration (10) with rrP3HT:PC$_{71}$BM, was obtained to be 4.89% with J_{sc}=16.19 mA/cm^2, V_{oc}=0.54 V and FF= 56%. A similar characteristic was also noticed when LiF/Al was replaced with BPhen/LiF/Al and BCP/LiF/Al.

Moreover, in the presence of these second cathode interfacial layer and HIL-(a) PEDOT:PSS + AuNPs:AgNPs (25:75) better device performance were observed compared to the HIL-(b) PEDOT:PSS + AuNPs:AgNPs (50:50) and HIL-(c) PEDOT:PSS + AuNPs:AgNPs (75:25) because of the higher surface plasmon effect of the AuNPs:AgNPs (25:75) which enhances the absorption length, scattering and trapping of the incident photon when it travels through the modified HIL (Figure. 5.5b and Figure. 5.5c). Further due to the better band alignment, a reason which is already mention above, BCP/LiF/Al along with HIL-(a) PEDOT:PSS + AuNPs: AgNPs (25:75) displayed better device performance compared to BPhen/LiF/Al for both the blend active layers. Also the selectivity of BCP towards electrons is very high as it has wide band gap (E_g ~3.5 eV) and deeper HOMO level (~ -7 eV) due to which it can block holes and minimize the recombination of charge between the cathode contacts-blend active layer (Figure. 5.5a). For the devices with configurations (4) and (13), the maximum efficiency was observed as η=4.94% with J_{sc}=15.21 mA/cm^2, V_{oc}=0.56 V, FF=58% for rrP3HT:PC$_{61}$BM and η=5.60% with J_{sc}=16.38 mA/cm^2, V_{oc}=0.57 V and FF= 60% for rrP3HT:PC$_{71}$BM [Fig. 5 i-b and ii-b] respectively. Further, from the Figure. 5.6

Table 5.1. Fabricated BHJ device configurations with hybrid metal NPs and dual cathode interfacial layer.

Blend active layer	Cathode Interfacial layer (CIL)	PEDOT:PSS +AuNPs + AgNPs	Device Configuration
(i) rrP3HT: PC$_{61}$BM	(A)LiF/Al	(a) (25:75)	(1) ITO / HIL(a) / Blend Active Layer (i) / CIL (A)
		(b) (50:50)	(2) ITO / HIL(b) / Blend Active Layer (i) / CIL (A)
		(c) (75:25)	(3) ITO / HIL(c) / Blend Active Layer (i) / CIL (A)
	(B)BPhen /LiF/Al	(a) (25:75)	(4) ITO / HIL(a) / Blend Active Layer (i) / CIL (B)
		(b) (50:50)	(5) ITO / HIL(b) / Blend Active Layer (i) / CIL (B)
		(c) (75:25)	(6) ITO / HIL(c) / Blend Active Layer (i) / CIL (B)
	(C)BCP/ LiF/Al	(a) (25:75)	(7) ITO / HIL(a) / Blend Active Layer (i) / CIL (C)
		(b) (50:50)	(8) ITO / HIL(b) / Blend Active Layer (i) / CIL (C)
		(c) (75:25)	(9) ITO / HIL(c) / Blend Active Layer (i) / CIL (C)
(ii) rrP3HT: PC$_{71}$BM	(A)LiF/Al	(a) (25:75)	(10) ITO / HIL(a) / Blend Active Layer (ii) / CIL (A)
		(b) (50:50)	(11) ITO / HIL(b) / Blend Active Layer (ii) / CIL (A)
		(c) (75:25)	(12) ITO / HIL(c) / Blend Active Layer (ii) / CIL (A)
	(B)BPhen /LiF/Al	(a) (25:75)	(13) ITO / HIL(a) / Blend Active Layer (ii) / CIL (B)
		(b) (50:50)	(14) ITO / HIL(b) / Blend Active Layer (ii) / CIL (B)
		(c) (75:25)	(15) ITO / HIL(c) / Blend Active Layer (ii) / CIL (B)
	(C)BCP/ LiF/Al	(a) (25:75)	(16) ITO / HIL(a) / Blend Active Layer (ii) / CIL (C)
		(b) (50:50)	(17) ITO / HIL(b) / Blend Active Layer (ii) / CIL (C)
		(c) (75:25)	(18) ITO / HIL(c) / Blend Active Layer (ii) / CIL (C)

i-c and Figure 5.6 ii-c, it was observed that the devices with configuration (7) and (16), showed the maximum η=5.31% with J_{sc}=14.77 mA/cm², V_{oc}=0.58 V and FF= 62% for rrP3HT:$PC_{61}BM$ and maximum η=5.71% with J_{sc}=16.98 mA/cm², V_{oc}=0.58 V and FF= 58% for rrP3HT:PC71BM respectively.

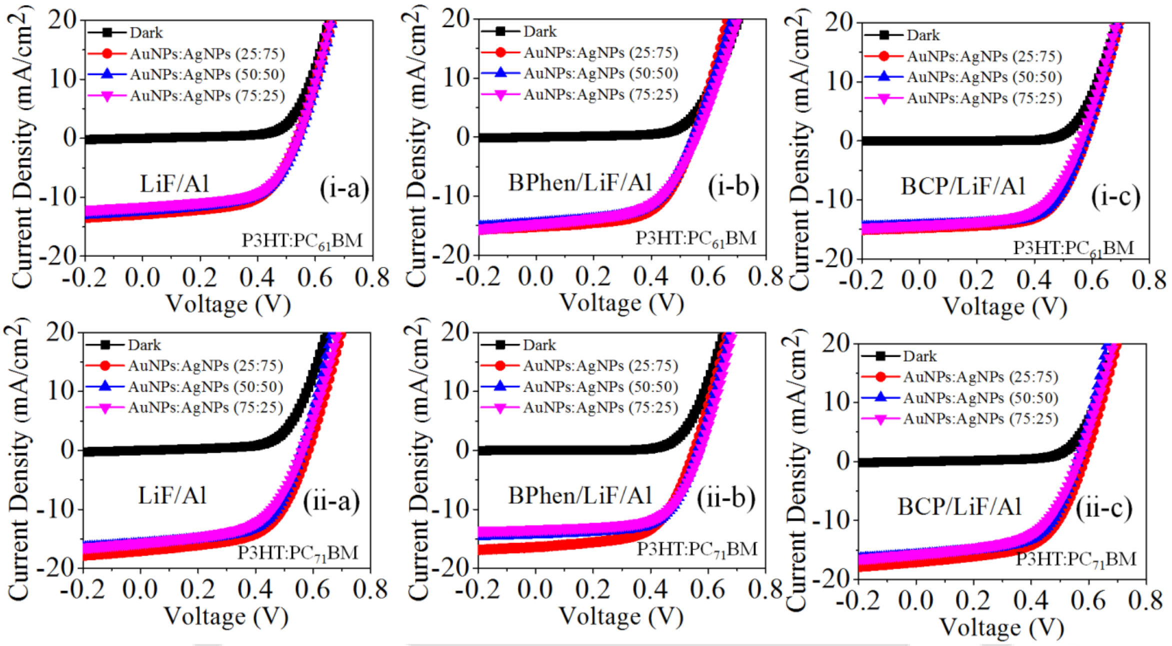

Figure 5.6. J-V characteristics of (i) rrP3HT:$PC_{61}BM$ and (ii) rrP3HT:$PC_{71}BM$ BHJ solar cells with different doping concentration of AuNPs: AgNPs and different (a) LiF/Al, (b) BPhen/LiF/Al and (c) BCP/LiF/Al cathode interfacial layer.

For the devices with configurations (4) and (13), the maximum efficiency was observed as η=4.94% with J_{sc}=15.21 mA/cm², V_{oc}=0.56 V, FF=58% for rrP3HT:$PC_{61}BM$ and η=5.60% with J_{sc}=16.38 mA/cm², V_{oc}=0.57 V and FF= 60% for rrP3HT:$PC_{71}BM$ [Fig. 5 i-b and ii-b] respectively. Further, from the Figure. 5.6 i-c and Figure 5.6 ii-c, it was observed that the devices with configuration (7) and (16), showed the maximum η=5.31% with J_{sc}=14.77mA/cm², V_{oc}=0.58 V and FF=62% for rrP3HT:$PC_{61}BM$ and maximum η=5.71% with J_{sc}=16.98 mA/cm², V_{oc}=0.58 V and FF= 58% for rrP3HT:$PC_{71}BM$ respectively. The device parameters obtained from all the fabricated devices with different configurations, mentioned in Table 5.1, are summarized in Table 5.2. For reference analysis, the devices having bare PEDOT:PSS, PEDOT:PSS + AgNPs and PEDOT:PSS + AuNPs HIL were also fabricated along with conventional and dual cathode interfacial layer. In the first step, with bare PEDOT:PSS and dual cathode interfacial layers the efficiency of rrP3HT:$PC_{61}BM$ increased from 3.30% (LiF/Al) to 4.68% (BCP/LiF/Al) and for rrP3HT:$PC_{71}BM$, 4.04% (LiF/Al) to 4.96% (BCP/LiF/Al) respectively. In the second step similar effect was observed with single NPs doped PEDOT:PSS hole injecting layer. Using the combined effect of PEDOT:PSS + AgNPs and dual cathode interfacial layers, the PCE increased from 3.45% (LiF/Al) to 4.94% (BCP/LiF/Al) for rrP3HT:PC_{61}BM and 4.05% (LiF/Al) to 5.29% (BCP/LiF/Al) for rrP3HT:PC_{71}BM active layers. Similarly, with PEDOT:PSS + AuNPs, the PCE value further increased from 3.96% (LiF/Al) to 4.99% (BCP/LiF/Al) for rrP3HT:PC_{61}BM and 4.66% (LiF/Al) to 5.65% (BCP/LiF/Al) for rrP3HT:PC_{71}BM (shown as Figure. 3.3 in Chapter 3).

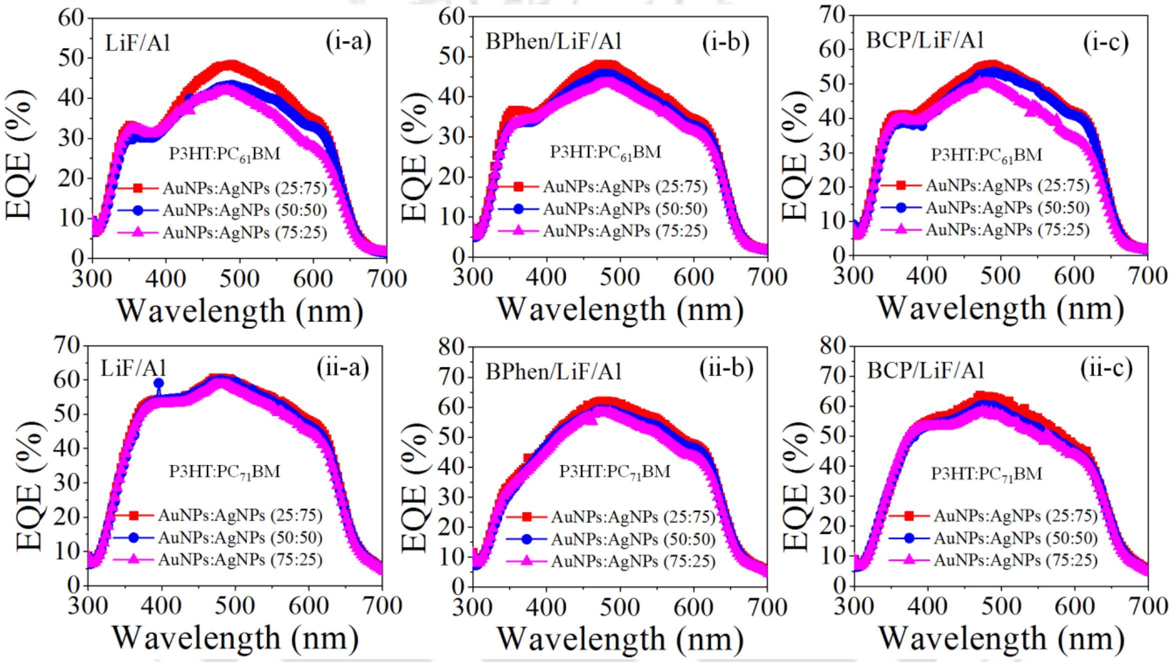

Figure 5.7. External quantum efficiency (EQE) spectre (i) rrP3HT:PC_{61}BM and (ii) rrP3HT:PC_{71}BM BHJ solar cells with different doping concentration of AuNPs: AgNPs and different (a) LiF/Al, (b) BPhen/LiF/Al and (c) BCP/LiF/Al cathode interfacial layer.

Due to the better internal absorbance and scattering properties, the photovoltaic properties of the devices with PEDOT:PSS+ AuNPs were observed higher compared to PEDOT:PSS+ AgNPs as AuNPs has SPR in visible region (~518 nm) and AgNPs has the same near the UV region (~424 nm). Finally to further improve the internal absorbance and scattering phenomena, both the metal nanoparticles were incorporated in the PEDOT:PSS layer together in different doping ratio to observe that with HIL-(a) PEDOT:PSS + AuNPs:AgNPs (25:75) and BCP/LiF/Al the PCE value can be further improved and finally it can be increased from 4.03% (LiF/Al) to 5.31% (BCP/LiF/Al) for rrP3HT:PC_{61}BM and 4.89% (LiF/Al) to 5.71% (BCP/LiF/Al) for rrP3HT:PC_{71}BM. No significant changes were observed in presence of the three metal NP doped HIL in the dark J-V characteristics of all the fabricated devices.

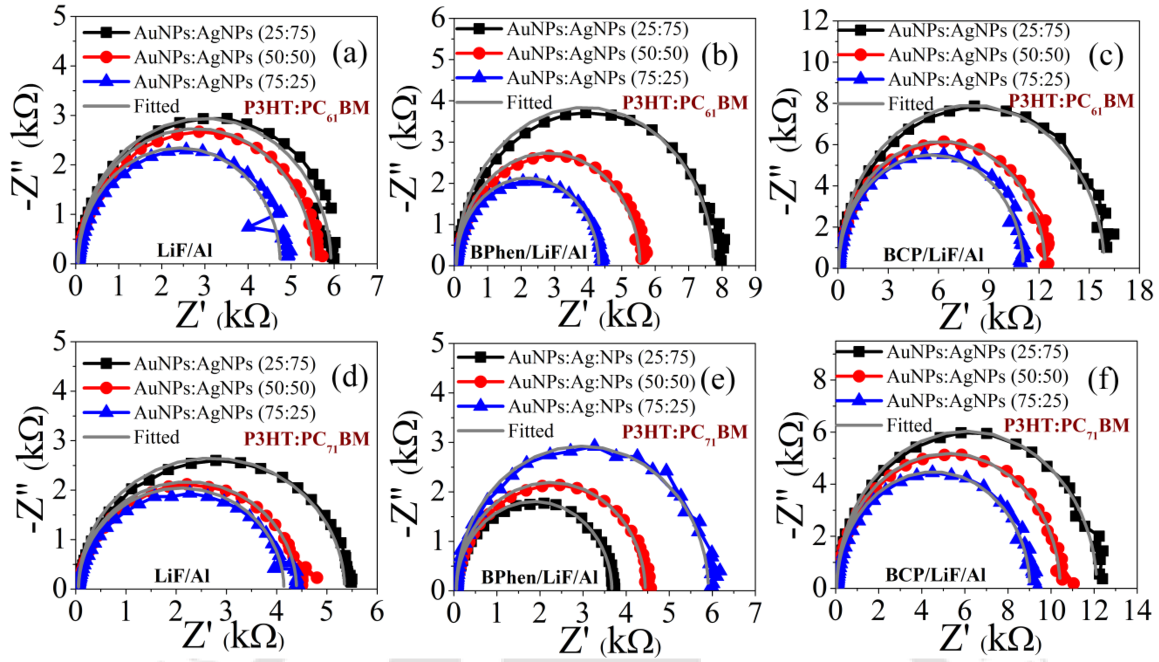

Figure 5.8. Nyquist plots of (i) rrP3HT:PC$_{61}$BM and (ii) rrP3HT:PC$_{71}$BM BHJ solar cells with different doping concentration of AuNPs: AgNPs and different (a) LiF/Al, (b) BPhen/LiF/Al and (c) BCP/LiF/Al cathode buffer layer.

The EQE spectra and Nyquist plots of all the devices are represented in Figure. 5.7 and Figure. 5.8 respectively. The EQE measurements were carried out outside the glove box in ambient atmosphere. From EQE spectra it was noticed that the devices containing BCP as second cathode interfacial layer showed highest quantum efficiency than the other cathode contact in between 300-700 nm wavelength range, with EQE values over ≥ 55% for rrP3HT:PC$_{61}$BM and ≥ 65% for rrP3HT:PC$_{71}$BM for all the metal NPs contained HIL. The J_{sc} value obtained from EQE spectra are also listed in Table 5.2.

To further understand the electron injection in detail, the Nyquist plots was recorded. Generally, the shunt resistance of the device can be estimated from the diameter of the semicircle under its test conditions. It has been observed that the devices with BCP/LiF/Al contact has the largest shunt resistance (shown in Table 5.2) as compared with other device configurations. This observation suggested that due to the high selectivity towards electron of BCP and its high hole blocking capacity, minimize the charge recombination between the blend polymer-cathode contacts. This led to the improvement in the current density and overall photovoltaic performance. Among all the device architectures, the configuration (15), with BPhen/LiF/Al contact, showed higher shunt resistance due to its higher FF and lesser J_{sc} values.

Different approaches are practiced in literature to amend the performance of BHJ solar cells like, various molecular designing and device structure modifications. The modification in cathode contact by inserting functional buffer layer[34-44] and in the hole injecting layer with plasmonic metal NPs are one of the efficient approaches among them.[45-55] The blending of metal NPs in PEDOT:PSS layer is relatively facile and easiest approach. As PEDOT:PSS is soluble in water medium and also the gold and silver NPs can be synthesized through chemical reduction method, these NPs can easily be co-mixed with PEDOT:PSS without further functionalization. Regarding this point, it was observed that incorporation of $NaBH_4$ contained AuNPs in PEDOT:PSS can improve the efficiency of P3HT:PCBM based solar cell up to 3.19% with LiF/Al contact.[43]

Table 5.2 Summary of Photovoltaic performance of all the fabricated plasmonic BHJ solar cell.

Device Configuration	$J_{sc,max}$ (#$J_{sc,avg}$) ($mA.cm^{-2}$)	$J_{sc,EQE}$ ($mA.cm^{-2}$)	R_s ($\Omega.cm^{-2}$)	R_{sh} ($\Omega.cm^{-2}$)	$V_{oc,max}$ (#$V_{oc,avg}$) (V)	FF_{max} (#$FF_{,avg}$) (%)	PCE,η_{max} (#η_{avg}) (%)
(1)	**12.87 (11.98±0.72)**	6.57	134	6357	**0.54 (0.53±0.01)**	**58 (57±01)**	**4.03(3.75±0.21)**
(2)	12.41 (11.69±0.85)	6.07	137	5649	0.54 (0.53±0.02)	56 (55±02)	3.75 (3.54±0.28)
(3)	11.56 (10.71±0.89)	5.66	141	3509	0.54 (0.53±0.02)	58 (57±01)	3.62 (3.35±0.27)
(4)	**15.21 (14.38±0.83)**	6.67	133	7468	**0.56 (0.55±0.01)**	**58 (57±02)**	**4.94 (4.68±0.26)**
(5)	14.68 (13.43±1.25)	6.35	145	5797	0.56 (0.55±0.01)	56 (55±02)	4.60 (4.21±0.39)
(6)	14.65 (13.39±1.26)	6.11	153	4504	0.56 (0.55±0.02)	55 (54±01)	4.51 (4.13±0.38)
(7)	**14.77 (13.89±0.67)**	7.81	127	12097	**0.58 (0.57±0.01)**	**62 (60±01)**	**5.31 (4.99±0.29)**
(8)	14.32 (13.65±0.88)	7.54	128	11503	0.58 (0.55±0.02)	61 (59±01)	5.07 (4.13±0.94)
(9)	15.26 (13.49±1.77)	6.85	135	7880	0.58 (0.56±0.03)	57 (56±02)	4.71 (4.46±0.32)
(10)	**16.19 (15.32±0.75)**	9.05	130	7089	**0.54 (0.53±0.01)**	**56 (55±02)**	**4.89 (4.63±0.22)**
(11)	15.72 (14.97±0.84)	8.89	134	4557	0.54 (0.53±0.02)	56 (55±01)	4.75 (4.53±0.26)
(12)	14.67 (13.83±0.87)	8.65	136	3776	0.54 (0.53±0.02)	57 (56±01)	4.52 (4.26±0.25)
(13)	**16.38 (15.66±0.48)**	8.91	123	6442	**0.57 (0.56±0.01)**	**60 (59±01)**	**5.60 (5.36±0.17)**
(14)	14.29 (13.81±0.72)	8.58	127	11142	0.57 (0.56±0.01)	61 (59±02)	4.97 (4.80±0.24)
(15)	13.37(12.84± 0.60)	8.28	135	12588	0.57 (0.56±0.02)	62 (59±02)	4.73 (4.54±0.19)
(16)	**16.98 (15.93±0.94)**	9.12	117	5561	**0.58 (0.57±0.01)**	**58 (57±01)**	**5.71 (5.36±0.28)**
(17)	15.82 (14.98±1.05)	8.74	125	4545	0.57 (0.56±0.02)	58 (57±02)	5.23 (4.95±0.35)
(18)	15.61 (14.54±1.07)	8.49	136	4395	0.57 (0.56±0.02)	56 (55±01)	4.98 (4.64±0.33)

Average value of ten different devices.

Also additionally, it has been found that the efficiency of BHJ solar cell is vigorously affected by the size of the metal NPs. 50 nm sized AuNPs contained PEDOT:PSS layer can improve the efficiency of the same blend polymer system from 3.57% to 4.24%.[44] Further, the amalgamation of Au-Ag alloy NPs in active layer improved the PCE up to 4.73% with Ca/Al as cathode contact.[49]

In this study, we have successfully amended the PCE value for both the bend active layers through the collective effect of plasmon induced hybrid metal NPs and the dual cathode interfacial layers. Initially, two variants of citrate stabilized gold and silver NPs were discretely synthesized and then physically blended together with three different volume ratios [AuNPs + AgNPs (25:75), AuNPs + AgNPs (50:50) and AuNPs + AgNPs (75:25)]. These three coalesced NPs solution are then co-mixed together in the PEDOT:PSS hole injecting layer to compose three new NPs doped hole injecting layers for the application of organic BHJ solar cell. The plasmonic metal nanoparticles were incorporated in the PEDOT:PSS layer to improve photo current of the fabricated BHJ solar cell by increasing optical absorption and scattering in both the UV and visible wavelength range inside the devices. For dual cathode interfacial layer, two organic small molecules, BPhen and BCP were used along with LiF/Al cathode contact to improve the charge collection. For both the active layers systems the efficiency enhances significantly with PEDOT:PSS + AuNPS:AgNPs (25:75) as HIL and BCP/LiF/Al as cathode contact. Moreover, this study introduced a profoundly facile and very easy technique for high performance rrP3HT:$PC_{61}BM$ and rrP3HT:$PC_{71}BM$ based organic BHJ solar cell with PCE ~6 %, a value which can be further ameliorated by engineering the contrivance architecture and by utilizing preferential additives.

5.3 Conclusion

In conclusion, the cooperative effect of plasmon induced hybrid metal NPs and the dual cathode interfacial layers on rrP3HT:$PC_{61}BM$ and rrP3HT:$PC_{71}BM$ based bulk heterojunction solar cell performance was systematically discussed. Both the citrate stabilized metal NPs were first blended together in three different volume ratio, viz., [AuNPs + AgNPs (25:75), AuNPs + AgNPs (50:50) and AuNPs + AgNPs (75:25)] and then with PEDOT:PSS hole injecting layer. The importance and effect of NPs modified HIL on the device parameters are systematically validated and were compared with each other. It has been found that the PCE increases considerably for both the active blend systems, in presence of PEDOT:PSS + AuNPs:AgNPs (25:75) with BCP/LiF/Al as the modified cathode electrode, because of the better energy level matching of BCP/LiF/Al with the active blend and the excellent surface plasmon property of the AuNPs:AgNPs (25:75) in the UV-visible region compared to AuNPs:AgNPs (50:50) and AuNPs:AgNPs (75:25). The device with ITO/PEDOT:PSS + AuNPs:AgNPs (25:75)/rrP3HT:$PC_{71}BM$/BCP/LiF/Al configuration showed PCE, η= 5.71% with J_{sc}= 16.98 mA/cm^2, V_{oc}= 0.58 V and FF=58%, whereas, for ITO/PEDOT:PSS + AuNPs:AgNPs (25:75)/rrP3HT:$PC_{61}BM$/ BCP/LiF/Al, the device parameters were observed as PCE, η= 5.31% with J_{sc}=14.77 mA/cm^2, V_{oc}= 0.58 V and FF= 62%. These results conclusively explain a very easy method in which the cooperative effect of plasmonic hybrid metals nanoparticles and dual cathode Interfacial layers outstandingly enrich the PCE and on the overall performance of P3HT-PCBM based BHJ solar cells.

5.4 References

1. Christopher, P.; Xin, H., Marimuthu, A.; Linic, S. Singular Characteristics and Unique Chemical Bond Activation Mechanisms of Photocatalytic Reactions on Plasmonic Nanostructures. *Nat. Mater.* **2012**, *11*, 1044–1050.

2. Christopher, P.; Xin, H.; Linic, S. Visible-Light-Enhanced Catalytic Oxidation Reactions on Plasmonic Silver Nanostructures. *Nat. Chem.* **2011**, *3*, 467–472.

3. Linic, S.; Christopher, P.; Ingram, D. B. Plasmonic-Metal Nanostructures for Efficient Conversion of Solar to Chemical Energy. *Nat. Mater.* **2011**, *10*, 911–921.

4. Ravelli, D.; Fagnoni, M.; Albini, A. Photoorganocatalysis. What for? *Chem. Soc. Rev.* **2013**, *42*, 97–113.

5. Lang, X. J.; Chen, X. D.; Zhao, J. C. Heterogeneous Visible Light Photocatalysis for Selective Organic Transformations. *Chem. Soc. Rev.* **2014**, *43*, 473–486.

6. Ma, W. L.; Yang, C. Y.; Gong, X.; Lee, K.; Heeger, A. J. Thermally Stable, Efficient Polymer Solar Cells with Nanoscale Control of the Interpenetrating Network Morphology. *Adv. Funct. Mate*r. **2005**, *15*, 1617–1622.

7. Dennler, G.; Scharber, M. C.; Brabec, C. J. Polymer-Fullerene Bulk-Heterojunction Solar Cells. *Adv. Mater.* **2009**, *21*, 1323–1338.

8. Li, G.; Zhu, R.; Yang, Y. Polymer Solar Cells. *Nat. Photonics* **2012**, ***6***, 153–161.

9. Li, G.; Shrotriya, V.; Huang, J. S.; Yao, Y.; Moriarty, T.; Emery, K.; Yang, Y. High-Efficiency Solution Processable Polymer Photovoltaic Cells by Self-Organization of Polymer Blends. *Nat. Mater.* **2005**, *4*, 864–868.

10. Berson, S.; Bettignies, R. D.; Bailly, S.; Guillerez, S. Poly(3-hexylthiophene) Fibers for Photovoltaic Applications. *Adv. Funct. Mater.* **2007**, ***17***, 1377–1384.

11. Deibel, C.; Dyakonov, V. Polymer–Fullerene Bulk Heterojunction Solar Cells. *Rep. Prog. Phys.* **2010**, *73*, 096401.

12. Blom, P. W. M.; Mihailetchi, V. D.; Koster, L. J. A.; Markov, D. E. Device Physics of Polymer:Fullerene Bulk Heterojunction Solar Cells. *Adv. Mater.* **2007**, *19*, 1551–1566.

13. Su, Y.-W.; Lan, S.-C.; Wei, K.-H. Organic Photovoltaics. *Mater. Today* **2012**, *15*, 554–562.

14. Bouclé, J.; Ravirajan, P.; Nelson, J. Hybrid Polymer–Metal Oxide Thin Films for Photovoltaic Applications. *J. Mater. Chem.* **2007**, *17*, 3141–3153.

15. Banerjee, S.; Pillai, S. C.; Falaras, P.; O'Shea, K. E.; Byrne, J. A.; Dionysiou, D. D. New Insights into the Mechanism of Visible Light Photocatalysis. *J. Phys. Chem. Lett.* 2014, **5**, 2543–2554.

16. Chiu, M.-Y.; Jeng, U.-S.; Su, C.-H.; Liang, K. S.; Wei, K.-H. Simultaneous Use of Small- and Wide-Angle X-ray Techniques to Analyze Nanometerscale Phase Separation in Polymer Heterojunction Solar Cells. *Adv. Mater.* **2008**, *20*, 2573–2578.

17. Schilinsky, P.; Waldauf, C.; Brabec, C. J. Recombination and Loss Analysis in Polythiophene based Bulk Heterojunction Photodetectors. *Appl. Phys. Lett.* **2002**, *81*, 3885–3887.

18. Yuan, K.; Chen, L.; Chen, Y. Optical Engineering of Uniformly Decorated Graphene Oxide Nanoflakes via in Situ Growth of Silver Nanoparticles with Enhanced Plasmonic Resonance. *ACS Appl. Mater. Interfaces*. **2014**, *6*, 21069–21077.

19. Yuan, K.; Chen, L.; Chen, Y. Versatile Electron-Collecting Interfacial Layer by in Situ Growth of Silver Nanoparticles in Nonconjugated Polyelectrolyte Aqueous Solution for Polymer Solar Cells. *J. Phys. Chem. B* **2014**, *118*, 11563–11572.

20. Street, R. A.; Schoendorf, M.; Roy, A.; Lee, J. H. Interface State Recombination in Organic Solar Cells. *Phys. Rev. B* **2010**, *81*, 205307.

21. Jung, K.; Song, H. -J.; Lee, G.; Ko, Y.; Ahn, K.; Choi, H.; Kim, J. Y.; Ha, K.; Song, J.; Lee, J.-K.; Lee, C.; Choi, M. Plasmonic Organic Solar Cells Employing Nanobump Assembly via Aerosol-Derived Nanoparticles. *ACS Nano* **2014**, *8*, 2590–2601.

22. Chiu, M.-Y.; Jeng, U.-S.; Su, M.-S.; Wei, K.-H. Morphologies of Self-Organizing Regioregular Conjugated Polymer/Fullerene Aggregates in Thin Film Solar Cells *Macromolecules* 2010, **43**, 428–432.

23. Liu, C.-M.; Chen, C.-M.; Su, Y.-W.; Wang, S.-M.; Wei, K.-H. The Dual Localized Surface Plasmonic Effects of Gold Nanodots and Gold Nanoparticles Enhance the Performance of Bulk Heterojunction Polymer Solar Cells. *Org. Electron.* **2013**, *14*, 2476–2483.

24. Ting, H.; Longbin, L.; Shuqin, X.; Kai, Y.; Hanjun, Y.; Chen ,L.; Chen, Y. In Situ Implanting Carbon Nanotube-Gold Nanoparticles into ZnO as Efficient Nanohybrid Cathode Buffer Layer for Polymer Solar Cells. *Org. Electron.* 2016, **38**, 350–356.

25. Liu, H.; Wu, H.; Luo, Z.; Shen, J.; Kang, G.; Liu, B.; Wan, Z.; Jiang, J. Regioselectivity-Reversed Asymmetric Aldol Reaction of 1,3-Dicarbonyl Compounds *Chem. Eur. J.* **2015**, *21*, 11899–11903.

26. Fung, D. D. S.; Qiao, L. F.; Choy, W. C. H.; Wang, C.; Sha, W. E. I.; Xie, F.; He, S. Optical and Electrical Properties of Efficiency Enhanced Polymer Solar Cells with Au Nanoparticles in a PEDOT:PSS Layer. *J. Mater. Chem.* **2011**, *21*, 16349–16356.

27. Theander, M.; Yartsev, A.; Zigmantas, D.; Sundström, V.; Mammo, W.; Andersson, M. R.; Inganäs, O. Photoluminescence Quenching at a Polythiophene/C_{60} Heterojunction. *Phys. Rev. B* **2000**, *61*, 12957–12963.

28. Kirchartz, T.; Agostinelli, T.; Campoy-Quiles, M.; Gong, W.; Nelson, J. Understanding the Thickness-Dependent Performance of Organic Bulk Heterojunction Solar Cells: The Influence of Mobility, Lifetime, and Space Charge. *J. Phys. Chem. Lett.* **2012**, ***3***, 3470–3475.

29. Halls, J. J. M.; Pichler, K.; Friend, R. H.; Moratti, S. C.; Holmes, A. B. Exciton Diffusion and Dissociation in a Poly(p-Phenylenevinylene)/C_{60} Heterojunction Photovoltaic Cell. *Appl. Phys. Lett.* **1996**, ***68***, 3120–3122.

30. Catchpole, K. R.; Polman, A. Design Principles for Particle Plasmon Enhanced Solar Cells. *Appl. Phys. Lett.* **2008**, *93*, 191113.

31. Barnes, W. L.; Dereux, A.; Ebbesen, T. W. Surface Plasmon Subwavelength Optics *Nature* **2003**, ***424***, 824–830.

32. Hutter, E.; Fendler, J. H. Exploitation of Localized Surface Plasmon Resonance *Adv.Mater.* **2004**, *16*, 1685–1706.

33. Kelly, K. L.; Coronado, E.; Zhao, L. L.; Schatz, G. C. The Optical Properties of Metal Nanoparticles: The Influence of Size, Shape, and Dielectric Environment. *J. Phys. Chem. B* **2003**, *107*, 668–677.

34. Pandey, R.; Holmes, R. J. Graded Donor-Acceptor Heterojunctions for Efficient Organic Photovoltaic Cells. *Adv. Mater.* **2010**, ***22***, 5301–5305.

35. Hoven, C. V.; Dang, X.-D.; Coffin, R. C.; Peet, J.; Nguyen, T.-Q.; Bazan, G. C. Improved Performance of Polymer Bulk Heterojunction Solar Cells Through the Reduction of Phase Separation via Solvent Additives. *Adv. Mater.* **2010**, *22*, E63–E66.

36. Brabec, C. J.; Shaheen, S. E.; Winder, C.; Sariciftci N. S.; Denk, P. Effect of LiF/Metal Electrodes on the Performance of Plastic Solar Cells. *Appl. Phys. Lett.* **2002**, *80*, 1288–1290.

37. Hill, I. G.; Rajagopal, A.; Kahn, A.; Hu, Y. Molecular Level Alignment at Organic Semiconductor-Metal Interfaces. *Appl. Phys. Lett.* **1998**, *73*, 662–664.

38. Singh, A.; Dey, A.; Das, D.; Iyer, P. K. Effect of Dual Cathode Buffer Layer on the Charge Carrier Dynamics of rrP3HT:PCBM Based Bulk Heterojunction Solar Cell. *ACS Appl. Mater. Interfaces* **2016**, *8*, 10904–10910.

39. Namkoong, G.; Kong, J.; Samson, M.; Hwang, I. W.; Lee, K. Active Layer Thickness Effect on the Recombination Process of PCDTBT:$PC_{71}BM$ Organic Solar Cells. *Org. Electron.,* 2013, **14**, 74–79.

40. Wong, W.-Y.; Wang, X.-Z.; He, Z.; Djurisic, A. B.; Yip, C.-T.; Cheung, K.-Y.; Wang, H.; Mak, C. S. K.; Chan, W.-K. Metallated Conjugated Polymers as a New Avenue towards High-Efficiency Polymer Solar Cells *Nat. Mater.* **2007**, *6*, 521–527.

41. Reinspach, J. A.; Diao, Y.; Giri, G.; Sachse, T.; England, K.; Zhou, Y.; Tassone, C.; Worfolk, B. J.; Presselt, M.; Toney, M. F.; Mannsfeld, S.; Bao, Z. Tuning the

Morphology of Solution-Sheared P3HT:PCBM Films. *ACS Appl. Mater. Interfaces* **2016**, *8*, 1742–1751.

42. Shao, M.; Keum, J.; Chen, J.; He, Y.; Chen, W.; Browning, J. F.; Jakowski, J.; Sumpter, B. G.; Ivanov I. N.; Ma, Y.-Z.; Rouleau, C. M.; Smith, S. C.; Geohegan, D. B.; Hong, K.; Xiao, K. The Isotopic Effects of Deuteration on Optoelectronic Properties of Conducting Polymers. *Nat. Commun.* **2014**, *5*, 4180.

43. Guo, S.; Ruderer, M. A.; Rawolle, M.; Körstgens, V.; Birkenstock, C.; Perlich, J.; Müller-Buschbaum, P. Evolution of Lateral Structures during the Functional Stack Build-up of P3HT:PCBM-Based Bulk Heterojunction Solar Cells. *ACS Appl. Mater. Interfaces* **2013**, ***5***, 8581–8590.

44. Müller-Buschbaum, P. The Active Layer Morphology of Organic Solar Cells Probed with Grazing Incidence Scattering Techniques. *Adv. Mater.* **2014**, *16*, 7692–7709.

45. Notarianni, M.; Vernon, K.; Chou, A.; Aljada, M.; Liu, J. Z.; Motta, N. Plasmonic Effect of Gold Nanoparticles in Organic Solar Cells. *Sol. Energy* **2014**, *106*, 23–37.

46. Luber, E. J.; Buriak, J. M. Reporting Performance in Organic Photovoltaic Devices. *ACS Nano* **2013**, *7*, 4708–4714.

47. Zimmermann, E.; Ehrenreich, P.; Pfadler, T.; Dorman, J. A.; Weickert, J.; Schmidt-Mende, L. Erroneous Efficiency Reports Harm Organic Solar Cell Research. *Nat. Photonics* **2014**, *8*, 669–672.

48. Wang, T.; Chen, C.; Guo, K.; Chen, G.; Xu, T.; Wei, B. Improved Performance of Polymer Solar Cells by using Inorganic, Organic, and Doped Cathode Buffer Layers. *Chin. Phys. B* **2016**, *25,* 038402.

49. Oh, I. S.; Ji, C. H.; Oh, S. Y. Effects of Ytterbium on Electrical and Optical Properties of BCP/Ag/WO_3 Transparent Electrode Based Organic Photovoltaic Cells *Electron. Mater. Lett.* **2016**, *12*, 156–162.

50. Kim, J.-H.; Park, J.-G. Effect of a Co-evaporated Alq_3:Liq Cathode Buffer Layer on the Performance of a Polymer Photovoltaic Cell. *J. Korean. Phys. Soc.* 2015, **66**, 1872–1878.

51. Chang, C.-C.; Lin, C.-F.; Chiou, J.-M.; Ho, T.-H.; Tai, Y.; Lee, J.-H.; Chen, Y.-F.; Wang, J.-K.; Chen, L.-C.; Chen, K.-H. Effects of Cathode Buffer Layers on the Efficiency of Bulk-Heterojunction Solar Cells. *Appl. Phys. Lett.* **2010**, *96,* 263506.

52. Jung, G. H.; Lee, J.-L. Origin of Gap States in the Electron Transport Layer of Organic Solar Cells. *J. Mater. Chem. A* **2013**, ***1***, 3034–3039.

53. Wu, J. L.; Chen, F. C.; Hsiao, Y. S.; Chien, F. C.; Chen, P. L.; Kuo, C. H.; Huang, M. H.; Hsu, C. S. Surface Plasmonic Effects of Metallic Nanoparticles on the Performance of Polymer Bulk Heterojunction Solar Cells. *ACS Nano* 2011**,** **5**, 959–967.

54. Chen, F. C.; Wu, J. L.; Lee, C. L.; Hong, Y.; Kuo, C. H.; Huang, M. H. Plasmonic-Enhanced Polymer Photovoltaic Devices Incorporating Solution Processable Metal Nanoparticles. *Appl. Phys. Lett.* **2009**, *95*, 013305.

55. Li, X. H.; Choy, W. C. H.; Lu, H. F.; Sha, W. E. I.; Ho, A. H. P. Efficiency Enhancement of Organic Solar Cells by using Shape-Dependent Broadband Plasmonic Absorption in Metallic Nanoparticles. *Adv. Funct. Mater.* **2013**, *23*, 2728–2735.

Chapter 6

Influence of Different Shaped Plasmonic AuNPs and Double Cathode Interfacial Layers on PCE of Organic BHJ Solar Cell

Over the last two decades, a magnetizing interest can be observed for rectifying the performance of third generation- organic bulk hetero junction (BHJ) solar cell because of its capability to obtain more expeditious, lightweight, economical contrivances compared to the conventional first generation silicon wafer and second generation-CdTe, and CIGS predicated thin film solar cell technologies. However, their conversion efficiency is still not commensurable to their silicon counterparts. The efficiency of organic BHJ solar cell essentially depends upon two factors- (1) the photo-absorption capacity of the blend active materials, and (2) the photo-generated charge collection ability of the contacts material.

There are already several approaches mentioned in the literature to improve the photovoltaic properties by reducing these problems. For improving the point (1), the most commonly used techniques are the inclusion of periodic nanostructures, diffraction gratings, plasmonic excitation using metallic nanoparticles (NPs) and a combination of gratings and metallic nanoparticles.[1-4] Trapping of light by the inducing plasmonic metal NPs in the various layers of BHJ solar cell was found to be useful for better photo absorption in organic BHJ solar cells.[5-8] A surface plasmon is a phenomenon where bound excitation is generated on noble metal surface when incident photon interacted with the free conduction electrons of the metal surface. After excitation, surface plasmon decay either by radiatively or non-radiatively, follow-on absorption or scattering of light respectively, as result of which internal absorption path length increases. Additionally, metallic nanoparticles also affect the exciton generation rate, dissociation and extraction of photo-generated charges inside the organic BHJ solar cell. One of the main advantage metallic nanoparticles is that it does not compromise the structure of the BHJ solar cell since they can be easily mixed up in any one layers of the device. Further it has been found that different shapes and sizes of the metallic nanoparticles also has great influence on the improving the power conversion efficiency of BHJ solar cell as the plasmonic property of any metallic NPs directly depends on its dimensionality. Further, in order to impromise point (2), the interfacial layers of the contact materials also show very important significance for increasing the efficiency of BHJ solar cell by modifying the contact work function and thereby improving the particular charge carrier selectivity.[9-16]

This study try to demonstrate the combined influence of different shaped plasmonic gold nanoparticles (AuNPs) and the double cathode interfacial layer on improving the power conversion efficiency (PCE) of rrP3HT:PCBM based Bulk Hetero Junction (BHJ) solar cell. Two different blend polymers, namely, rrP3HT:PC$_{61}$BM and rrP3HT:PC$_{71}$BM along with BPhen and BCP as the buffer layers of the convensional LiF/Al cathode contact were used here in order to demostrate the effects. Initially, four different types AuNPs, viz. CTAB capped gold nanorod (AuNRs), gold nanosphere (AuNSs), gold nano-oval (AuNOs) and gold nano branch (AuNBs) were synthesized separately and then blend with PEDOT:PSS hole transport layer to form four newly doped hole injecting layers and their effect on improving the power conversion efficiency (PCE) of rrP3HT:PCBM based BHJ solar cell was systamatically analysed. It has been found that for both the blend systems the PCE increases appreciably in presence of PEDOT:PSS + AuNRs with BCP/LiF/Al as the cathode contact compared to others because the superior surface plasmon resonance of the AuNRs at the UV-visible spectrum compared to AuNSs, AuNOs and AuNBs and the better band alignment of BCP/LiF/Al with the active layers. and The device with ITO/ PEDOT:PSS + AuNRs/rrP3HT:PC$_{71}$BM/BCP/LiF/Al configuration showed the highest PCE, η= 5.83 % with J_{sc}= 15.80 mA/cm^2, V_{oc}= 0.58 V and FF=63%, whereas, for ITO/ PEDOT:PSS + AuNRs/rrP3HT:PC$_{61}$BM/BCP/LiF/Al, the device parameters were observed as PCE, η= 5.44 % with J_{sc}=17.40 mA/cm^2, V_{oc}= 0.57 V and FF= 57%. To the best of our knowledge, these result are one of the highest reported value on rrP3HT:PCBM based organic BHJ system and the results can successively explain the influence of shape of AuNPs to magnify the PCE value of rrP3HT:PCBM based BHJ solar cells in presence of double cathode interfacial layer.

6.1 Experiments

6.1.1 Synthesis of Different Shaped AuNPs

For the synthesis of different shaped AuNPs, gold (III) chloride trihydrate ($HAuCl_4 \cdot 3H_2O$), sodium borohydride ($NaBH_4$), silver nitrate ($AgNO_3$), cetyltrimethylammonium bromide (CTAB) and ascorbic acid were purchased from Sigma-Aldrich and used without any modification. Tri-sodium citrate 2-hydrate was purchased from Merck Specialties Pvt Ltd and de-ionized water was used in all the preparations. Seed-mediated method was used for the synthesis of four different shapes Gold nanoparticles viz., including nano-spheres, nano-ovals, nano-branches and nano-rods. Three different types of gold seed were prepared for synthesizing four different shaped AuNPs, the detail of which are given below-

Seed 1: Seed 1 was prepared in presence of cetyltrimethylammonium bromide (CTAB) as stabilizing agent. For the preparation of CTAB-stabilized Seed freshly prepared, ice-cold aqueous $NaBH_4$ solution (0.01 M, 0.3 mL) was added into an aqueous mixture solution composed of $HAuCl_4$ (0.01 M, 0.125 mL) and CTAB (0.1 M, 3.75 mL), followed by rapid inversion mixing for 2 min. The resulting seed solution was kept at room temperature for 2 h before use.

Seed 2: Seed 2 was prepared in presence of cetyltrimethylammonium bromide (CTAB) as stabilizing agent for gold nanorod preparation. In this method, the seed solution was prepared by the addition of $HAuCl_4$ (0.01 M, 0.25 mL) into CTAB (0.1 M, 10 mL) in a 15mL plastic tube with gentle mixing. A freshly prepared, ice-cold $NaBH_4$ solution (0.01 M, 0.6 mL) was then injected quickly into the mixture solution, followed by rapid inversion for 2 min. The seed solution was kept at room temperature for 2 h before use.

Seed 3: Seed 3 was prepared in presence of tri-sodium citrate 2-hydrate as stabilizing agent. For the preparation of citrate-stabilized seeds, aqueous solutions of $HAuCl_4$ (0.01 M, 0.125 mL) and citrate (0.01 M, 0.25 mL) were added into water (9.625 mL), and then a freshly prepared, ice-cold aqueous $NaBH_4$ solution (0.01 M, 0.15 mL) was added under vigorous stirring. The resulting seed solution was kept at room temperature for at least 2 h before use.

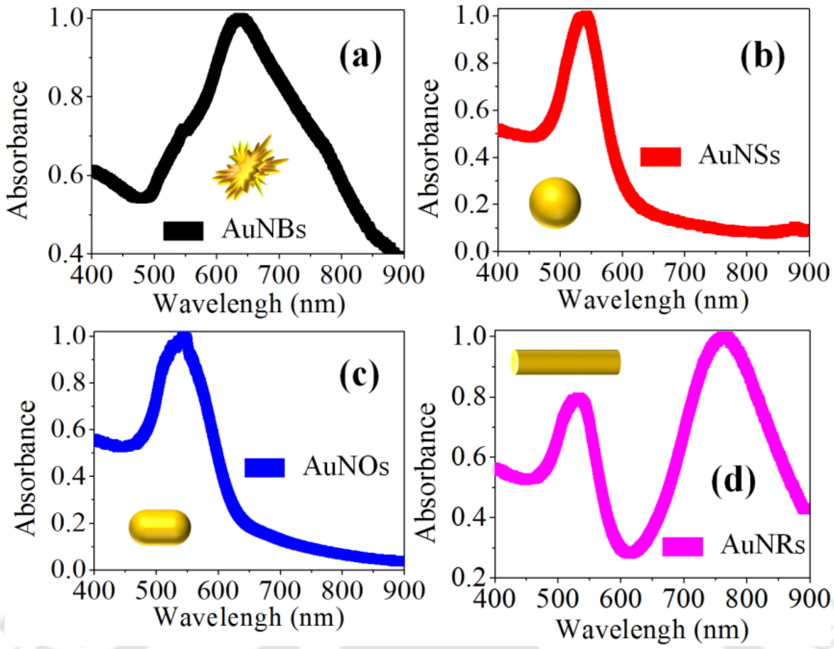

Figure 6.1. UV-Vis absorption study of the synthesized (a) AuNBs (b) AuNSs (c) AuNOs and (b) AuNRs respectively.

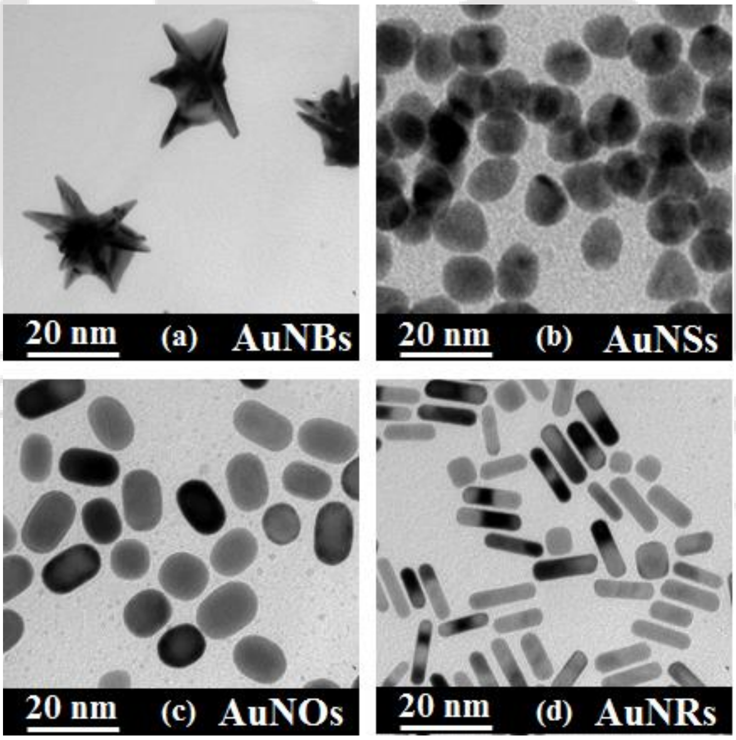

Figure 6.2. TEM images of the synthesized (a) AuNBs (b) AuNSs (c) AuNOs and (b) AuNRs respectively.

Synthesis of Gold Nano-sphere (AuNSs): The AuNSs was prepared by the sequential addition of CTAB (0.1 M, 6.4 mL), $HAuCl_4$ (0.01 M, 0.8 mL) and ascorbic acid (0.1 M, 3.8 mL) into water (32 mL). 20 μL of the seed 1 solution diluted 10 times with water was then added into the growth solution. The resulting solution was mixed by gentle inversion for 10 s and then left undisturbed overnight.

Synthesis of Gold Nano-branch (AuNBs): Gold nano-branches were grown with citrate-stabilized Au nanoparticles as seeds (seed 3). The growth solution of Au Nano-branches was prepared by the sequential addition of $HAuCl_4$ (0.01 M, 1.8 mL), $AgNO_3$ (0.01 M, 0.27 mL), and ascorbic acid (0.1 M, 0.3 mL) into an aqueous CTAB solution (0.1 M, 42.75 mL). The seed 3 solution (40 μL) was then added. The entire reaction solution was mixed by gentle inversion for 10 s and then left undisturbed overnight.

Synthesis of Gold Nano-oval (AuNOs) and Gold Nano-rod (AuNRs): AuNOs and AuNRs were synthesized by similar method only the amount of $AgNO_3$ was varied. For the synthesis of AuNRs, $HAuCl_4$ (0.01 M, 2.0 mL) and $AgNO_3$ (0.01 M, 0.4 mL) were mixed with CTAB (0.1 M, 40 mL) in a 50 mL plastic tube whereas for AuNOs the amount of $AgNO_3$ was decreases to 0.01mL. HCl (1.0 M, 0.8 mL) was then added separately to this two solutions to adjust the pH of the solution to 1-2, followed by the addition of ascorbic acid (0.1 M, 0.32 mL). Finally, the seed 2 solution (0.096 mL) was injected into the growth solutions. The solutions were then gently mixed for 10 s and left undisturbed overnight. After 24 hours of synthesis, all the NPs solutions (2 mL) were washed with de-ionized water by centrifuged it in 15000 rpm for 5 min. The precipitates were then re-dispersed into water (2 mL), centrifuged again at 15000 rpm for 5 min, and finally again re-dispersed into de-ionized water (2 mL each) before recording the TEM and UV-vis spectra of the NPs. The recorded UV-Vis Spectra and the TEM images of each of the NPs are shown in Figure. 6.1 and Figure.6.2 respectively. The observed UV-Vis plasmonic peaks of AuNBs, AuNSs, AuNOs and AuNRs were observed at 636 nm, 541 nm, 543 nm and (532 nm, 762 nm) respectively [Figure. 6.1] and their corresponding average sizes were observed as ~20 nm for AuNBs, 10 nm for AuNSs, 15 nm for AuNOs and 18 nm for AuNRs respectively [Figure. 6.2].

6.1.2 Thin Film Morphology Study

The plasmonic BHJ solar cells were fabricated on commercially available ITO-coated glass substrate (R_{Sheet}~15Ω/sq., Sigma Aldrich, India) and the schematic representation of all the device structures are shown in Figure.6.3. All the devices were fabricated following the same method as like Chapter 5. Prior to the device fabrication the effect of four different shaped AuNPs on the morphology of the active layer surface were analysed by Grazing Incidence Small Angle X-ray Scattering (GISAXS) study.[17-22]

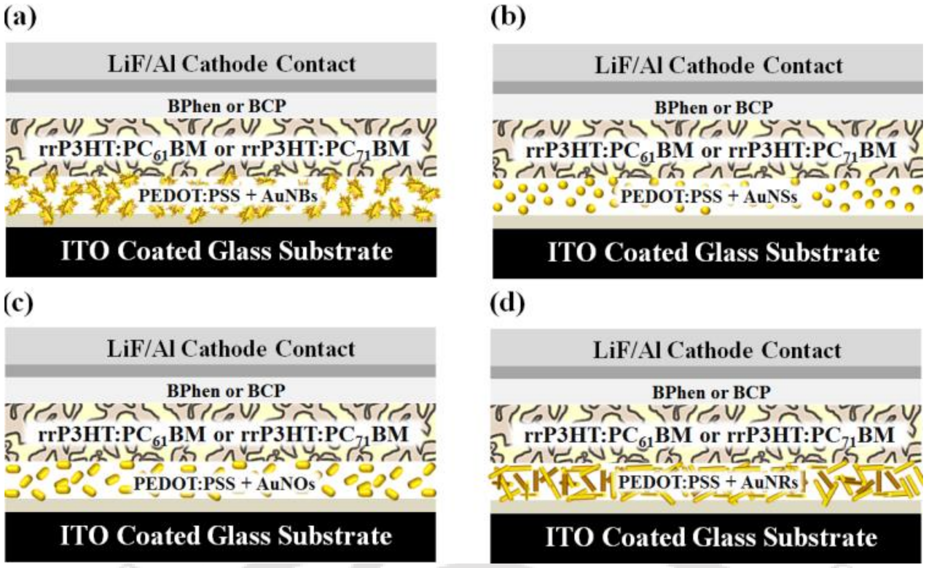

Figure 6.3. Schematic of the fabricated plasmonic bulk hetero junction solar cell with (b) PEDOT:PSS + AuNBs (c) PEDOT:PSS + AuNSs (d) PEDOT:PSS + AuNOs and (e) PEDOT:PSS + AuNRs as HIL respectively.

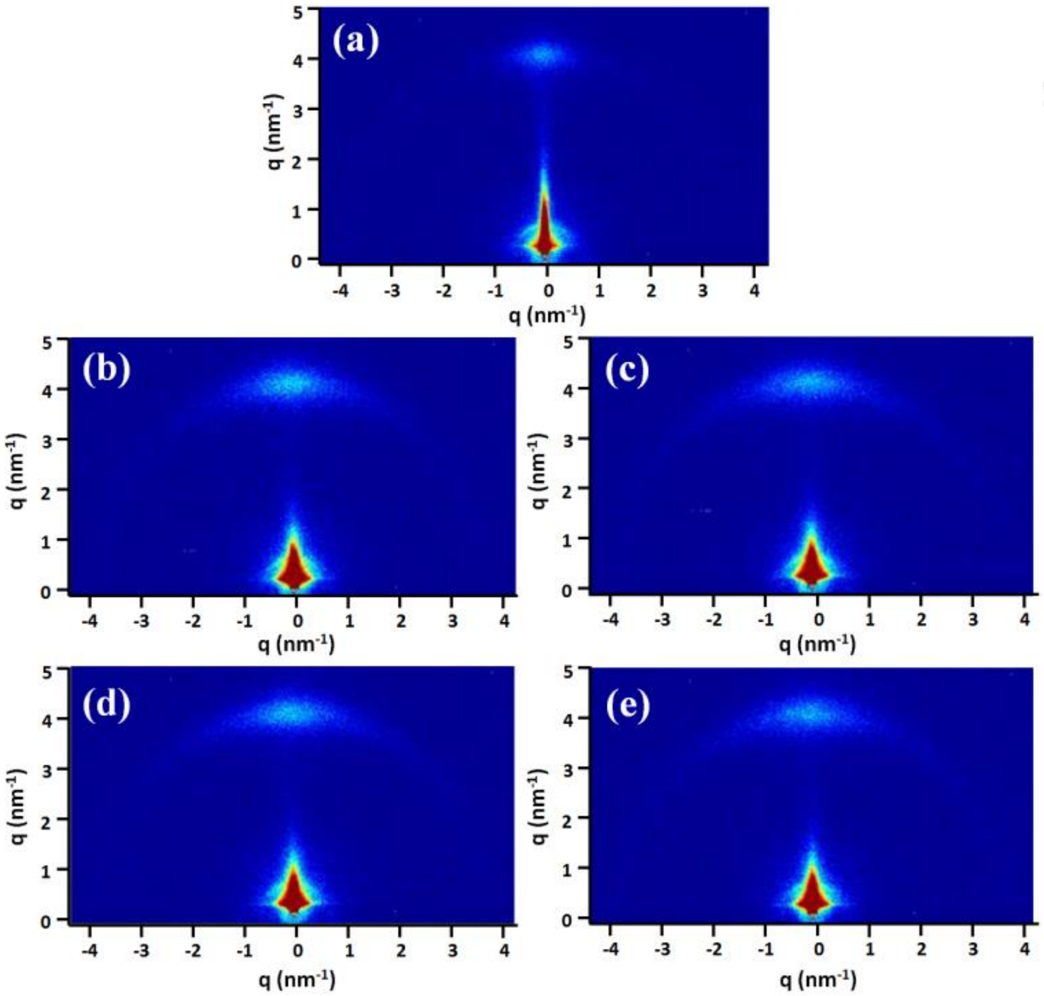

Figure 6.4. GISAXS images rrP3HT:PC$_{71}$BM blend polymer on (a) Bare PEDOT:PSS (b) PEDOT:PSS + AuNBs (c) PEDOT:PSS + AuNSs (d) PEDOT:PSS + AuNOs and (e) PEDOT:PSS + AuNRs respectively.

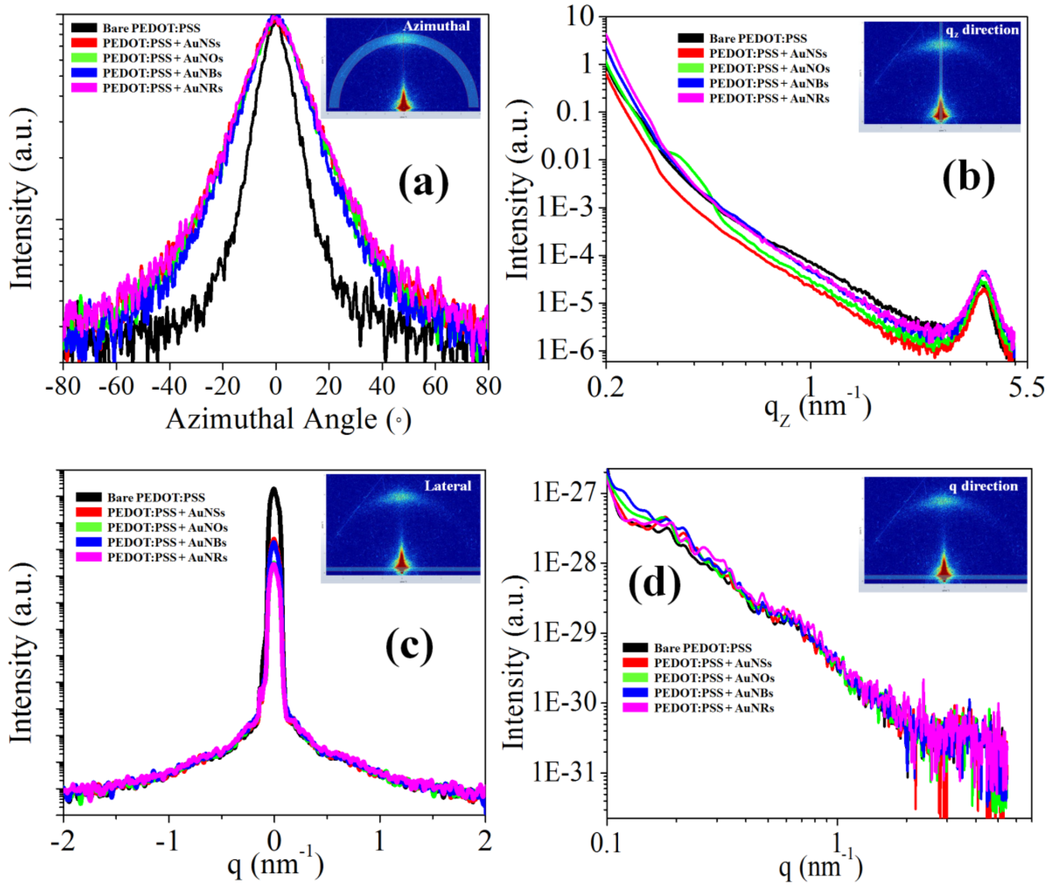

Figure 6.5. Correlation peak of GISAXS images. (a) azimuthal integration (b) correlation peak in q_z direction (c) correlation peak in lateral direction and (d) Yoneda cuts along lateral direction.

For this study, the synthesized four different types of AuNPs were blended with Poly (3, 4-ethylenedioxythiophene) -poly(styrene sulfonate) (PEDOT:PSS, Sigma Aldrich, India), hole injecting layer with a doping concentration of 20% (v/v), to make four different types of NPs doped new HIL. Following this, the four different HIL were spun on the ITO coated substrates at 3000 rpm and dried at 120°C for 30 minutes. The measurements were carried out by SAXSpoint 2.0 system (Anton Paar) having Dectris Eiger detector with photon energy of 40 kV, sample–detector distance of 315 mm and a grazing incidence angle of 0.2°. The 2D q-plots of the GISAXS measurements are shown Figure. 6.4. It is observed that all the different shaped AuNPs doped PEDOT:PSS containing samples (Figure. 6.4b to Figure. 6.4e) are very much alike with each other whereas the sample with bare PEDOT:PSS is showing a distinct scattering pattern (Figure. 6.4a). A correlation peak is visible for all the samples indicating a slightly distorted layered structure. To analyse this, the azimuthal integration along the correlation peak are plotted which is shown in Figure. 6.5 which shows that the sample with bare PEDOT: PSS exhibits a narrower peak while with all the AuNPs modified

PEDOT: PSS contained samples are exhibits a comparable broadness which indicates that the presence of AuNPs leads to a slight disorder in the active layer system. There were total sixteen different device architectures were fabricated in order to analyse this dual effect which are listed below in the Table 6.1.

Table 6.1. Fabricated BHJ device configurations with different shaped AuNPs and double cathode interfacial layer.

Blend active layer	Cathode Interfacial layer (CIL)	HIL	Device Configuration
(i) rrP3HT: $PC_{61}BM$	(A)BPhen/LiF/Al	(a) PEDOT:PSS +AuNBs	(1) ITO / HIL(a) / Blend Active Layer (i) / CIL (A)
		(b) PEDOT:PSS +AuNSs	(2) ITO / HIL(b) / Blend Active Layer (i) / CIL (A)
		(c) PEDOT:PSS +AuNOs	(3) ITO / HIL(c) / Blend Active Layer (i) / CIL (A)
		(d) PEDOT:PSS +AuNRs	(4) ITO / HIL(d) / Blend Active Layer (i) / CIL (A)
	(B)BCP/LiF/Al	(a) PEDOT:PSS +AuNBs	(5) ITO / HIL(a) / Blend Active Layer (i) / CIL (B)
		(b) PEDOT:PSS +AuNSs	(6) ITO / HIL(b) / Blend Active Layer (i) / CIL (B)
		(c) PEDOT:PSS +AuNOs	(7) ITO / HIL(c) / Blend Active Layer (i) / CIL (B)
		(d) PEDOT:PSS +AuNRs	(8) ITO / HIL(d) / Blend Active Layer (i) / CIL (B)
(ii) rrP3HT: $PC_{71}BM$	(A)BPhen/LiF/Al	(a) PEDOT:PSS +AuNBs	(9) ITO / HIL(a) / Blend Active Layer (ii) / CIL (A)
		(b) PEDOT:PSS +AuNSs	(10) ITO / HIL(b) / Blend Active Layer (ii) / CIL (A)
		(c) PEDOT:PSS +AuNOs	(11) ITO / HIL(c) / Blend Active Layer (ii) / CIL (A)
		(d) PEDOT:PSS +AuNRs	(12) ITO / HIL(d) / Blend Active Layer (ii) / CIL (A)
	(B)BCP/LiF/Al	(a) PEDOT:PSS +AuNBs	(13) ITO / HIL(a) / Blend Active Layer (ii) / CIL (B)
		(b) PEDOT:PSS +AuNSs	(14) ITO / HIL(b) / Blend Active Layer (ii) / CIL (B)
		(c) PEDOT:PSS +AuNOs	(15) ITO / HIL(c) / Blend Active Layer (ii) / CIL (B)
		(d) PEDOT:PSS +AuNRs	(16) ITO / HIL(d) / Blend Active Layer (iI) / CIL (B)

6.2 Results and Discussion

6.2.1 Photovoltaic Characterization

The schematic of the mechanism involved in the fabricated rrP3HT:$PC_{71}BM$ based plasmonic solar cell, containing four different shaped AuNPs doped hole injecting layers with double cathode interfacial layer are represented in Figure. 6.6 to Figure. 6.9. In this study, two different physical phenomenon, i.e., (1) the plasmonic effect of different shaped AuNPs and (2) the influence of double cathode interfacial layers, are simultaneously acting together and helping to improve the photovoltaic properties of the

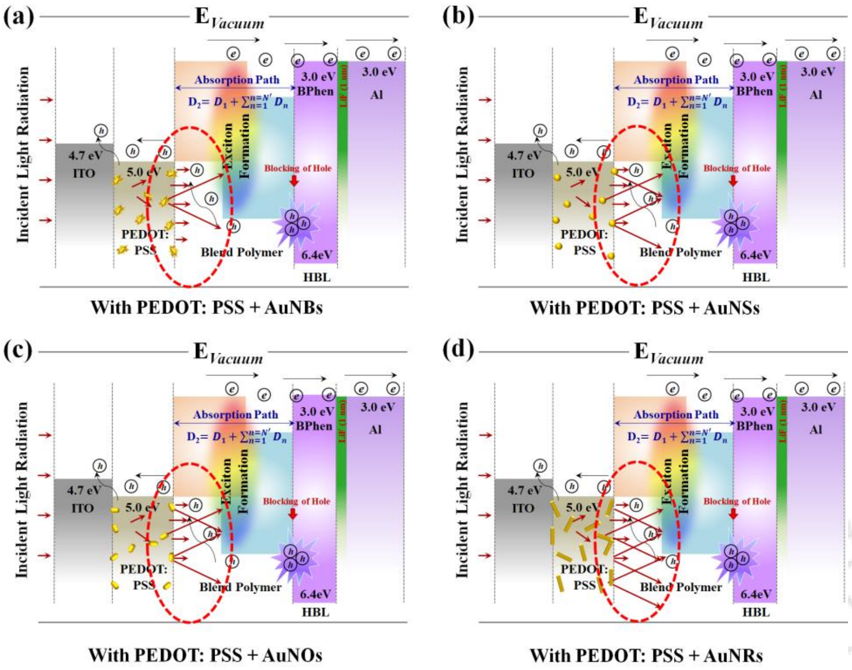

Figure 6.6. Schematic representation of the mechanism involved for rrP3HT:PC$_{71}$BM BHJ solar cell with different shaped AuNPs viz., (a) AuNBs, (b) AuNSs, (c) AuNOs and (d) AuNRs and BPhen/LiF/Al as the double cathode interfacial layer.

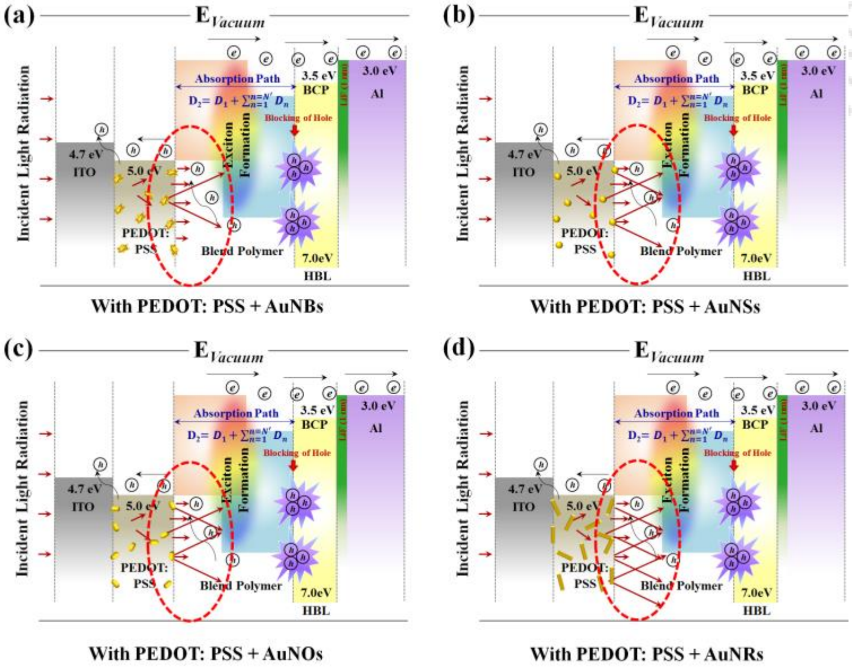

Figure 6.7. Schematic representation of the mechanism involved for rrP3HT:PC$_{71}$BM BHJ solar cell with different shaped AuNPs viz., (a) AuNBs, (b) AuNSs, (c) AuNOs and (d) AuNRs and BCP/LiF/Al as the double cathode interfacial layer.

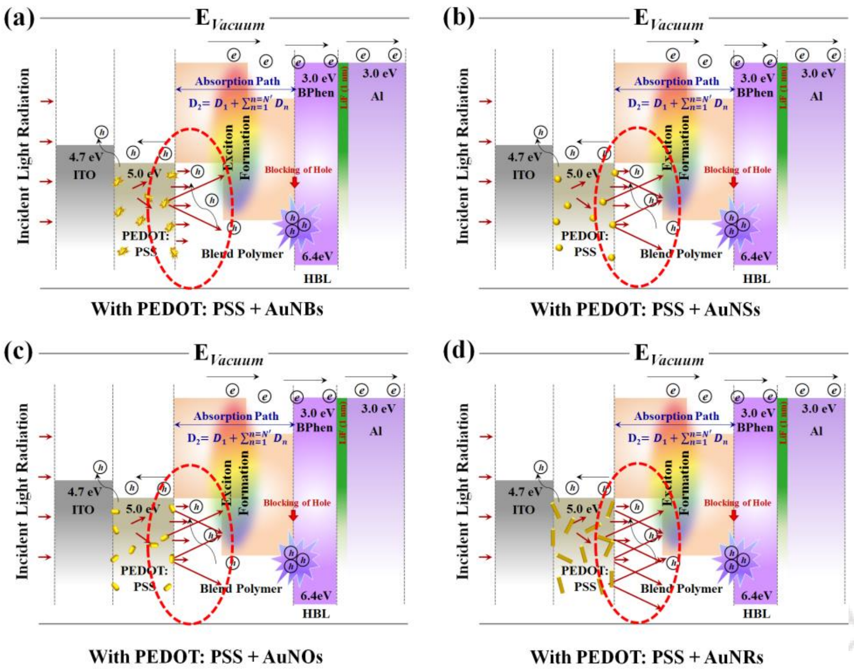

Figure 6.8. Schematic representation of the mechanism involved for rrP3HT:PC$_{61}$BM BHJ solar cell with different shaped AuNPs viz., (a) AuNBs, (b) AuNSs, (c) AuNOs and (d) AuNRs and BPhen/LiF/Al as the double cathode interfacial layer.

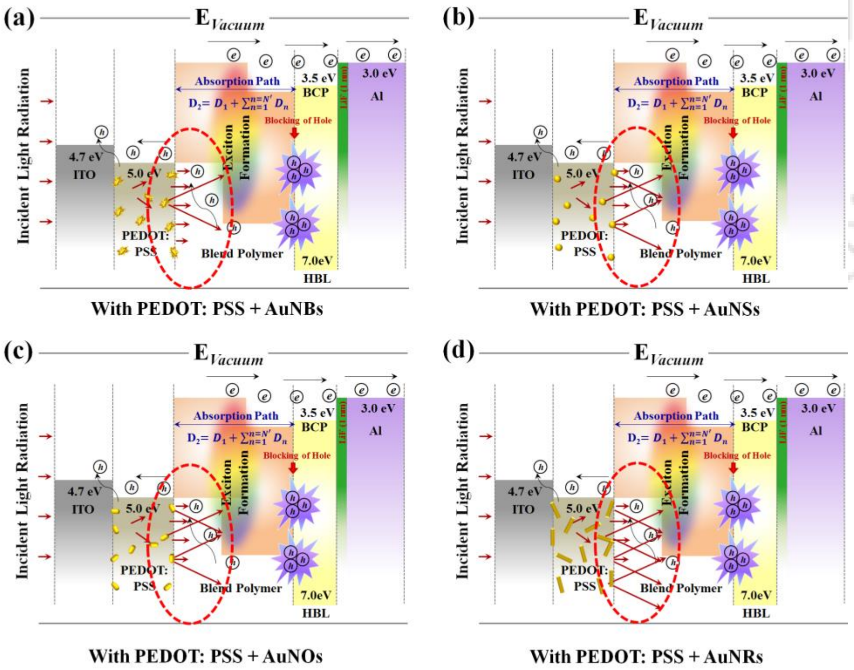

Figure 6.9. Schematic representation of the mechanism involved for rrP3HT:PC$_{61}$BM BHJ solar cell with different shaped AuNPs viz., (a) AuNBs, (b) AuNSs, (c) AuNOs and (d) AuNRs and BCP/LiF/Al as the double cathode interfacial layer.

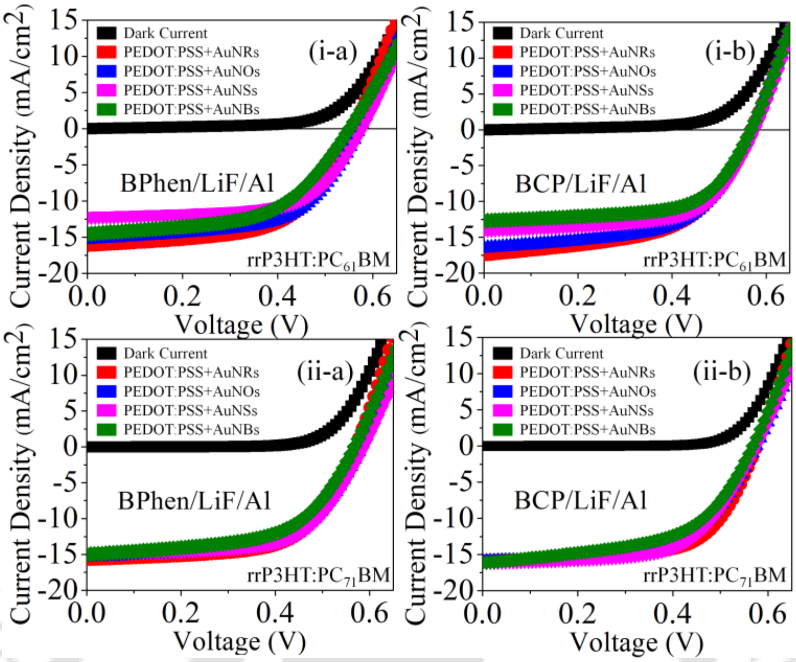

Figure 6.10. J-V characteristics of (i) rrP3HT:PC$_{61}$BM and (ii) rrP3HT:PC$_{71}$BM plasmonic BHJ solar cells containing different shaped AuNPs along with (a) BPhen/LiF/Al and (b) BCP/LiF/Al double cathode interfacial layer.

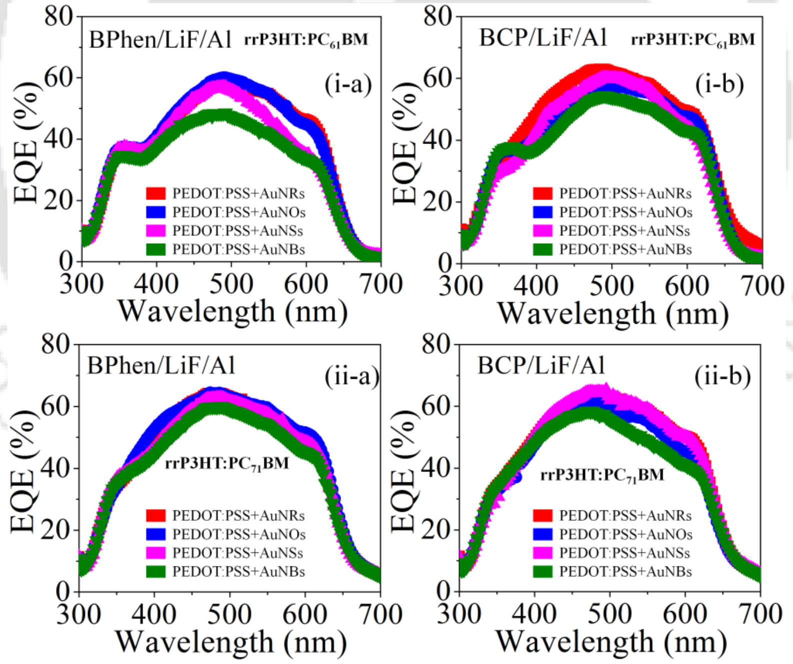

Figure 6.11. EQE spectra of (i) rrP3HT:PC$_{61}$BM and (ii) rrP3HT:PC$_{71}$BM plasmonic BHJ solar cells containing different shaped AuNPs along with (a) BPhen/LiF/Al and (b) BCP/LiF/Al double cathode interfacial layer.

fabricated BHJ cells. It was observed that for both the blend active materials the PCE value increases significantly with the combination of PEDOT:PSS +AuNRs based HIL and BCP/LiF/Al as the double cathode interfacial layer. Figure.6.10 and Figure.6.11 represented the J-V characteristics and EQE spectra of all the fabricated plasmonic BHJ devices. For the device having configuration (8) it has been observed that the maximum ɳ=5.53% with J_{sc}=16.98 mA/cm², V_{oc}=0.57 V and FF= 57.1% for rrP3HT:$PC_{61}BM$ blend polymer, on the other hand, the maximum ɳ for the device having configuration (16) with rrP3HT:$PC_{71}BM$, was obtained to be 5.83% with J_{sc}=15.77 mA/cm², V_{oc}=0.58 V and FF= 63.5%. An analogues behaviour was also noticed when BCP/LiF/Al was replaced with BPhen/LiF/Al. For the device having configuration (4) it has been observed that the maximum ɳ=5.23% with J_{sc}=16.17 mA/cm², V_{oc}=0.57 V and FF= 56.7% for rrP3HT:$PC_{61}BM$ blend polymer, on the other hand, the maximum PCE for the device having configuration (12) with rrP3HT:$PC_{71}BM$, was obtained to be 5.55% with J_{sc}=15.75 mA/cm², V_{oc}=0.57 V and FF= 61.9%. Similar incremental pattern were also observed in the EQE measurements. From EQE study it was noticed that the devices containing BCP as second cathode interfacial layer showed highest quantum efficiency than the other cathode contact in between 300-700 nm wavelength range, with EQE values over ≥ 60% for rrP3HT:$PC_{61}BM$ and ≥ 65% for rrP3HT:$PC_{71}BM$ for all the metal NPs contained HIL. As for all the devices EQE measurements were carried out outside the glove box without encapsulation under high humidity condition (~80%), due to the fast degradation of BCP, BPhen and the blend active layers, very high increment were not observed in the EQE spectra. For analysing the effect of double cathode interfacial layer, it was observed that, compared to BPhen/LiF/Al, BCP/LiF/Al is showing better device performance which is because of the better energy level alignment of BCP/LiF/Al with the active layers compared to BPhen/LiF/Al.[23] Further the selectivity of BCP towards electrons is very high as it has wide band gap (E_g ~3.5 eV) and very deeper HOMO level (~-7 eV) due to which it can block holes and minimize the recombination of charge between the cathode contacts-blend active layers [Figure. 6.6 to Figure. 6.9]. Again for analysing the effect of different plasmonic AuNPs, it was noticed that with PEDOT:PSS + AuNBs, all the devices are showing inferior performance compared to PEDOT:PSS + AuNSs and PEDOT:PSS + AuNOs, whereas with PEDOT:PSS + AuNRs the devices were showing best performances compared to all. This may be due to the higher surface plasmon effect of AuNRs compared to other which enhances the absorption length, scattering and trapping of the of incident photon which is when travel through the modified HIL [Figure. 6.6 to Figure. 6.9]. This statement was also supported by UV-Vis study [Figure. 6.1] from which it is clearly visible that compared to the other AuNPs, AuNRs are covering almost the entire UV-Vis spectrum (400nm-900nm) by its two characteristics surface plasmon resonance peaks. Due to this AuNRs able to enhance the photo absorption by increasing the forward scattering cross section and the near-field enhancement which further help to increase the PCE value of the fabricated BHJ solar cell. The device parameters obtained from all the devices with different configurations, mentioned in Table 6.1, are summarized in Table 6.2. To the best of our knowledge, these result are one of the highest reported value on rrP3HT:PCBM based organic BHJ system and the results can successively explain the influence of shape of AuNPs to magnify the PCE value of rrP3HT:PCBM based BHJ solar cells in presence of double cathode interfacial layer.

Different approaches are mentioned in the literature to improve the performance of BHJ solar cells by a variety of molecular designing and device structure modulations. Modification in cathode contact by inserting functional buffer layer[24-27] and in the hole injecting layer with plasmon induced NPs are one of the efficient approaches among them.[28-32] The coalescing metal NPs in PEDOT:PSS layer is relatively facile and most facile approach. As PEDOT:PSS is soluble in aqueous medium and withal the gold NPs can be synthesized by liquid chemical method, so these NPs can facilely be co-commixed with PEDOT:PSS without further functionalization. Regarding this point, it was observed that incorporation of NaBH4 contained AuNPs in PEDOT:PSS can improve the efficiency of P3HT:PCBM predicated solar cell up to 3.19% with LiF/Al contact.[31]

Table 6.2. Summary of photovoltaic performance of all the fabricated plasmonic BHJ solar cell.

Device Configuration	$J_{sc,max}$ (mA.cm^{-2})	$V_{oc,max}$ (V)	FF_{max} (%)	PCE,η_{max} (%)
(1)	14.51	0.56	53.6	4.36
(2)	12.14	0.58	63.3	4.46
(3)	15.29	0.58	57.7	5.12
(4)	**16.17**	**0.57**	**56.7**	**5.23**
(5)	12.69	0.57	61.2	4.43
(6)	13.92	0.58	61.3	4.94
(7)	16.48	0.58	56.2	5.37
(8)	**16.98**	**0.57**	**57.1**	**5.53**
(9)	14.98	0.57	56.7	4.78
(10)	14.78	0.58	62.0	5.31
(11)	15.35	0.58	59.8	5.32
(12)	**15.75**	**0.57**	**61.9**	**5.55**
(13)	16.15	0.57	54.2	4.97
(14)	16.08	0.58	60.1	5.61
(15)	15.87	0.58	61.7	5.68
(16)	**15.77**	**0.58**	**63.5**	**5.83**

Further, it has been found that the efficiency of BHJ solar cell is vigorously affected by the size of the metal NPs. 50 nm sized AuNPs contained PEDOT:PSS layer can ameliorates the efficiency of the same blend polymer system from 3.57% to 4.24%.[29] Again, the amalgamation of Au-Ag alloy NPs in active layer amended the PCE up to 4.73% with Ca/Al as cathode contact.[28]

In this study, we have successfully amended the PCE value for both the bend active layers through combined influence of different shaped plasmonic gold nanoparticles (AuNPs) and the double cathode interfacial layer. Initially, four different types AuNPs, viz. CTAB capped gold nanorod (AuNRs), gold nanosphere (AuNSs), gold nano-oval (AuNOs) and gold nano branch (AuNBs) were synthesized separately.These four coalesced NPs solution are then commixed together in the PEDOT:PSS hole injecting layer to compose four new NPs doped hole injecting layers for the application of organic BHJ solar cell. The plasmonic metal nanoparticles were incorporated in the PEDOT:PSS layer is to improved photocurrent of the fabricated BHJ solar cell by increasing optical absorption and scattering in both the UV and visible wavelength range inside the devices. For dual cathode interracial layer, two organic small molecules, BPhen and BCP were used along with LiF/Al cathode contact to improve the charge collection. For both the active layers systems the efficiency enhances significantly with PEDOT:PSS + AuNRs as HIL and BCP/LiF/Al as cathode contact. Moreover, this study introduced a profoundly facile and very easy technique for high performance rrP3HT:$PC_{61}BM$ and rrP3HT:$PC_{71}BM$ based organic BHJ solar cell with PCE ~6 %, a value which can be further ameliorated by engineering the contrivance architecture and by utilizing preferential additives.

6.3 Conclusion

In conclusion, combined influence of different shaped plasmonic gold nanoparticles (AuNPs) and the double cathode interfacial layer on rrP3HT:$PC_{61}BM$ and rrP3HT:$PC_{71}BM$ based bulk heterojunction solar cell's performance was systematically discussed. Initially, four different types AuNPs, viz. CTAB capped gold nanorod (AuNRs), gold nanosphere (AuNSs), gold nano-oval (AuNOs) and gold nano branch (AuNBs) were synthesized separately and then blend with PEDOT: PSS hole transport layer to form four newly doped hole injecting layers and their effect on improving the power conversion efficiency (PCE) of rrP3HT:PCBM based BHJ solar cell was systamatically analysed. The importance and effect of NPs modified HIL on the device parameters are systematically validated and were compared with each other. It has been found that the PCE increases considerably for both the active blend systems, in presence of PEDOT:PSS + AuNRs with

BCP/LiF/Al as the modified cathode electrode, because of the better energy level matching of BCP/LiF/Al with the active blend and the excellent surface plasmon property of the AuNRs in the UV-visible region compared to AuNBs, AuNSs and AuNOs. The device with ITO/ PEDOT:PSS + AuNRs/rrP3HT:$PC_{71}BM$/BCP/LiF/Al configuration showed the highest PCE, η= 5.83 % with J_{sc}= 15.80 mA/cm^2, V_{oc}= 0.58 V and FF=63%, whereas, for ITO/ PEDOT:PSS + AuNRs/rrP3HT:$PC_{61}BM$/BCP/LiF/Al, the device parameters were observed as PCE, η= 5.44 % with J_{sc}=17.40 mA/cm^2, V_{oc}= 0.57 V and FF= 57%. These results conclusively explain a very easy method in which the combined influence of different shaped plasmonic gold nanoparticles (AuNPs) and the double cathode interfacial layer outstandingly enrich the PCE and on the whole performance of P3HT-PCBM based BHJ solar cells.

6.4 References

1. Choi, H.; Lee, J.-P.; Ko, S.-J.; Jung, J.-W.; Park, H.; Yoo, S.; Park, O.; Jeong, J.-R.; Park, S.; Kim, J. Y. Multipositional Silica-Coated Silver Nanoparticles for High-Performance Polymer Solar Cells. *Nano Lett.* **2013**, *13*, 2204–2208.

2. Li, X.; Choy, W. C. H.; Huo, L.; Xie, F.; Sha, W. E. I.; Ding, B.; Guo, X.; Li, Y.; Hou, J.; You, J.; Yang, Y. Dual Plasmonic Nanostructures for High Performance Inverted Organic Solar Cells. *Adv. Mater.* **2012**, *24*, 3046–3052.

3. Lu, L.; Luo, Z.; Xu, T.; Yu, L. Cooperative Plasmonic Effect of Ag and Au Nanoparticles on Enhancing Performance of Polymer Solar Cells. *Nano Lett.* **2013**, *13*, 59–64.

4. Linic, S.; Christopher, P.; Ingram, D. B. Plasmonic-Metal Nanostructures for Efficient Conversion of Solar to Chemical Energy. *Nat. Mater.* **2011**, *10*, 911–921.

5. Banerjee, S.; Pillai, S. C.; Falaras, P.; O'Shea, K. E.; Byrne, J. A.; Dionysiou, D. D. New Insights into the Mechanism of Visible Light Photocatalysis. *J. Phys. Chem. Lett.* 2014, **5**, 2543–2554.

6. Yuan, K.; Chen, L.; Chen, Y. Optical Engineering of Uniformly Decorated Graphene Oxide Nanoflakes via in Situ Growth of Silver Nanoparticles with Enhanced Plasmonic Resonance. *ACS Appl. Mater. Interfaces.* **2014**, *6*, 21069–21077.

7. Jung, K.; Song, H. -J.; Lee, G.; Ko, Y.; Ahn, K.; Choi, H.; Kim, J. Y.; Ha, K.; Song, J.; Lee, J.-K.; Lee, C.; Choi, M. Plasmonic Organic Solar Cells Employing Nanobump Assembly via Aerosol-Derived Nanoparticles. *ACS Nano* **2014**, *8*, 2590–2601.

8. Li, X. H.; Choy, W. C. H.; Lu, H. F.; Sha, W. E. I.; Ho, A. H. P. Efficiency Enhancement of Organic Solar Cells by using Shape-Dependent Broadband Plasmonic Absorption in Metallic Nanoparticles. *Adv. Funct. Mater.* **2013**, *23*, 2728–2735.

9. Madogni, V. I.; Kounouhéwa, B.; Akpo, A.; Agbomahéna, M.; Hounkpatin, S. A.; Awanou, C. N. Comparison of Degradation Mechanisms in Organic Photovoltaic Devices upon Exposure to a Temperate and a Subequatorial Climate. *Chem. Phys. Lett.* **2015**, *640*, 201–214.

10. Brabec, C. J.; Shaheen, S. E.; Winder, C.; Sariciftci, N. S. Effect of LiF/Metal Electrodes on the Performance of Plastic Solar Cells. *Appl. Phys. Lett.* **2002**, *80*, 1288–1290.

11. Mityashin, A.; Cheyns, D.; Rand, B. P.; Heremans, P. Understanding Metal Doping for Organic Electron Transport Layers. *Appl. Phys. Lett.* **2012**, *100*, 053305.

12. Kang, R.; Oh, S.-H.; Kim, D.-Y. Influence of the Ionic Functionalities of Polyfluorene Derivatives as a Cathode Interfacial Layer on Inverted Polymer Solar Cells. *ACS Appl. Mater. Interfaces* **2014**, *6*, 6227–6236.

13. Li, Y.; Zhao, Y.; Chen, Q.; Yang, Y.; Liu, Y.; Hong, Z.; Liu, Z.; Hsieh, Y.-T.; Meng, L.; Li, Y.; Yang, Y. Multifunctional Fullerene Derivative for Interface Engineering in Perovskite Solar Cells. *J. Am. Chem. Soc.* **2015**, *137*, 15540–15547.

14. Mateker, W. R.; McGehee, M. D. Progress in Understanding Degradation Mechanisms and Improving Stability in Organic Photovoltaics. *Adv. Mater.* **2017**, *29*, 1603940.

15. Graetzel, M.; Janssen, R. A. J.; Mitzi, D. B.; Sargent, E. H. Materials Interface Engineering for Solution-Processed Photovoltaics. *Nature* **2012**, *488*, 304–312.

16. Kim, I.; Haverinen, H. M.; Li, J.; Jabbour, G. E. Enhancement of Device Performance of Organic Solar Cells by an Interfacial Perylene Derivative Layer. *ACS Appl. Mater. Interfaces* **2010**, *2*, 1390–1394.

17. Guo, S.; Ruderer, M. A.; Rawolle, M.; Körstgens, V.; Birkenstock, C.; Perlich, J.; Müller-Buschbaum, P. Evolution of Lateral Structures during the Functional Stack Build-up of P3HT:PCBM-Based Bulk Heterojunction Solar Cells. *ACS Appl. Mater. Interfaces* **2013**, ***5***, 8581–8590.

18. Müller-Buschbaum, P. The Active Layer Morphology of Organic Solar Cells Probed with Grazing Incidence Scattering Techniques. *Adv. Mater.* **2014**, *16*, 7692–7709.

19. Oesinghaus, L.; Schlipf, J.; Giesbrecht, N.; Song, L.; Hu, Y.; Bein, T.; Docampo, P.; Müller-Buschbaum, P. Toward Tailored Film Morphologies: The Origin of Crystal Orientation in Hybrid Perovskite Thin Films. *Adv. Mater. Interfaces* **2016**, *3*, 1600403.

20. Reinspach, J. A.; Diao, Y.; Giri, G.; Sachse, T.; England, K.; Zhou, Y.; Tassone, C.; Worfolk, B. J.; Presselt, M.; Toney, M. F.; Mannsfeld, S.; Bao, Z. Tuning the Morphology of Solution-Sheared P3HT:PCBM Films. *ACS Appl. Mater. Interfaces* **2016**, *8*, 1742–1751.

21. Shao, M.; Keum, J.; Chen, J.; He, Y.; Chen, W.; Browning, J. F.; Jakowski, J.; Sumpter, B. G.; Ivanov, I. N.; Ma, Y.-Z.; Rouleau, C. M.; Smith, S. C.; Geohegan, D. B.; Hong, K.; Xiao, K. The Isotopic Effects of Deuteration on Optoelectronic Properties of Conducting Polymers. *Nat. Commun.* **2014**, *5*, 4180.

22. Singh, A.; Dey, A.; Das, D.; Iyer, P. K. Combined Influence of Plasmonic Metal Nanoparticles and Dual Cathode Buffer Layers for Highly Efficient rrP3HT:PCBM-Based Bulk Heterojunction Solar Cells. *J. Mater. Chem. C* **2017**, *5*, 6578–6587.

23. Singh, A.; Dey, A.; Das, D.; Iyer, P. K. Effect of Dual Cathode Buffer Layer on the Charge Carrier Dynamics of rrP3HT:PCBM Based Bulk Heterojunction Solar Cell. *ACS Appl. Mater. Interfaces* **2016**, *8*, 10904–10910.

24. Jung, G. H.; Lee, J.-L. Origin of Gap States in the Electron Transport Layer of Organic Solar Cells. *J. Mater. Chem. A* **2013**, ***1***, 3034–3039.

25. Xiao, T.; Fungura, F.; Cai, M.; Anderegg, J. W.; Shinar, J.; Shinar, R. Improved Efficiency and Stability of Inverted Polymer Solar Cells with a Solution-Processed BPhen Interlayer and Polystyrene Beads. *Org. Electron.* **2013**, *14*, 2555–2563.

26. Chang, C.-C.; Lin, C.-F.; Chiou, J.-M.; Ho, T.-H.; Tai, Y.; Lee, J.-H.; Chen, Y.-F.; Wang, J.-K.; Chen, L.-C.; Chen, K.-H. Effects of Cathode Buffer Layers on the Efficiency of Bulk-Heterojunction Solar Cells. *Appl. Phys. Lett.* **2010**, *96,* 263506.

27. Oh, I. S.; Ji, C. H.; Oh, S. Y. Effects of Ytterbium on Electrical and Optical Properties of BCP/Ag/WO_3 Transparent Electrode Based Organic Photovoltaic Cells *Electron. Mater. Lett.* **2016**, *12*, 156–162.

28. Chen, H.-C.; Chou, S.-W.; Tseng, W.-H.; Chen, I. W. P.; Liu, C.-C.; Liu, C.; Liu, C.-L.; Chen, C.-H.; Wu, C.-I.; Chou, P.-T. Large AuAg Alloy Nanoparticles Synthesized in Organic Media Using a One-Pot Reaction: Their Applications for High-Performance Bulk Heterojunction Solar Cells. *Adv. Funct. Mater.* **2012**, *22*, 3975–3984.

29. Wu, J. L.; Chen, F. C.; Hsiao, Y. S.; Chien, F. C.; Chen, P. L.; Kuo, C. H.; Huang, M. H.; Hsu, C. S. Surface Plasmonic Effects of Metallic Nanoparticles on the Performance of Polymer Bulk Heterojunction Solar Cells. *ACS Nano* 2011**, 5**, 959–967.

30. Spyropoulos, G. D.; Stylianakis, M. M.; Stratakis, E.; Kymakis, E. Organic Bulk Heterojunction Photovoltaic Devices with Surfactant-Free Au Nanoparticles Embedded in the Active Layer. *Appl. Phys. Lett.* **2012**, *100*, 213904.

31. Woo, S.; Jeong, J. H.; Lyu, H. K.; Han, Y. S.; Kim, Y. In Situ-Prepared Composite Materials of PEDOT:PSS Buffer Layer-Metal Nanoparticles and their Application to Organic Solar Cells. *Nanoscale Res. Lett.* **2012**, *7*, 641.

32. Khoo, S. Y.; Yang, H. B.; He, Z. M.; Miao, J. W.; Leong, K. C.; Li, C. M.; Tan, T. T. Y. Enhanced Charge Extraction of Polymer Solar Cell by Solution-Processable Gold Nanoparticles. *J. Mater. Chem. C* **2013**, *1*, 5402–5409.

Chapter 7

EPILOGUE

Due to the influence of clean and sustainable energy device development and therefore the motivation to fabricate highly efficient organic bulk heterojunction solar cell, which can possibly be used as an efficient solar energy converter in this tremendous universal demand of easily processable energy transforming device, this thesis mainly focused to introduce different methods to enhance the power conversion efficiency of very commonly studied system, namely, rrP3HT with PC$_{61}$BM and/or rrPC$_{71}$BM based organic bulk heterojunction solar cell. The entire thesis essentially pays attention in device engineering of BHJ solar cell by modulating the cathode and anode interfacial layers to achieve improved photovoltaics performance.

At the very beginning, the thesis discussed about the individual influence of the molar mass ratio of donor-acceptor polymers, the effect of annealing temperature and the significance of cathode buffer layer on amending the power conversion efficiency of BHJ solar cell. For this study rrP3HT:PC$_{71}$BM was choosen as the active layer blend whereas Ca, LiF, BPhen and BCP were selected for the cathode buffer layer. The molar mass ratio was varied systematically as 1:0.6, 1:0.8, 1:1.0 and 1:1.2 respectively whereas to study the effect of temperature the substrates were annealed sequencially at 100°C, 125°C, 150°C and 175°C respectively. The performance of all the fabricated BHJ solar cells were correlated systematically with their thin film growth structure and energy level diagram. This study successfully standardized all this essential physical parameters which eventually controled the performance of thin film solar cell. By controlling these factors, the efficiency of the fabricated rrP3HT:PC$_{71}$BM based BHJ was increased from 2.69% (with 1:0.6, RT, LiF/Al) to 4.79% (with 1:0.8,150°C, BCP/Al). This drastic enhancement in PCE of the devices having BCP/Al as the cathode contact compared to the other device configurations is due to the collective effects of BCP along with Al due to the better hole-blocking capacity and better phase separation of the active blend layer at 150°C annealing temperature.

In the next step, another new concept was demonstrated in the dissertation by incorporation of dual cathode buffer layer in rrP3HT:PCBM based BHJ solar cell for harvesting the PCE value. In this study, three different additional buffer layers viz., Alq$_3$, BPhen, and BCP was incorporated along with LiF/Al as conventional cathode contact for the fabrication of both rrP3HT:PC$_{61}$BM and rrP3HT:PC$_{71}$BM based BHJ solar cells. The photovoltaic performances were again correlated with their energy level diagram. It has been observed that the devices with BCP/LiF/Al as dual cathode buffer layer showed the best device performance for both with rrP3HT:PC$_{71}$BM and rrP3HT:PC$_{61}$BM system which is due to the combined effects of better hole-blocking capacity of BCP and low work function provided by LiF/Al with the blend polymer. The PCE of rrP3HT:PC$_{61}$BM was found to be improvising drastically from 2.4% (LiF/Al) to 4.5% (BCP/LiF/Al) and for rrP3HT:PC$_{71}$BM from 4.04% (LiF/Al) to 4.96% (BCP/LiF/Al) with very easy modification of the cathode contact.

Furthermore, in order to modulate the anode buffer layer, plasmonic metal nanoparticles were introduced into the BHJ device structure. For this purpose, two different types of metal NPs, viz. citrate capped gold (Au) and silver (Ag) NPs were blended (20 v/v %) separately in the hole transport layer PEDOT:PSS. For the dual cathode buffer layer, again the same hole blocking layers, viz., BPhen and BCP, along with LiF/Al cathode contact were selected. The combined influence of both the NPs as well as the dual cathode buffer layers were investigated for both the blend polymers, rrP3HT:PC$_{61}$BM and rrP3HT:PC$_{71}$BM. It was observed that for both the blend polymer systems the power conversion efficiency (PCE) increases significantly in the presence of PEDOT:PSS + AuNPs and PEDOT:PSS + AgNPs with BCP/LiF/Al as the cathode contact compared to the bare PEDOT:PSS layer. Especially, the devices containing PEDOT:PSS + AuNPs and BCP/LiF/Al, the highest PCE were observed for both the blend polymers because of the better energy band alignment of BCP/LiF/Al with the active layers and the superior surface plasmon resonance of the AuNPs at the visible spectrum compared to AgNPs. In this study the PCE again increased for rrP3HT:PC$_{61}$BM from ~4.68 % (BCP/LiF/Al, bare PEDOT:PSS) to ~4.99 % (BCP/LiF/Al, PEDOT:PSS+AuNPs) whereas for rrP3HT:PC$_{71}$BM system it increased from 4.96 % (BCP/LiF/Al, bare PEDOT:PSS) to 5.65 % (BCP/LiF/Al, PEDOT:PSS+AuNPs). These results conclusively explain the importance of cathode and anode buffer layers modulation to remarkably improve the PCE and overall device performance of rrP3HT:PCBM based BHJ solar cells.

Again in order to find the influence of metal NPs concentration for harvesting the PCE of organic BHJ the collective effect of plasmon induced dual metal nanoparticles (NPs) and the dual cathode buffer layers were studied. For this analysis, initially, two different types of metal NPs, viz. citrate capped gold (Au) and silver (Ag) NPs were separately blended with three different volume ratio [AuNPs + AgNPs (25:75), AuNPs + AgNPs (50:50) and AuNPs + AgNPs (75:25)]. These three blended NPs solution were then mixed together in the PEDOT:PSS to form three new NPs doped hole injecting layers and their effect on the performance of rrP3HT:PCBM based BHJ solar cell was also systamatically analysed. The plasmonic metal nanoparticles were incorporated in the PEDOT:PSS layer to improve photo current of the fabricated BHJ solar cell by increasing optical absroption and scattering inside the devices. It was observed that for both the blend polymer systems the PCE increases significantly in presence of PEDOT:PSS + AuNPs:AgNPs (25:75) with BCP/LiF/Al as the cathode contact compared to others the superior surface plasmon resonance of the AuNPs:AgNPs (25:75) at the UV-visible spectrum compared to AuNPs:AgNPs (50:50) and AuNPs:AgNPs (75:25). In this case the PCE further increases for rrP3HT:PC$_{61}$BM from 4.03 % [LiF/Al, PEDOT:PSS + AuNPs:AgNPs (25:75)] to 5.31 % [BCP/LiF/Al, PEDOT:PSS+ AuNPs:AgNPs (25:75)] whereas for rrP3HT:PC$_{71}$BM system it is increases from 4.89% [LiF/Al, PEDOT:PSS+ AuNPs:AgNPs (25:75)] to 5.71 % [BCP/LiF/Al, PEDOT:PSS+ AuNPs:AgNPs (25:75)]. These results precisely explain the importance of volume ratio of plasmonic metal NPs along with dual cathode buffer layer for increasing the overall device performance of rrP3HT:PCBM based BHJ solar cells.

Finally, as the plasmonicity of metal NPs strongly varied with its different shape and size, and in order to understand this effect in organic BHJ solar cell performances, four different shaped AuNPs, viz. CTAB capped gold nanorod (AuNRs), nanosphere (AuNSs), nano-oval (AuNOs) and nano branch (AuNBs) were synthesized. These particles were then separately mixed together in the PEDOT:PSS hole transport layer to form four new NPs doped hole injecting layers and their effects were studied with the dual cathode buffer layers on improving the PCE of rrP3HT:PCBM based BHJ solar cells. The synthesized nanoparticles were characterised by various caracterization techniques viz., UV-Vis absorption study and TEM analysis. The intention of varying the shape of the NPs was to improve the photo current by light scattering phenomenon inside the BHJ solar cell. It was observed that for both the blend polymer systems the PCE increased significantly in the presence of PEDOT:PSS + AuNRs with BCP/LiF/Al as the cathode contact compared to others because of the superior surface plasmon resonance of the AuNRs at the entire UV-visible spectrum compared to AuNSs, AuNOs and AuNBs. In these cases the observed increment in PCE value for rrP3HT:$PC_{61}BM$ system were found to be 5.53% whereas for rrP3HT:$PC_{71}BM$ the same was observed as 5.83%.

Thus, by step wise device standardization this thesis successfully explained some facile methods by which the power conversion efficiency of very commonly studied system, namely rrP3HT:$PC_{71}BM$ was improved from 4.79% to 5.83%. This concept can be further used moderately in future for highly efficient rrP3HT:$PC_{71}BM$ based flexible tandem or perovskite solar cell fabrication. A schematic representation of the overall thesis overview is shown in Figure. 7.1 below-

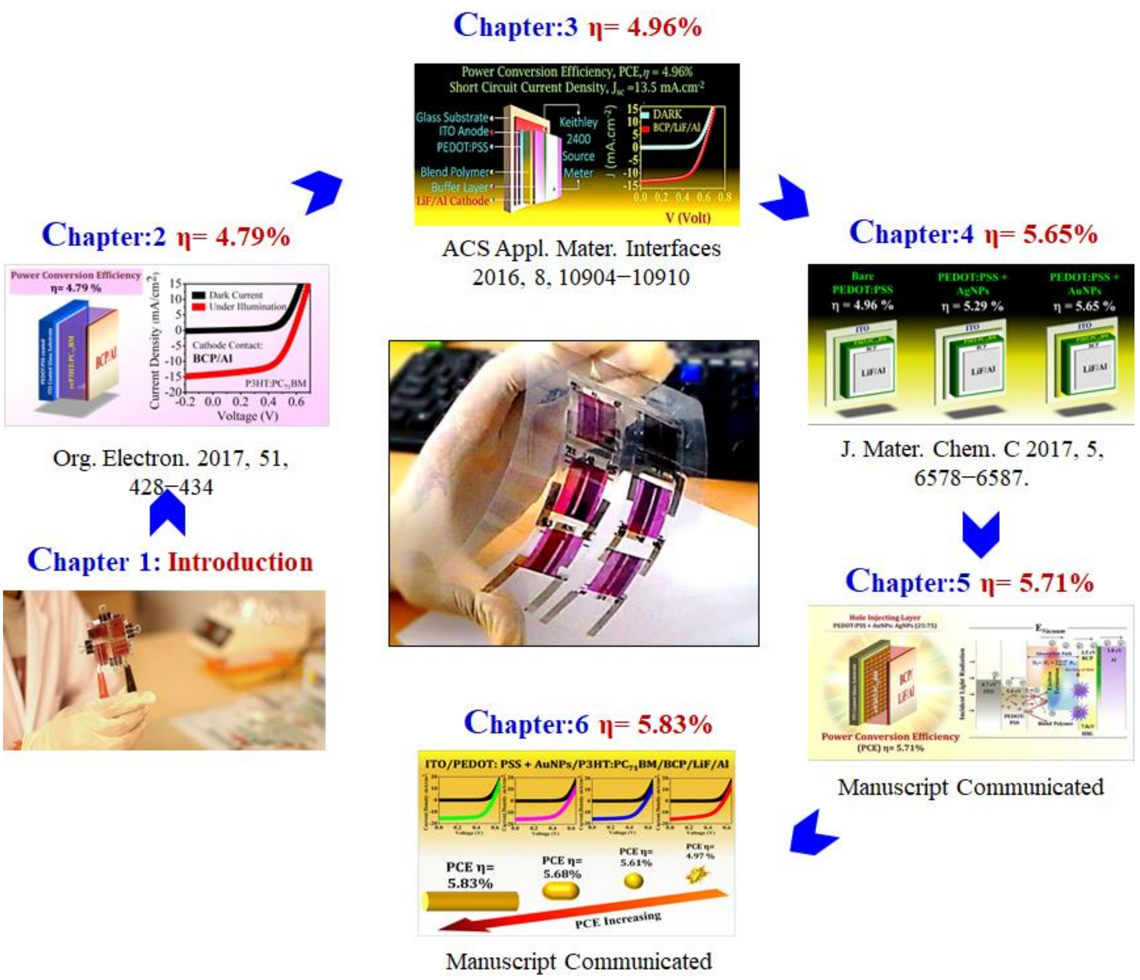

Figure 7.1. Schematic of the Thesis overview.

Publications

Journals:

[1] **Singh, A.;** Dey, A.; Iyer, P. K. Collective Effect of Hybrid Metal Nanoparticles and Dual Cathode Interfacial Layers for High Performance Polymer Solar Cell. **Communicated**.

[2] **Singh, A.;** Dey, A.; Iyer, P. K. Effect of Different Shaped Plasmonic AuNPs and Double Cathode Interfacial Layer on rrP3HT:PCBM Based Bulk Heterojunction Solar Cell. **Communicated**.

[3] **Singh, A.;** Dey, A.; Iyer, P. K. Influence of Molar Mass Ratio, Annealing Temperature and Cathode Buffer Layer on Power Conversion Efficiency of P3HT:$PC_{71}BM$ Based Organic Bulk Heterojunction Solar Cell. *Org. Electron.* **2017,** *51,* 428-434.

[4] **Singh, A.;** Dey, A.; Das, D.; Iyer, P. K. Combined Influence of Plasmonic Metal Nanoparticle and Dual Cathode Buffer Layer for Highly Efficient rrP3HT: PCBM Based Bulk Heterojunction Solar Cell. *J. Mater. Chem. C* **2017,** *5,* 6578-6587.

[5] **Singh, A.;** Dey, A.; Das, D.; Iyer, P. K. Effect of Dual Cathode Buffer Layer on the Charge Carrier Dynamics of rrP3HT: PCBM Based Bulk Heterojunction Solar Cell. *ACS Appl. Mater. Interfaces* **2016,** *8,* 10904-10910.

Patents:

[1] Dey, A.; **Singh, A.;** Iyer, P. K. Method for the Fabrication of Solution Process, Ultra-low Operating Voltage, Stable Organic Field Effect Transistor, 2017, Ref. No. 201731046915, App. No. TEMP/E-1/47841/2017-KOL.

[2] Dey, A.; **Singh, A.;** Iyer, P. K. Method for the Fabrication of Low Cost, Reduced Bias Stress Multi-layers Dielectric System Ultralow Operated n-type Organic Field Effect Transistors, 2017, Ref. No. 201731046914, App. No. TEMP/E-1/47853/2017-KOL.

[3] Dey, A.; **Singh, A.;** Dutta, D.; Ghosh, S. S.; Iyer, P. K. Method for the Detection of Gram Positive and Gram Negative Bacteria by Ultra-low Operating Voltage n-type Organic Field Effect Transistor, 2017, Ref. No. 201831000478, App. No. TEMP/E-1/462/2018-KOL.

Publications

Book Chapter:

[1] Dey, A.; **Singh, A.;** Das, D.; Iyer, P. K. Organic Semiconductors: A New Future of Nano Devices and Applications in Thin Film Structure in Energy Applications. Springer, **2015**, 97-128.

Journals (not included in the Thesis):

[1] Sharma, B.; **Singh, A.;** Afroz, M. A.; Jacob, J.; Iyer, P. K. Direct Arylation Polymerization Approach for the Synthesis of Narrow Band Gap Cyclopentadithiophene Based Conjugated Polymer and its Application in Solar Cell Devices. *Synth. Met.* **2017,** *226,* 56-61.

[2] Ratha, R.; **Singh, A.;** Bhim Raju, T.; Iyer, P. K. Insight into the Synthesis and Fabrication of 5, 6-alt-Benzothiadiazole based D-π-A Conjugated Copolymers for Bulk-Heterojunction Solar Cell. *Polym. Bull.* DOI: 10.1007/s00289-017-2193-x, 2017.

[3] Dey, A.; **Singh, A.;** Das, D.; Iyer, P. K. Photosensitive Organic Field Effect Transistor: Influence of ZnPc Morphology and Bilayer Dielectrics to Achieve Low Operating Voltage and Low Bias Stress Effect. *Phys. Chem. Chem. Phys.* **2016,** *18,* 32602-32609.

[4] Dey, A.; **Singh, A.;** Das, D.; Iyer, P. K. High-Performance ZnPc Thin Film-Based Photosensitive Organic Field-Effect Transistors: Influence of Multilayer Dielectric Systems and Thin Film Growth Structure. *ACS Omega* **2017,** *2,* 1241-1248.

[5] Das, D.; Gopikrishna, P.; **Singh, A.;** Dey, A.; Iyer, P. K. Efficient Blue and White Polymer Light Emitting Diodes Based on a Well Charge Balanced, Core Modified Polyfluorene Derivative. *Phys. Chem. Chem. Phys.* **2016,** *18,* 7389-7394.

[6] Das, D.; Gopikrishna, P.; **Singh, A.;** Dey, A.; Iyer, P. K. Solution Processed WPLEDs with Good Color Stability and High Color Rendering Index via a Phosphor-Sensitized System. *Chemistry Select* **2017,** *2,* 3184-3190.

[7] Das, D.; Gopikrishna, P.; Narasimhan, R.; **Singh, A.;** Dey, A.; Iyer, P. K. White Polymer Light Emitting Diodes Based on PVK: The Effect of the Electron Injection Barrier on Transport Properties, Electroluminescence and Controlling the Electroplex Formation. *Phys. Chem. Chem. Phys.* **2016,** *18,* 33077-33084.

[8] Soni, S. S.; Fadadu, K. B.; Vaghasiya, J. V.; Solanki, B. G.; Sonigara, K. K.; **Singh, A.;**

Das, D.; Iyer, P. K Improved Molecular Architecture Of D-π-A Carbazole Dyes: 9% PCE with a Cobalt Redox Shuttle in Dye Sensitized Solar Cells. *J. Mater. Chem. A* **2015,** *3,* 21664-21671.

Proceedings (not included in the Thesis):

[1] **Singh, A.;** Raju, T. B.; Dey, A.; Gupta, R. K.; Iyer, P. K. Effect of Dual Cathode Buffer Layer on P3HT: BH-1:PC71BM Based Ternary Organic Solar Cell, *IEEE Conference Proceeding,* **Under Revision**.

[2] **Singh, A.;** Dey, A.; Das, D.; Iyer, P. K. Effect of Substrate Temperature on Twin Donor Layer Organic Solar Cell. *Material Today Proceeding,* **Under Revision.**

[3] **Singh, A.;** Dey, A.; Das, D.; Iyer, P. K. Improvement of Charge Carrier Dynamics in P3HT:PC_{61}BM Based Solar Cell in Presence of Organic Cathode Interfacial Layers, *IEEE Conference Proceeding,* DOI: 10.1109/ICEmElec.2016.8074606.

[4] Dey, A.; **Singh, A.;** Iyer, P. K. Ultra-Low Operating Voltage, Poly (3-hexylthiophene-2,5-diyl) based Highly Light-sensitive Organic Field Effect Transistor, *IEEE Conference Proceeding,* DOI: 10.1109/ICEmElec.2016.8074605.

[5] Dey, A.; **Singh, A.;** Kalita, A.; Das, D.; Iyer, P. K. High Performance, Low Operating Voltage n-Type Organic Field Effect Transistor Based on Inorganic-Organic Bilayer Dielectric System. *Journal of Physics: Conference Series,* **2016,** *704,* 012017 (1-8).

[6] Das, D.; Gopikrishna, P.; **Singh, A.;** Dey, A.; Iyer, P. K. Influence of Emissive Layer Thickness on Electrical Characteristics of Polyfluorene Copolymer Based Polymer Light Emitting Diodes, *Journal of Physics: Conference Series,* **2016,** *704,* 012016 (1-6).

Vitae

Ashish Singh was born in Chhatarpur, Madhya Pradesh, India. He obtained his Bachelor of Engineering in Electronics and Communication and completed Master of Technology in Nanotechnology from Rajiv Gandhi Proudyogiki Vishwavidyalaya, Bhopal, Madhya Pradesh, India. Under the supervision of Prof. Parameswar Krishnan Iyer, he started his research career at the Centre for Nanotechnology, IIT Guwahati – with the development of highly efficient plasmonic nanoparticle induced organic bulk heterojunction solar cell. His current research interests are mainly to focus on the physics of charge photo generation, separation and collection in plasmonically enhanced organic heterojunction and perovskite solar cells. He is also having interest on other functional organic electronic devices like organic thin film based transistors, light emitting diodes, memory and sensor devices.